Stress Distributions around Hydrofoils using Computational Fluid Dynamics

by

Ofer Aharon

B.Sc., Mechanical Engineering,
Tel Aviv University, 1997

SUBMITTED TO THE DEPARTMENT OF MECHANICAL ENGINEERING IN PARTIAL FULFILLMENT OF THE REQUIREMENTS FOR THE DEGREE OF

MASTER OF SCIENCE IN NAVAL ARCHITECTURE AND MARINE ENGINEERING AT THE

MASSACHUSETTS INSTITUE OF TECHNOLOGY

FEBRUARY 2009

Signature of Author……………………………………………………………………………………
Department of Mechanical Engineering
December 15, 2008

Certified by……………………………………………………………………………………………
Klaus-Jürgen Bathe
Professor of Mechanical Engineering
Thesis Advisor

Accepted by……………………………………………………………………….…………………...
David E. Hardt
Professor of Mechanical Engineering
Chairman, Committee for Graduate Students

Stress Distributions around Hydrofoils using Computational Fluid Dynamics

by

Ofer Aharon

Submitted to the Department of Mechanical Engineering
on December 15th, 2008 in Partial Fulfillment of the
Requirements for the Degree of Master of Science in
Naval Architecture and Marine Engineering

Abstract

This research describes the reciprocal influence between two foils, vertically and horizontally oriented, on each other for different gaps between them. Those cases are the focus part of a bigger process of lowering significantly the drag of a ship when hydrofoils are attached to its hull. The research results are based on CFD analyses using the ADINA software. In order to verify the CFD process, a comparison was made between analytical, experimental and ADINA's results for a single foil. The chosen foil was the famous Clark-Y foil; however a correction to its geometry was made using the Unigraphics software. Using the corrected geometry with an analytical solution well detailed and explained, the results of the CFD model were compared to experimental and analytical solutions. The matching of the results and the obtained accuracy are very high and satisfactory.

In addition, the research contains an examination of the results when one of the boundary conditions is changed. Surprisingly, it was discovered that the FREE slip condition along the foil is much closer to reality than the NO slip condition. Another examination was stretching horizontally the foil and checking the pressure distribution behavior. Those results met exactly the expectations. As for the main core of this research, both the bi-plane case and the stagger case were found to be less effective than using a single foil. The conclusion of those investigations is that using those cases a few decades ago was for a structural reason rather than stability or speed.

Since this research is very wide but also deep in its knowledge, references and academic work, many future research works may be based on it or go on from its detailed stages.

Thesis Advisor: Klaus-Jürgen Bathe.
Title: Professor of Mechanical Engineering.

Biographical Note

Ofer Aharon, Master Student
Mechanical Engineering Department
Massachusetts Institute of Technology
77 Massachusetts Avenue, Office 3-359

Education

Massachusetts Institute of Technology, Cambridge, USA
Master of Science Degree in Naval Architecture & Marine Engineering, February 2009
Relevant Courses: Finite Element Analysis of Solids and Fluids, Marine Hydrodynamics, Principles of Naval Architecture, Principles of Naval Ship Design, Ship Power and Propulsion, Ship Structural Analysis and Design, Plates and Shells.

Tel-Aviv University, Tel-Aviv, Israel
Bachelor of Science Degree in Mechanical Engineering, June 1997
Relevant Courses: Fluid Mechanics (1) + (2), Physics (1) + (2), Mechanics of Solid (1) + (2), Theory of Machines, Structural Mechanics, Introduction to Finite Elements, Thermodynamics (1) + (2), Heat Transfer, Mathematical Analysis, Numerical Analysis, Advanced Programming.

Experience

Israeli Navy, Navy Seals, Head of the Engineering Section
September 2003 - August 2007
I have developed structures and mechanisms according to the needs of the fighters. Some of the sophisticated systems and the dynamic cases were analyzed and optimized by using the Finite Element Method (ANSYS).

Israeli Navy, Officer in the Naval Architecture Branch in the Battle Ships Section
February 2001 - September 2003
I have analyzed the stability and strength of the gunships and designed structures according to the needs of the navy. Most of the analyses were performed by using ANSYS and General Hydrostatics (GHS) softwares and mathematical models in Mathcad.

Israeli Navy, Officer in the Naval Architecture Branch in the Planning Crafts Section
September 1997 - February 2001
I have analyzed the stability of the patrol crafts and their performance at sea. Most of the patrol crafts are planning vehicles which require special computations methods.

Skills

Languages:	Fluent Hebrew and English.
Computer:	ADINA, ANSYS, GHS, C++, Mathcad, Unigraphics, Microsoft Office.

Acknowledgements

This Thesis was performed and written during 2008 in the Finite Elements Lab of the Mechanical Engineering Department at MIT. At first, I would like to thank G-d who guides me through my events in life and lights my way until the very sweet end of each one of them.

I would like to express my deep gratitude to my thesis advisor, Prof. Klaus-Jürgen Bathe, for his guidance and constructive criticism throughout this year. His excellent advice inspired me towards completion of this research. His life experience in general and his knowledge of finite element methods in particular, made me very proud to have worked with him.

I would like to thank ADINA R & D, Inc. for allowing me to use their finite element software ADINA for my research. All the finite element analyses and results presented in this paper were generated by this code. Special Thanks to Dr. Shanhong Ji and Lay Tan for their kind help and smart suggestions.

I am most thankful to the Israeli Ministry of Defense and the Israeli Navy for funding my staying in the USA and giving me the opportunity to take part in the MIT experience. I am sure that the knowledge and skills I have gained at MIT will be most beneficial to the Israeli Navy in the coming future.

Last but not least, I would like to express my deepest appreciation and love toward my wife Taly and our kids: Marom, Or and Yahav for their infinite support. Although they have been through hard times during my research, still they gave me the time and space I needed to complete this thesis.

This thesis is dedicated to my beloved parents, Haim and Louise. I owe them more than can be expressed.

Table of Contents

List of Figures

List of Tables

Nomenclature

Symbol	Description	Units
ρ	Density of the fluid	kg/m^3
μ	Dynamic viscosity	kg/(m·sec)
ν	Kinematic viscosity	m^2/sec
Γ	Circulation	m^2/sec
Φ	Total velocity potential	m^2/sec
w	Complex variable	m^2/sec
ψ	Imaginary part magnitude of w	m^2/sec
ψ_0	Average value of ψ	m^2/sec
C	Constant	m^2/sec
x	X-coordinate of the foil	m
y	Y-coordinate of the foil	m
x_{cp}	X-coordinate of the action center of the foil lift	m
y_U	Y-coordinate of the upper surface of the foil	m
y_L	Y-coordinate of the lower surface of the foil	m
z	Complex variable in circle plane	m
z'	Complex variable in noncircular plane	m
ζ	Complex variable in foil plane	m
a	Radius of circle	m
l	Foil chord length	m
η	Foil camber	m
η_0	Maximum foil camber	m
r	Distance from origin	m
γ	Load distribution (vortex strength)	m/sec
U_∞	Uniform stream velocity	m/sec
u	Horizontal velocity disturbance on the foil	m/sec
u_T	Horizontal velocity disturbance on the foil at the tail	m/sec
v	Vertical velocity disturbance on the foil	m/sec

Symbol	Description	Units
M	Total moment	N·m
L	Total lift	N
p_∞	Pressure far away from the foil	Pa
p_f	Pressure on the foil	Pa
p	Relative pressure on the foil	Pa
τ_{ij}	Components of stress tensor	Pa
α	Angle of attack of the foil	deg
β	Phase gap between φ and θ	deg
β_α	Corrected parameter to use instead of β	deg
β_T	Phase gap between φ and θ at the foil tail (angle of zero lift)	deg
φ	Angular coordinate of z	deg
θ	Angular coordinate of z'	deg
Re	Reynolds Number	NA
Fr	Froude Number	NA
c	Foil chord length in percentage	NA
G	Vertical / Horizontal gap between two foils in chord percentage	NA
n	Normal to the foil surface	NA
λ	Middle point of transformation	NA
κ	Lower point of transformation	NA
C_P	Pressure coefficient	NA
C_L	Lift coefficient	NA
C_M	Moment coefficient	NA
ξ	Dummy variable	NA
ε	Dummy variable	NA
F	Dummy variable	NA

Chapter 1 - Introduction

1.1 Ship Design

Ship design and analysis is a complicated process that involves many parameters which affect each other. Some of the major aspects are hull geometry, weight and stability, resistance and powering, seakeeping, structure and cost. All of those parameters govern the dimensions and the form of the ship. Due to a dynamic environment like the ocean, the design of a ship becomes much more sophisticated.

According to [1][1], the growing demand for more efficient marine transportation has produced significant changes in ship sizes, types and production methods. Consequently, many new ship types have appeared during the last few decades, such as: multihull vessels, barge carriers, surface effect ships and hydrofoils.

In order to improve the marine transportation, naval architects and marine engineers have focused on the total drag of the ship. According to [2], the total drag of a ship is divided into three main parts:

- Friction Resistance.
- Wave-Making Resistance.
- Form Resistance.

The last two parts are treated together as the Residual Resistance. While the friction resistance coefficient is given by a formula adopted by the International Towing Tank Conference (ITTC), the residual resistance coefficient is found by making an experiment in a towing tunnel on a scaled-down model. The friction resistance is governed by the *Re* number and the residual resistance is governed by the *Fr* number. The following figure which is taken from [3], describes the total resistance of a ship versus its speed-length ratio:

[1] Numbers in rectangular parentheses represent the reference numbers in the list of references.

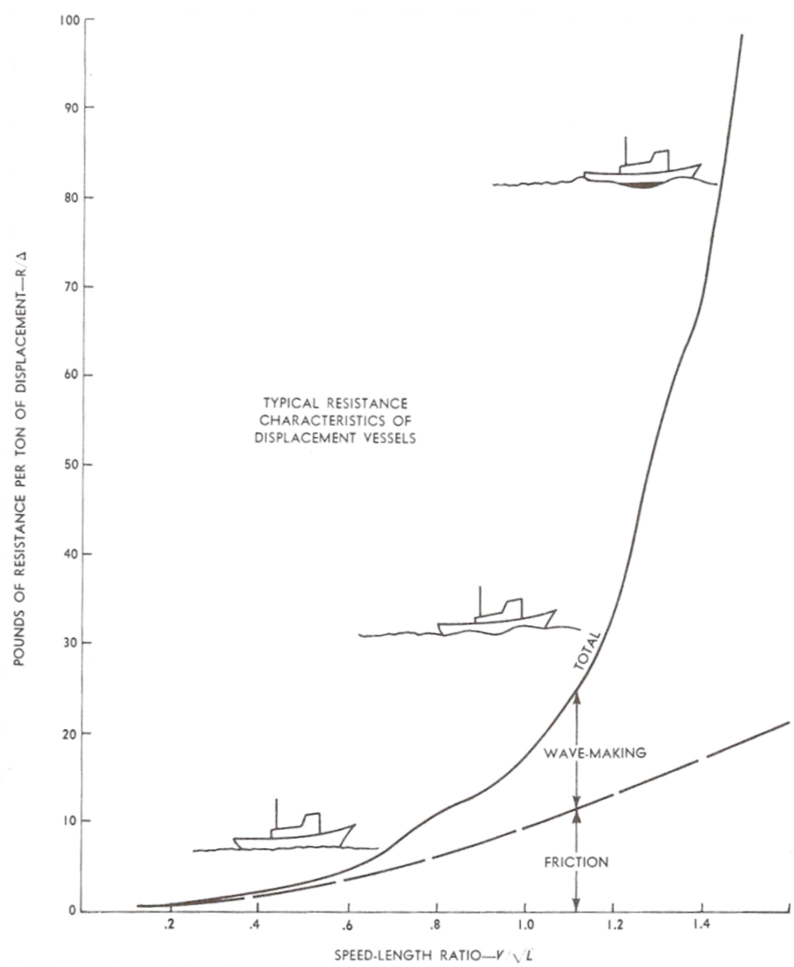

Figure 1. Resistance versus speed-length ratio.

The total drag increases sharply when the speed-length ratio is 1.34. The speed of the hull at this point is referred as the *Hull Speed*. At that point, the wave length is the same as the length of the ship, and the ship 'is trying to climb' on the wave which is going with her and never leaves. At this point, extra power is needed from the machinery system in order to get over this obstacle. Since it is not beneficial to do so, most of the ships do not go faster than their *Hull Speed*. When entering gravity into the speed-length ratio, one gets the *Fr* number. The *Hull Speed* occurs at $Fr = 0.4$.

1.2 Hydrofoil Characteristics

One of the main challenges of a naval architect when designing a ship is to reduce significantly its resistance. Thus, the required power will be lower and that directly influences the total weight of the machinery systems (Gas Turbines, Engines, Gear Boxes, Shafts and Propellers) and of the ship itself. As mentioned above, the resistance of a ship jumps very high when $Fr = 0.4$. However, this is true for a monohull with no hydrofoils.

There are several ways to reduce the resistance of a ship; one of the successful implementations is attaching a hydrofoil to its hull. The most common use of the hydrofoils is between the dummy hulls of multihull vessels. The hydrofoil, which is placed along the vertical axis of the ship under the waterline, produces lift which makes the ship less submerged in the sea. Thus, the submerged part of the ship is reduced and the sail part of the ship is enlarged. Due to density ratio of about 1000 between sea-water and air, the total resistance of the ship is reduced significantly.

Furthermore, not only is the hydrofoil producing lift and reducing the resistance, it is also constraining the two dummy hulls it is in between. Thus it plays a dual role: it acts as a strength member as well, while it reduces the total drag as its main purpose. The following figure illustrates the influence of a hydrofoil on a catamaran. One can see how the ship is lifted when it gets to high speed.

Figure 2. Hydrofoil of a catamaran.

1.3 Objective

The objective of this research is to analyze and find the distributed pressure around two vertical foils (bi-plane) and around two subsequent foils (stagger) where the distance between them is enlarged with relation to their chord length. The analyses will be performed using Computational Fluid Dynamics (CFD).

In order to verify the CFD process and results, a comparison will be made between analytical, experimental and CFD's distributed pressure curves around a single foil (the famous Clark-Y foil). Once the results of the CFD match the analytical solution and more important the experimental results, a mid-stage between the single foil stage and the two foils stages will take place, which analyzes the distributed pressure around the same single foil while stretching it horizontally only.

In between the stages, the CFD models will be analyzed and examined for sensitivity, validity and applicability by changing the boundary conditions, condensing the mesh to find the optimal mesh versus computer resources, plotting the errors of the numeric solutions to find singularities and / or sensitive zones in the model which require refined mesh. Also the streamlines along the foils will be plotted to get a better understanding of the physics.

The Finite Element Software which will be used for the analyses is Automatic Dynamic Incremental Nonlinear Analysis (ADINA). ADINA R & D, Inc. was founded in 1986 by Prof. K. J. Bathe and associates. The exclusive mission of the company is the development of the ADINA System for the analysis of solids, structures, fluids and fluid flow with structural interactions.

Chapter 2 - Theoretical Background

2.1 Two-Dimensional Hydrofoil

Knowing the pressure field around a foil is of vital importance in hydrodynamics. Considering a steady flow over a thin foil (streamlined body), there are two ways to produce lift. One is the angle of attack and the other is the camber of the foil, i.e. it is asymmetric about the horizontal axis. Obviously, those two components of lift can be combined at the same time.

When the angle of attack is small and the foil is thin, there is no separation of the flow even for large Reynolds numbers. The viscous effects are only in a very thin boundary layer around the foil and thus the drag of the foil is due only to the skin friction. Consequently, when the viscosity of the fluid is very small (like for sea water: $\nu \approx 10^{-6}\,\frac{m^2}{sec}$), the drag can be neglected and not taken into consideration.

If there is no separation of the flow and the viscous effect can be neglected (the drag is so small that is second of importance), one can assume a potential flow around the foil in order to solve for the distributed pressure and the lift produced. According to [4], applying only a uniform stream will result in infinite velocity at the trailing edge; such a velocity is not physical and thus cannot take place. The following figure, which is taken from [5], describes the streamlines past a foil when a uniform stream is applied:

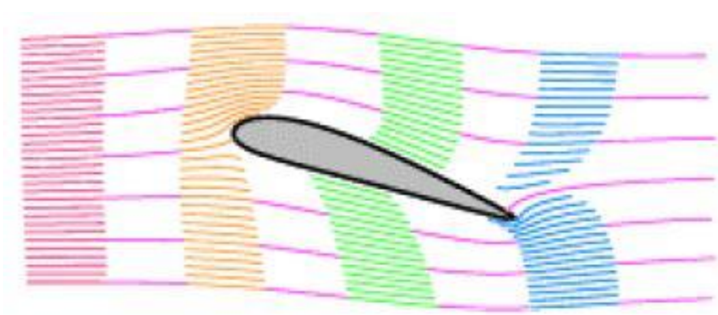

Figure 3. Infinite velocity at the trailing edge.

This infinite velocity violates the Kutta condition which states that **"flow leaves tangentially the trailing edge, i.e., the velocity at the trailing edge is finite"**. In order to satisfy the Kutta condition, one needs to apply circulation in addition to the uniform stream. The following figure describes the circulatory flow:

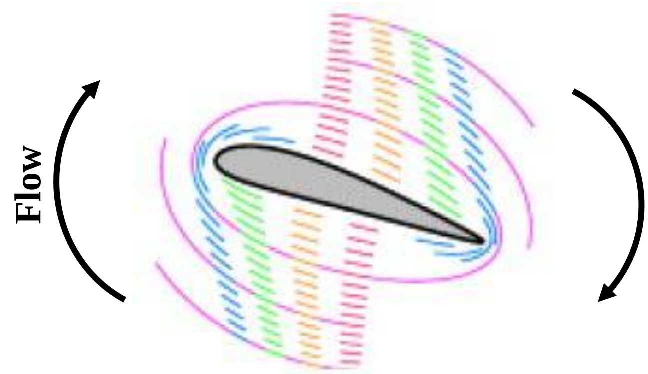

Figure 4. Circulatory flow only.

Consequently, the flow past a foil is combined from uniform stream and circulation as well. The open question is how much circulation to apply? And the answer is until the Kutta condition is satisfied and the velocity at the trailing edge leaves smoothly, as described in the following figure:

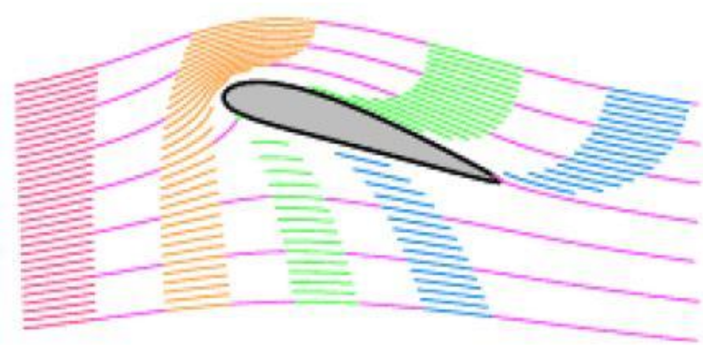

Figure 5. Uniform stream combined with Circulatory.

In actuality, when a foil starts moving, vortices are created due to the separation at the tail (infinite velocity). The vortex shedding continues till the Kutta condition is satisfied and the flow leaves the foil smoothly. The sum of all these vortices is the circulation that has been developed and led to a tangent and finite velocity at the tail.

The velocity of the uniform stream is U_∞ in the x direction and the velocity disturbance due to the foil is given by u and v on the foil at a given point. Thus, using the total velocity potential $\Phi(x, y)$, the flow velocity can be expressed as:

$$(1) \quad \vec{v} = (-U_\infty + u, v) = \nabla\Phi(x, y)$$

One can easily translate the above flow explanation into a mathematical model as the following boundary value problem based on the following figure:

(2) $\nabla^2 \Phi(x, y) = 0,$ as the governing equation.

(3) $\frac{\partial \Phi(x,y)}{\partial n} = 0,$ on the foil.

(4) $\nabla\Phi \rightarrow 0,$ r$\rightarrow$ 0.

(5) $\nabla\Phi < \infty,$ at the trailing edge (Kutta condition).

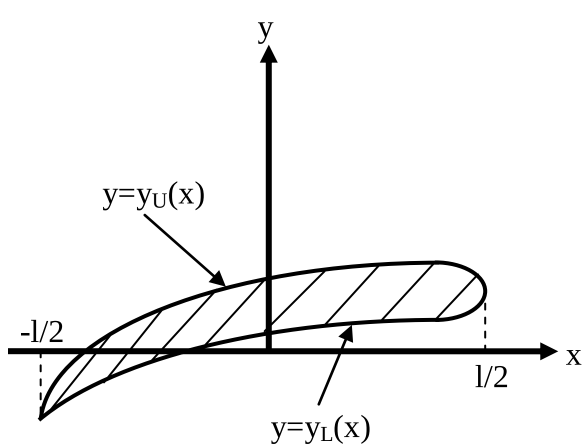

Figure 6. General boundary value problem.

2.2 Developing the Linearized Solution for a Thin Foil

Two main assumptions can be made in order to simplify the equations:

1. The velocity disturbances (u,v) are very small compare to the free stream velocity U_∞, i.e. $\frac{u}{U_\infty}, \frac{v}{U_\infty} \ll 1$.
2. Since the foil is thin, the vertical disturbance v on each of the two surfaces of the foil can be expressed as:

$$(6) \quad v(x, 0_+) = -U_\infty \frac{dy_U}{dx}$$

$$(7) \quad v(x, 0_-) = -U_\infty \frac{dy_L}{dx}$$

The following figure, also taken from [5], describes the linearized problem:

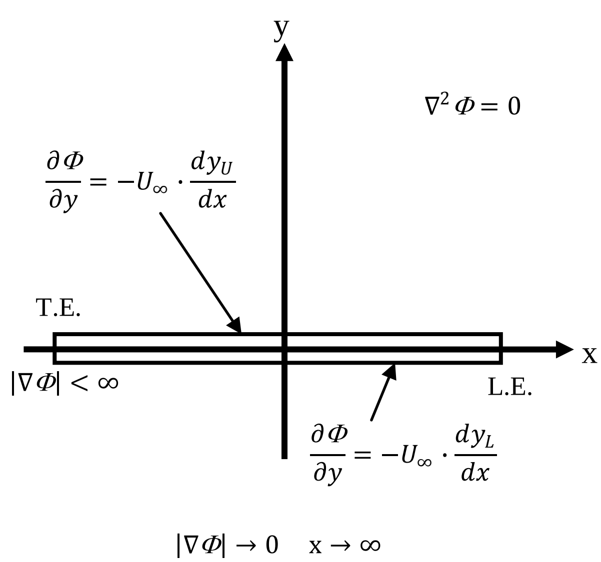

Figure 7. The linearized problem.

Since the mean camber line of the foil is given by:

$$(8) \quad \eta(x) = \frac{1}{2}(y_U(x) + y_L(x))$$

The vertical disturbance v can be expressed for a very thin foil ($y_U \approx y_L$) as:

$$(9) \quad v(x, 0_{\pm}) = -U_{\infty} \frac{d\eta}{dx}$$

The horizontal velocity u along the lower surface is lower than the horizontal velocity along the upper surface; since the pressure behavior is opposite to the velocity, lift is produced. In order to find the lift, vortices are being distributed along the horizontal axis of the foil, as described in the following figure:

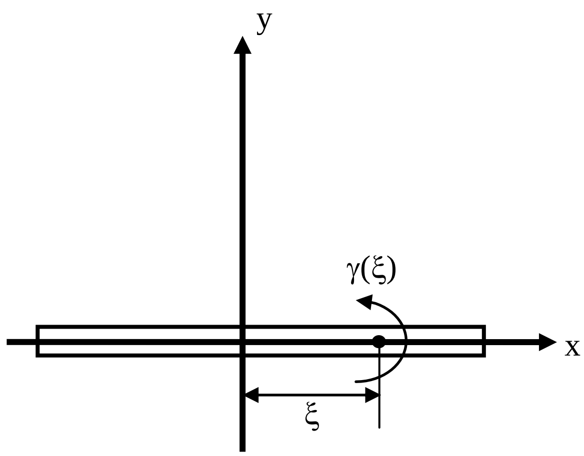

Figure 8. Distributed vortices along the linearized foil.

The potential differential at each vortex is given by:

$$(10) \quad d\Phi(x, y) = \frac{1}{2\pi} \tan^{-1}\left(\frac{y}{x-\xi}\right) \cdot \gamma(\xi)\, d\xi$$

One can find the potential function by integrating this expression over the foil length:

$$(11) \quad \Phi(x, y) = \int_{-\frac{l}{2}}^{\frac{l}{2}} \gamma(\xi) \frac{1}{2\pi} \tan^{-1}\left(\frac{y}{x-\xi}\right) d\xi$$

The boundary condition for this problem then becomes:

$$(12)\qquad \left.\frac{\partial \Phi(x,y)}{\partial y}\right|_{y=0} = \frac{\partial}{\partial y}\left[\int_{-\frac{l}{2}}^{\frac{l}{2}} \gamma(\xi)\frac{1}{2\pi}\tan^{-1}\left(\frac{y}{x-\xi}\right)d\xi\right]_{y=0} = -U_{\infty}\frac{d\eta}{dx}$$

For an analysis of a design, the geometry of the foil is given, i.e. the camber is known, thus one can solve for the load distribution γ. Since the horizontal velocity disturbance u is very small compared to U_{∞} and the foil is considered to be very thin, the relation between the horizontal disturbance u and the load distribution γ is given by:

$$(13)\qquad u(x,\varepsilon) \cong \mp\frac{1}{2\pi}\gamma(x)\int_{-\frac{l}{2}}^{\frac{l}{2}}\frac{\varepsilon}{(x-\xi)^2+\varepsilon^2}\mathrm{d}\xi = \mp\frac{1}{2\pi}\gamma(x)\left[\tan^{-1}\left(\frac{\xi-\mathrm{x}}{\varepsilon}\right)\right]_{-l/2}^{l/2}$$

$$\cong \mp\frac{\gamma(x)}{2}$$

Applying the Bernoulli equation along a streamline between infinity and a point on the foil, one should obtain:

$$(14)\qquad p_f - p_{\infty} = -\frac{1}{2}\rho\left(|\vec{v}|^2 - {U_{\infty}}^2\right) = -\frac{1}{2}\rho\left\{\left[(u - U_{\infty})^2 + v^2\right] - {U_{\infty}}^2\right]\right\} =$$

$$= -\frac{1}{2}\rho(u^2 - 2\cdot u\cdot U_{\infty} + v^2) = -\frac{1}{2}\rho\cdot u\cdot U_{\infty}\cdot\left(\frac{u}{U_{\infty}} - 2 + \frac{v}{u}\cdot\frac{v}{U_{\infty}}\right)$$

Since $\frac{u}{U_{\infty}}, \frac{v}{U_{\infty}} \ll 1$ and also $\frac{u}{v}\sim 1$, equation (14) becomes:

$$(15)\qquad p_f - p_{\infty} = \rho\cdot u\cdot U_{\infty}$$

Consequently, integrating equation (15) along the foil for computing the lift:

$$(16)\quad L = \int_{-l/2}^{l/2} \left[\left(p_f(x,0_-) - p_\infty\right) - \left(p_f(x,0_+) - p_\infty\right)\right] dx$$

$$= \rho \cdot U_\infty \cdot \int_{-l/2}^{l/2} [u(x,0_-) - u(x,0_+)] dx$$

The combination of equation (13) and equation (16) leads to the total lift equation:

$$(17)\quad L = \rho \cdot U_\infty \cdot \int_{-l/2}^{l/2} \gamma(x) dx = \rho \cdot U_\infty \cdot \Gamma$$

According to the linear lift theory as detailed in [4], the lift coefficient can be defined as:

$$(18)\quad C_L = \frac{L/span}{\frac{1}{2} \cdot \rho \cdot {U_\infty}^2 \cdot l} = \frac{4}{l} \int_{-l/2}^{l/2} \frac{d\eta}{d\xi} \left[\frac{\frac{l}{2} - \xi}{\frac{l}{2} + \xi}\right]^{1/2} d\xi = \frac{\int_{-l/2}^{l/2} \gamma(x) \cdot x \cdot dx}{\Gamma}$$

For small angles of attack, the lift coefficient can be simply approximated as:

$$(19)\quad C_L = 2\pi\alpha + 4\pi \frac{\eta_0}{l}$$

where η_0 is the maximum camber of the foil.

The center of action of the equivalent lift on the foil is derived by the relation of the total moment to the total lift. The total moment, with respect to the middle of the foil, is given by:

$$(20)\quad M = \rho \cdot U_\infty \cdot \int_{-l/2}^{l/2} \gamma(x) \cdot x \cdot dx = 2 \cdot \rho \cdot {U_\infty}^2 \cdot \int_{-l/2}^{l/2} \frac{d\eta}{d\xi} \left[\frac{l^2}{4} - \xi^2\right]^{1/2} d\xi$$

And the center of action (measured from the mid-chord) is:

$$(21)\quad X_{cp} = \frac{M}{L} = \frac{\int_{-l/2}^{l/2} \gamma(x) \cdot x \cdot dx}{\Gamma}$$

The moment coefficient is given by:

$$(22)\quad C_M = \frac{M/span}{\frac{1}{2} \cdot \rho \cdot {U_\infty}^2 \cdot l^2}$$

2.3 Developing the Analytical Solution for an Arbitrary Foil

When the foil has finite thickness and cannot be treated as a thin foil, a different and more general approach should be used. For a frictionless incompressible fluid flow past a streamlined hydrofoil of an arbitrary form, the velocity on each point can be expressed by an exact expression. Thus, the pressure along the upper and lower surfaces can be easily derived. It is interesting to note that the governing parameters are functions of form only.

The detailed procedure is presented in [6] which includes experimental results for verifying the theory. The theoretical and experimental pressure curves along the foil are almost perfectly matched. This mathematical procedure is also given in [7] with additional empirical modification of the theory which makes the curves perfectly matched.

The main steps of this mathematical procedure are given in this chapter in order to explain the essence of the process. In order to go thoroughly through the calculations, one should refer to [7]. The idea is to solve a potential flow around a circle and then to use the conformal transformation method to relate each point of the circle to a unique point on the foil. The following figure explains this transformation:

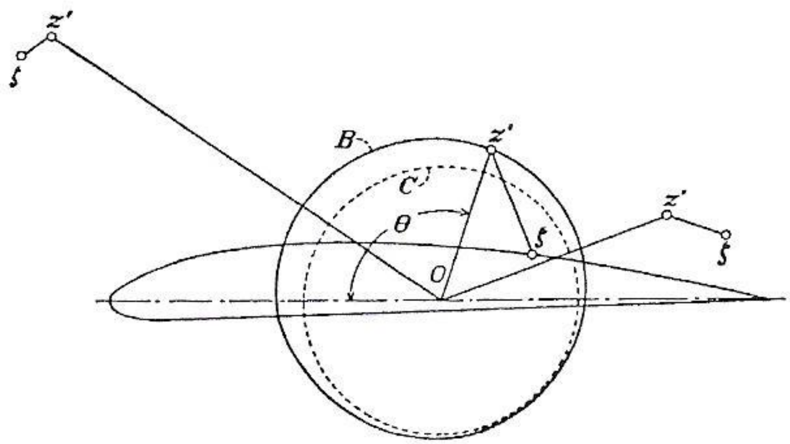

Figure 9. Transformation from a circle to noncircular curve into an arbitrary foil.

Solving a potential flow around a circular rotor is done by combining some simple potential flows such as a source at the origin of the circle, a dipole at origin oriented in the $+x$ direction, vortex at the origin representing the circulation and a uniform stream parallel to x axis. The expression for the 2D flow in terms of complex variables is then:

$$(23) \quad w = U_\infty \cdot \left(z + \frac{a^2}{z}\right) + \frac{i \cdot \Gamma}{2\pi} \cdot \ln\left(\frac{z}{a}\right) + C$$

The circle plane is defined as the “z-Plane” where the polar coordinates are r and φ. The radius vector r is given by:

$$(24) \quad r = a \cdot e^{\psi_0}$$

The variable a represents the radius of the circle and ψ_0 is given by:

$$(25) \quad \psi_0 = \frac{1}{2\pi}\int_0^{2\pi} \psi \, d\varphi$$

The noncircular curve plane is defined as the "z'-Plane". The transformation between the two planes is given by:

$$(26) \quad z' = z \cdot e^{\psi - \psi_0 + i(\theta - \varphi)}$$

Applying De Moivre's theorem, one can easily obtain the following two equations representing the real and imaginary parts of the powers:

$$(27) \quad \psi - \psi_0 = \sum_{i=0}^{n} [\frac{A_n}{r^n}\cos n_\varphi + \frac{B_n}{r^n}\sin n_\varphi]$$

$$(28) \quad \theta - \varphi = \sum_{i=0}^{n} [\frac{B_n}{r^n}\cos n_\varphi - \frac{A_n}{r^n}\sin n_\varphi]$$

Where the coefficients $\frac{A_n}{r^n}$ and $\frac{B_n}{r^n}$ are determined by:

$$(29) \quad \frac{A_n}{r^n} = \frac{1}{\pi}\int_0^{2\pi} \psi \cdot \cos n_\varphi \, d\varphi$$

$$(30) \quad \frac{B_n}{r^n} = \frac{1}{\pi}\int_0^{2\pi} \psi \cdot \sin n_\varphi \, d\varphi$$

The foil plane is defined as the "ζ-Plane", where each point on the foil is given by:

(31) $\zeta = x + iy$

The transformation between the noncircular curve plane (z') and the foil plane is:

(31) $\zeta = z' + \frac{a^2}{z'}$

Combining and solving all the above, the following main equations and relations are obtained:

(32) $x = 2a \cdot \cosh\psi \cdot \cos\theta$

(33) $y = 2a \cdot \sinh\psi \cdot \sin\theta$

(34) $u(x,y) = \frac{dw}{dz} \cdot \frac{dz}{dz'} \cdot \frac{dz'}{d\zeta} = U_\infty \cdot \frac{[\sin(\alpha+\theta+\beta)+\sin(\alpha+\beta_T)]\cdot\left(1+\frac{d\beta}{d\theta}\right)\cdot e^{\psi_0}}{\sqrt{(\sinh^2\psi+\sin^2\theta)\cdot[1+\left(\frac{d\psi}{d\theta}\right)^2]}}$

(35) $u(x,y)_T = U_\infty \cdot \frac{e^{\psi_0}\cdot\left(1+\frac{d\beta}{d\theta}\right)^2}{1+\left(\frac{d\psi}{d\theta}\right)^2}$ (at the tail of the foil).

(36) $\Gamma = 4\pi \cdot U_\infty \cdot r \cdot \sin(\alpha + \beta_T)$

(37) $\mathrm{F} = \frac{\left(1+\frac{d\beta}{d\theta}\right)\cdot e^{\psi_0}}{\sqrt{(\frac{y}{2a\cdot\sin\theta})^2+\sin^2\theta)\cdot[1+\left(\frac{d\psi}{d\theta}\right)^2]}}$

(38) $\frac{u(x,y)}{U_\infty} = \mathrm{F} \cdot [\sin(\alpha + \theta + \beta) + \sin(\alpha + \beta_T)]$

The solution we are after is a dimensionless pressure distribution (C_P) along the foil which is derived by the Bernoulli equation for a steady-state flow:

$$(39)\quad p_f + \frac{1}{2}\rho \cdot u(x,y)^2 = p_\infty + \frac{1}{2}\rho \cdot {U_\infty}^2$$

$$(40)\quad p_f - p_\infty + \frac{1}{2}\rho \cdot u(x,y)^2 = \frac{1}{2}\rho \cdot {U_\infty}^2 \equiv q$$

$$(41)\quad p = p_f - p_\infty$$

$$(42)\quad \frac{p}{q} + \frac{u(x,y)^2}{{U_\infty}^2} = 1$$

$$(43)\quad C_p = \frac{p}{q} = 1 - \left(\frac{u(x,y)}{U_\infty}\right)^2$$

The parameter *a* is determined by the chord length of the foil (geometric form only) as described in the following figure which is taken from [6]:

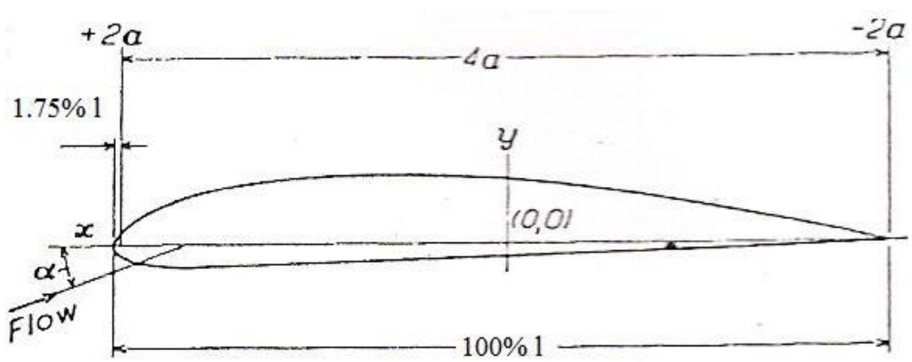

Figure 10. Determination of the parameter *a*.

As mentioned above, this theory was modified empirically since there are boundary layer effects which were not taken into consideration. According to the modified theory which is described in [8], the correction is made by distorting the shape of the section. This distortion is achieved by finding an increment $\Delta\beta_T$ which adjusts the circulation but still avoids infinite velocity at the trailing edge. Thus, instead of β, one should use:

$$(44) \quad \beta_\alpha = \beta + \frac{\Delta\beta_T}{2}(1 - \cos\theta)$$

Chapter 3 - Finite Elements Formulation

3.1 The Process of Finite Element Analysis

Solving for a pressure field around an arbitrary body in a flow field is very meaningful for many physical applications. Many engineering issues consist of a flow around a body, for example: a flying airplane, a ship at seaway, wind influence on structures, flow in veins etc. Thus, it is most important to find the velocity and pressure fields on a body in as short a time as possible with adequate resources.

Since it is complicated and sometimes impossible to find an analytical solution, but still essential to find a solution, the Finite Element Method (FEM) is used. The FEM is a powerful tool for solving physical problems in many scientific fields. The physical problem involves a structure or a control volume, with known material properties, subjected to certain loads and boundary conditions. Since the FEM is a computational tool based on a mathematical model, certain assumptions are made to idealize the physical problem to a mathematical model.

The FEM, in general, divides the control volume into many small (but finite) elements where the shared points of the elements are called nodes. The algorithm runs over the nodes until the equilibrium criteria are achieved in every node. The FEM is called Computational Fluid Dynamics (CFD) when a flow field is involved. The CFD method is very time consuming and requires extensive computational resources since a solution must be achieved all over the control volume of the problem and not just around the body itself. Thus, the mesh of the control volume becomes very sophisticated and has many elements. Consequently, even when high-speed supercomputers are used, it might take a few days to get a solution. Since the finite element solution is obtained numerically, some error is produced. Although this error can be reduced by refining the solution parameters (finer mesh, smaller time steps in transient or non-linear analysis, etc.) - the solution can never be an exact one but only an accurate one. In addition, since the mathematical model is solved rather than the physical one, one cannot expect more information on the physical phenomena than what has just been obtained.

One should pay close attention when using the FEM. The modern FEM integrates CAD software for graphic illustrations capabilities. Based on a user-friendly interface, the FEM code looks very aesthetic, colorful and easy to use. Nothing can be further from the truth as this illusion. This powerful tool, used by non adequate personnel, may lead to false results and destructive decisions. It is for this reason that professionals say that CFD is also Colorful Fluid Dynamics as it is very deceiving if improper use is made.

3.2 The Principle of Virtual Work

The principle of virtual work is used as the basis of the finite element solution. The derivation of this principle appears in numerous finite elements textbooks and it states the following:

Given a 3D domain with volume V, total surface area S, prescribed velocity on part of the area S_v and subjected to surface tractions f^{Sf} on the surface area S_f (such that $S_v \cap S_f = 0$ and $S_v \cup S_f = S$). In addition, the domain is subjected to externally applied body forces f^B per unit volume. Then, for this given domain, the following equation which given in [9] is valid:

$$(45) \quad \int_v \bar{v}_i \cdot \rho\left(\bar{v}_i + v_{i,j} \cdot v_j\right) dV + \int_v \bar{e}_{ij} \cdot \tau_{ij}\, dV = \int_v \bar{v}_i \cdot f_i^B\, dV + \int_{s_f} \bar{v}_i^s \cdot f_i^s\, dS$$

Since this equation, which describes the momentum of the continuum mechanics, has 3 equations but 4 unknowns (velocity in 3 directions and the pressure), the following continuity equation gives the 4th dimension and gives the problem a closure solution:

$$(46) \quad \int_v \bar{p} \cdot v_{i,i}\, dV = 0$$

where $\bar{v}$ and $\bar{p}$ are virtual velocities and pressure respectively, τ_{ij} and $\bar{e}_{ij}$ are given by:

$$(47) \quad \tau_{ij} = -p \cdot \delta_{ij} + 2\mu \cdot e_{ij}$$

$$(48) \quad e_{ij} = \frac{1}{2}\left(\frac{\partial v_i}{x_j} + \frac{\partial v_j}{x_i}\right)$$

and δ_{ij} is the Kronecker delta function.

3.3 Equilibrium Equations in Fluid Flows Analysis

In the finite element analysis, the control volume is approximated as an assemblage of *m* discrete finite elements interconnected at nodal points on the element boundaries. For every element *m*, there is a velocity interpolation matrix H and a pressure interpolation matrix $\widetilde{H}$. In two dimensional planar flow, those matrices are:

$$(49) \quad v^{(m)}(y,z) = H^{(m)}(y,z) \cdot \hat{V}$$

$$(50) \quad p^{(m)}(y,z) = \widetilde{H}^{(m)}(y,z) \cdot \hat{P}$$

where $\hat{V}$ and $\hat{P}$ are vectors of the two global velocities components and the global pressure component respectively. The stiffness matrices $K_{\mu v_2 v_2}$, $K_{\mu v_2 v_3}$, $K_{\mu v_3 v_3}$, $K_{v v_2}$, $K_{v v_3}$, $K_{v_2 p}$ and $K_{v_3 p}$ are obtained by the following terms:

$$(51) \quad K_{\mu v_2 v_2} = \int_v (2\mu \cdot H^T_{,x_2} \cdot H_{,x_2} + \mu \cdot H^T_{,x_3} \cdot H_{,x_3}) dV$$

$$(52) \quad K_{\mu v_2 v_3} = \int_v (\mu \cdot H^T_{,x_3} \cdot H_{,x_2}) dV$$

$$(53) \quad K_{\mu v_3 v_3} = \int_v (2\mu \cdot H^T_{,x_3} \cdot H_{,x_3} + \mu \cdot H^T_{,x_2} \cdot H_{,x_2}) dV$$

$$(54) \quad K_{vv_2} = K_{vv_3} = \rho \int_v (H^T \cdot H\hat{V}_2 \cdot H_{,x_2} + H^T \cdot H\hat{V}_3 \cdot H_{,x_3}) dV$$

$$(55) \quad K_{v_2 p} = -\int_v (H^T_{,x_2} \widetilde{H}) dV$$

$$(56) \quad K_{v_3 p} = -\int_v (H^T_{,x_3} \widetilde{H}) dV$$

where $H_{,x_2}$ and $H_{,x_3}$ are obtained by appropriately differentiating rows of the matrix $H^{(m)}$ with respect to their own index, i.e. $H_{,x_2}$ is differentiating $H^{(m)}$ with y-coordinate).

The other side of the equation has the body loads R_B and the surface tractions R_S. Those are given by:

$$(57) \quad R_B = \int_v H^T f^B dV$$

$$(58) \quad R_S = \int_{S_f} H^{ST} f^S dS$$

The fundamental relationship for a specific element that links the velocities and the pressure, the stiffnesses and the loads is:

$$(59)\quad \left(K_{\mu vv} + K_{vv}\right)\hat{V} + K_{vp}\hat{P} = R_B + R_S$$

and in matrix form for a 2D fluid flow:

$$(60)\quad \begin{bmatrix} K_{\mu v_2 v_2} + K_{vv_2} & K_{\mu v_2 v_3} & K_{v_2 p} \\ K^T_{\mu v_2 v_3} & K_{\mu v_3 v_3} + K_{vv_3} & K_{v_3 p} \\ K^T_{v_2 p} & K^T_{v_3 p} & 0 \end{bmatrix} \cdot \begin{bmatrix} \hat{V}_2 \\ \hat{V}_3 \\ \hat{P} \end{bmatrix} = \begin{bmatrix} R_{B2} + R_{S2} \\ R_{B3} + R_{S3} \\ 0 \end{bmatrix}$$

It should be noted that the above equations are applicable for a 2D steady state, incompressible viscous fluid flows only. Otherwise, for a more general fluid flow (3D flow, transient flow, flow with heat transfer) - more components should be added to equation (60). For further and detailed information one should look into [9].

3.4 Element type study

The CFD procedures are more sophisticated than those of structures methods. In a 3D structure model all there is to mesh and solve is the structure itself with the loads applied on it. On the other hand, the entire domain should be meshed around the body itself when solving a 2D flow problem. Thus, the number of elements of the meshed model is much larger than the number of elements for a structure. In order to solve a 2D flow problem, it takes time and special resources. In order to solve a 3D flow problem, it gets way too complicated. Thus, a lot of effort is invested in looking for procedures and element-types that are stable and give an accurate solution, but at the same time significantly reduce the time consumption of the process.

In order to reduce the time of a process, the algorithm of solving the CFD equations has to be simplified. One of the approaches is to change the interpolation procedure of the equations in order to get a more stable and accurate solution in each node of the meshed model. According to [10], there are many techniques for solving fluid flow problems. A very important and developed procedure is the flow-condition-based interpolation (FCBI). This interpolation has two meaningful aspects which are stability and flux equilibrium.

Another approach is to use a higher-order finite element with more nodes. This will provide a more accurate solution. A formulation of 9-node FCBI finite element is presented in [11]. According to this article, an effective fluid flow analysis was obtained in several cases using coarse meshes. Like in structural analyses, the 9-node element is a very good candidate for error assessment although it takes more time for the computer to solve the model. The article states that the element was examined for 2D flow, but may be employed to 3D analyses as well.

A study of a 2D flow, where the cubic interpolated polynomial (CIP) method is used with 4-node and 9-node finite elements, is detailed in [12]. The reason for using the CIP method is to stabilize the convective terms of the CFD equations. The goal is to make a coarse mesh of the model in order to save time in solving the equations but to still get an accurate solution. According to [12], the 4-node and 9-node elements show accurate and stable solutions, but were too expensive in the applications. It took too much time to get the solution. In addition, the authors state that the article results are based on numerical procedures and not on mathematical-analytical ones.

Consequently, in order to reduce the time of the solution and still get an accurate, stable and converged model, I have used the 4-node FCBI finite element in ADINA for the fluid flow models in this research.

Chapter 4 - Single Foil Analysis

4.1 The Geometry of the Model

The foil section that all the analyses were made on is the Clark-Y foil. The foil section coordinates are given in [6] for both the upper surface and the lower surface versus the x-coordinate. The following table shows those coordinates:

Table 1. Clark-Y foil coordinates from [6].

c	x	y_U	y_L
0	0	0.000	0.000
1.25	0.05	0.0803	-0.0618
2.5	0.101	0.124	-0.0787
5	0.202	0.185	-0.0961
7.5	0.303	0.226	-0.105
10	0.404	0.260	-0.110
15	0.605	0.311	-0.115
20	0.807	0.345	-0.112
30	1.211	0.373	-0.0997
40	1.614	0.375	-0.0856
50	2.0175	0.353	-0.0718
60	2.421	0.314	-0.0557
70	2.825	0.255	-0.0416
80	3.228	0.181	-0.0299
90	3.631	0.097	-0.0161
95	3.833	0.050	-0.0097
100	4.036	0.002	-0.002

When a CFD analysis is performed, a well defined geometry should be used; especially a more detailed geometry is needed at the leading edge of the foil. Otherwise, the results obtained will not be physical and will not make sense. Using the above table for solving the flow around the foil for the pressure distribution, one would get the following results:

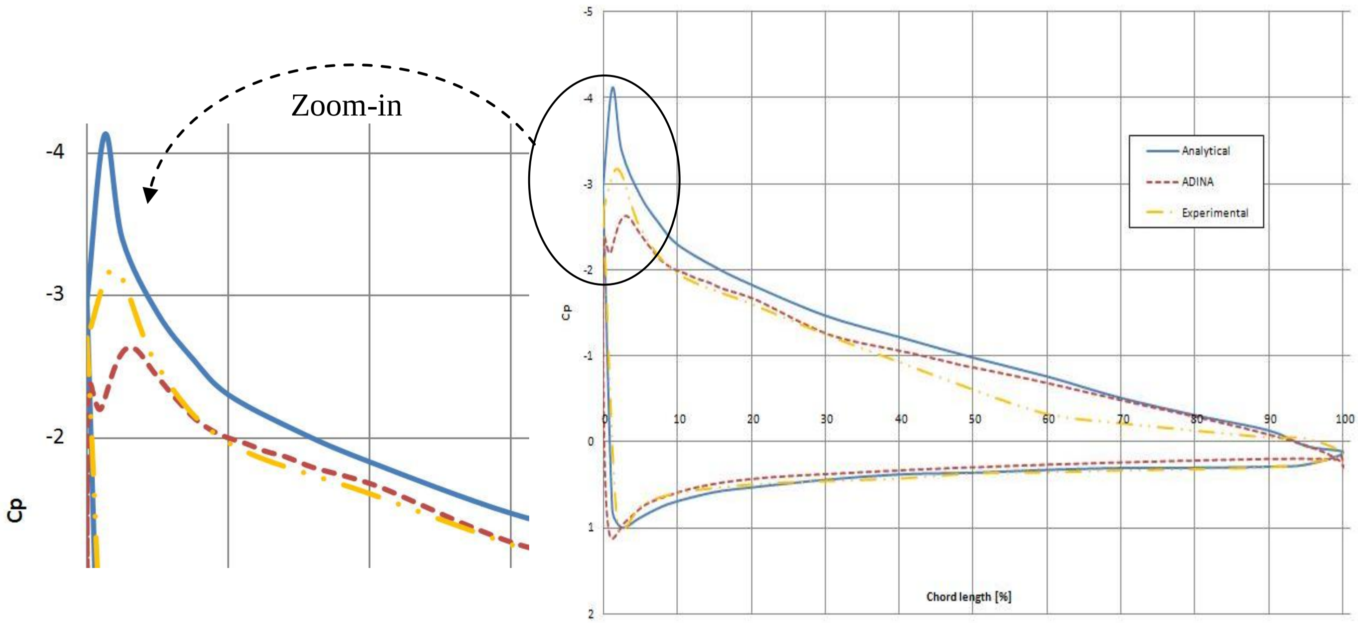

Figure 11. Pressure distribution along the foil using points from [6].

One can see that the results obtained with ADINA (the red dashed curve) are not physical at all. There is a jump in the pressure at the very beginning of the foil, i.e. at the leading edge. Thus, I have continued to look for detailed geometry with many points. Reference [13] also does not give enough points; therefore the search for detailed data has led to the Airfoil Design Workshop software [14] that has 142 points of the section. Surprisingly, solving the flow field using this reference gave the same results as above. Looking into the geometry of the foil, it has turned out that the geometry of the foil is problematic at the leading edge, and reference [14] has only extrapolated many points along the curve without encountering the same geometry problem.

Since the flow around the foil and especially at the leading edge is very sensitive to the curvature of the foil and the above results show that the pressure distribution curve is not physical, the following step of investigating the geometry of the section has taken place. Calculating and plotting the second derivative of the upper surface of the foil (y_u) revealed a surprising finding at the first 10 percent of the chord length. The following figure describes this finding:

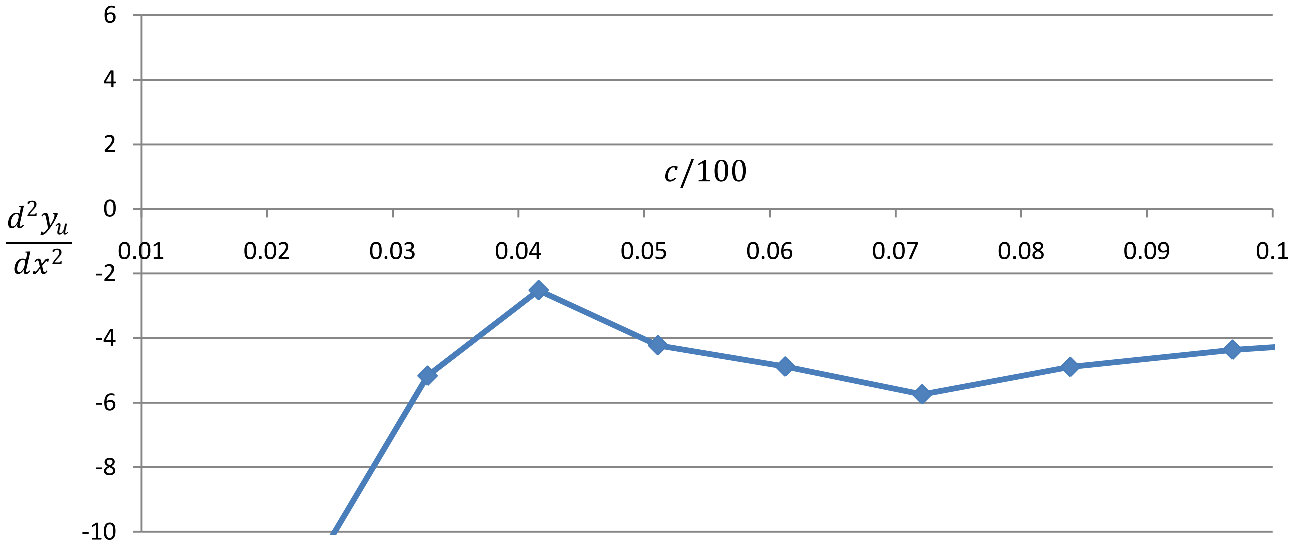

Figure 12. Plotting the 2nd derivative of the upper surface of the foil.

According to this figure, one can see that the curvature is decreasing moving away from the leading edge, but at 4% of the chord length it is <u>increasing</u> until 7% of the chord length and then decreasing again. This twist in the curvature is exactly what we get in the pressure distribution, i.e. this twist in the curvature is reflected in the same location (~4%) where we get the distortion in pressure distribution curve along the foil. Surprisingly, this finding was not discovered before; no one got into such refined resolution as needed in CFD. All the experiments and analyses made in the past using this foil skipped that phenomenon due to the coarse increments used. There was not any necessity to find the pressure at ~4% of the chord length. However, this is not valid in CFD analysis where a mathematical model is being solved by computer in a very refined and sequential way.

In order to build the correct curve with a monotonic and smooth curvature (second derivative) moving away from the leading edge, I have used the Unigraphics software [15] which is an important design tool in use of the Israeli Navy. The following figures represent the section view of the foil before and after the correction. In addition, a 3D view of the foil is given as modeled in Unigraphics:

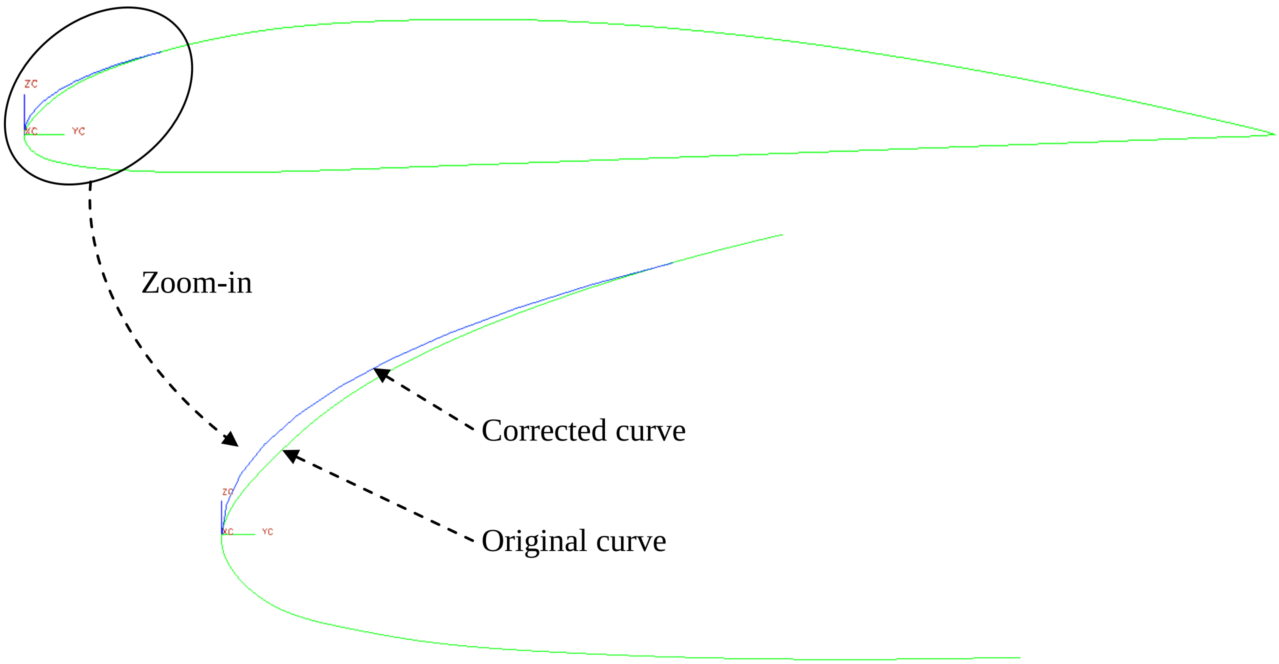

Figure 13. Correction of the Clark-Y foil section using Unigraphics.

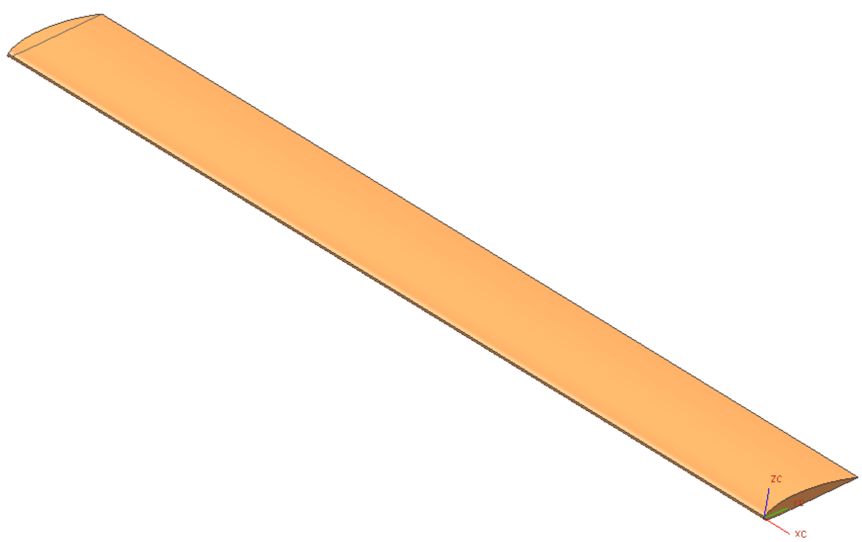

Figure 14. 3D view of the revised Clark-Y foil using Unigraphics.

The new geometry of the foil is given in the following two tables. The first table describes the upper surface (y_U) with the new points of the revised foil section and the second table describes the lower surface (y_L) geometry:

Table 2. Detailed Clark-Y foil coordinates using Unigraphics - upper surface.

x	y_U	x	y_U	x	y_U
0	0	0.80680	0.33090	3.56193	0.10998
0.00085	0.01261	0.88090	0.33965	3.64858	0.09133
0.00210	0.01983	0.95794	0.34744	3.73447	0.07241
0.00589	0.03321	1.03757	0.35417	3.81927	0.05323
0.01110	0.04554	1.11947	0.35979	3.90249	0.03394
0.01744	0.05701	1.20313	0.36423	3.98357	0.01485
0.02470	0.06777	1.28813	0.36743	4.036	0.00242
0.03277	0.07795	1.37389	0.36936		
0.04161	0.08771	1.46006	0.37000		
0.05110	0.09703	1.54643	0.36921		
0.06123	0.10602	1.63301	0.36748		
0.07212	0.11485	1.71974	0.36457		
0.08391	0.12363	1.80668	0.36054		
0.09682	0.13250	1.89385	0.35545		
0.11099	0.14150	1.98119	0.34944		
0.12649	0.15064	2.06869	0.34245		
0.14352	0.15998	2.15631	0.33467		
0.16221	0.16950	2.24394	0.32599		
0.18267	0.17920	2.33164	0.31646		
0.20515	0.18913	2.41938	0.30605		
0.22993	0.19931	2.50716	0.29483		
0.25725	0.20975	2.59503	0.28276		
0.28744	0.22045	2.68301	0.27001		
0.32078	0.23141	2.77108	0.25653		
0.35759	0.24259	2.85922	0.24244		
0.39827	0.25397	2.94737	0.22775		
0.44319	0.26552	3.03552	0.21254		
0.49263	0.27713	3.12362	0.19671		
0.54676	0.28868	3.21165	0.18037		
0.60552	0.30001	3.29955	0.16350		
0.66872	0.31095	3.38729	0.14610		
0.73596	0.32130	3.47479	0.12826		

Table 3. Detailed Clark-Y foil coordinates using Unigraphics - lower surface.

x	y_L	x	y_L	x	y_L
0	0	0.82577	-0.11930	3.57150	-0.01949
0.00004	-0.00965	0.90140	-0.11725	3.65690	-0.01635
0.00202	-0.01885	0.97998	-0.11470	3.74141	-0.01324
0.00597	-0.02793	1.06094	-0.11184	3.82463	-0.01017
0.01146	-0.03657	1.14372	-0.10873	3.90612	-0.00718
0.01824	-0.04480	1.22783	-0.10554	3.98507	-0.00428
0.02615	-0.05255	1.31287	-0.10235	4.036	-0.00242
0.03511	-0.05981	1.39860	-0.09920		
0.04508	-0.06655	1.48476	-0.09606		
0.05610	-0.07249	1.57130	-0.09291		
0.06825	-0.07765	1.65799	-0.08976		
0.08141	-0.08201	1.74488	-0.08657		
0.09557	-0.08581	1.83182	-0.08338		
0.11071	-0.08911	1.91888	-0.08020		
0.12681	-0.09238	2.00593	-0.07697		
0.14404	-0.09577	2.09307	-0.07378		
0.16241	-0.09912	2.18017	-0.07059		
0.18219	-0.10235	2.26734	-0.06736		
0.20350	-0.10534	2.35448	-0.06417		
0.22658	-0.10800	2.44166	-0.06098		
0.25168	-0.11030	2.52880	-0.05776		
0.27905	-0.11232	2.61597	-0.05457		
0.30904	-0.11414	2.70311	-0.05138		
0.34197	-0.11583	2.79029	-0.04819		
0.37817	-0.11753	2.87743	-0.04496		
0.41813	-0.11910	2.96452	-0.04177		
0.46220	-0.12043	3.05162	-0.03858		
0.51080	-0.12144	3.13864	-0.03540		
0.56423	-0.12205	3.22561	-0.03217		
0.62259	-0.12221	3.31243	-0.02898		
0.68584	-0.12181	3.39912	-0.02583		
0.75372	-0.12084	3.48549	-0.02264		

4.2 Loading and Boundary Conditions

The CFD model is a 2D domain of sea water where the Clark-Y foil is standing in the middle of the domain. Since the flow runs from left to right, the uniform stream velocity U_∞, which is set to $1\frac{m}{sec}$, is applied along the left curves of the domain. Along the upper and lower curves of the foil, the FREE slip condition was applied. Consequently, the model becomes independent with *Re* number since there are no separation of the flow and the flow becomes a potential one.

For the given geometry, 4 different angles of attack have been analyzed as performed in [6]: +9.55°, +5.32°, -1.27° and -3.25°. All of those cases were analyzed analytically as well and the results of the distributed pressure along the foil were compared between ADINA results, analytical results and experimental results which are given in [6].

4.3 The CFD Meshed Model

One should notice that, although a potential flow is solved by the Laplace equation in 2D which also applies to heat transfer, one cannot use the thermal module of ADINA (called ADINA-T) for solving the flow around the foil. The reason for that is that vorticity vanishes in this case as stated in [9]:

(61) $$\frac{\partial v_x}{\partial y} - \frac{\partial v_y}{\partial x} = 0$$

Since vorticity vanishes, the Kutta condition will not be satisfied as explained above. Thus, infinity values will be obtained which are not physical. Consequently, the CFD module of ADINA (called ADINA-F) was used in this research.

Meshing the domain around the foil and applying the boundary conditions of FREE slip condition along the foil leads to the following meshed model (22,230 elements):

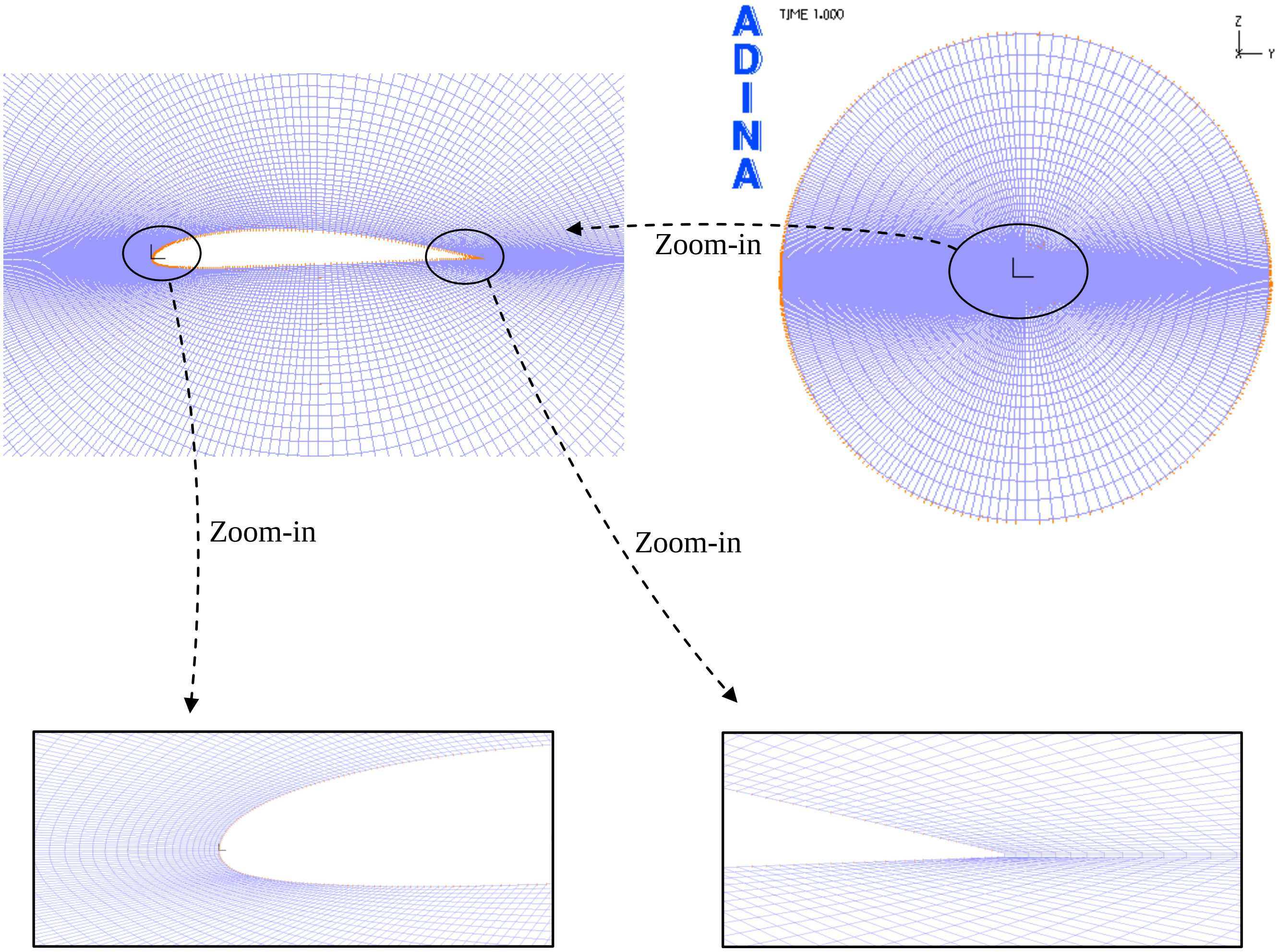

Figure 15. Meshing the 2D domain in ADINA for a single foil.

4.4 The CFD Results

Solving the model for each of the 4 angles of attack, the following solution is obtained. For each angle, the pressure field (figure 16) and the velocity profile (figure 17) around the foil are plotted. These plots are for understanding the distributed pressure and the velocity profile behavior around the foil for each angle of attack. In addition, a color scale with values is given in the figures. It is noted that the nodal pressure is plotted and not the dimensionless pressure (C_P), the relation between them can be obtained from (43).

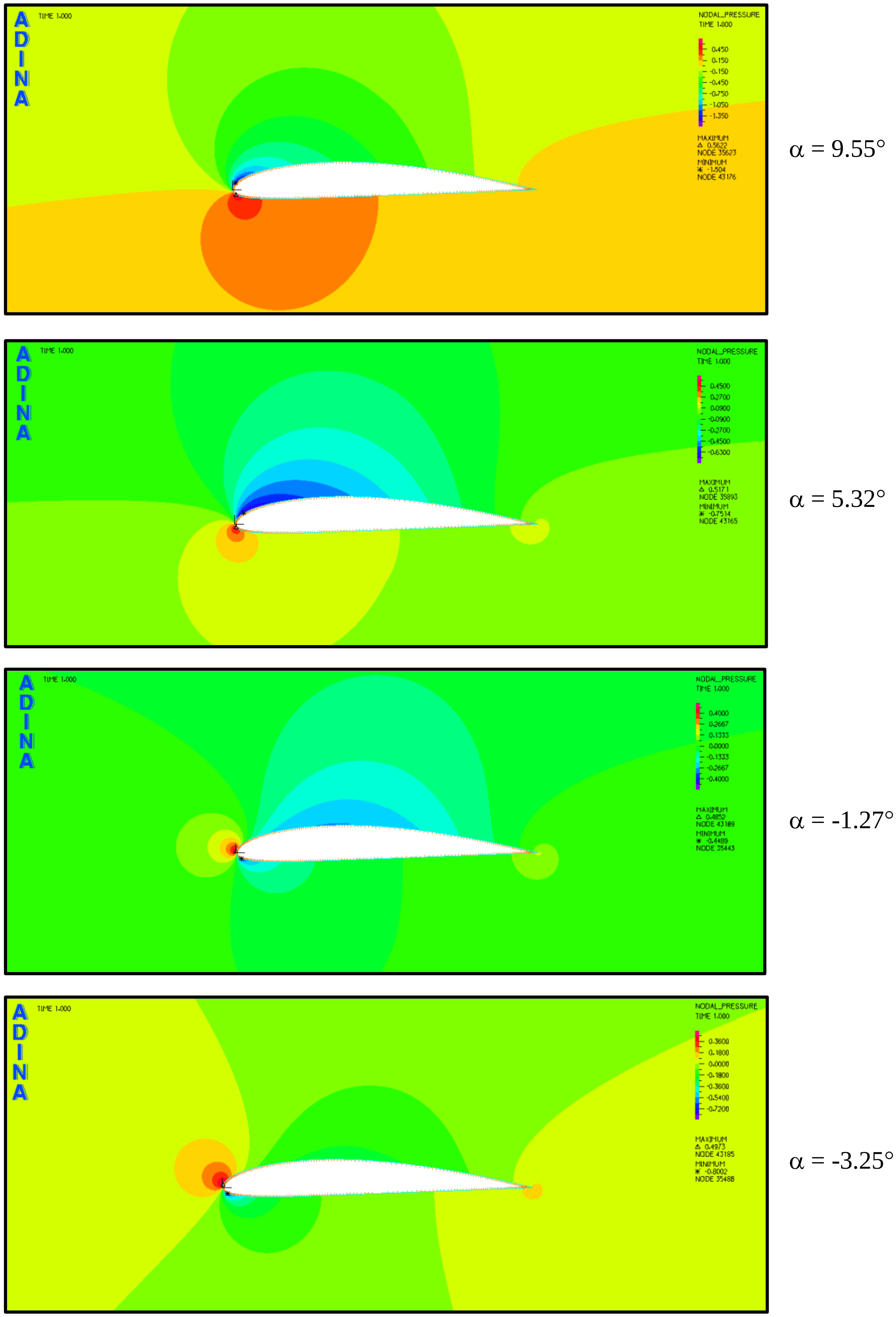

Figure 16. The pressure field for a single foil for the 4 different angles of attack.

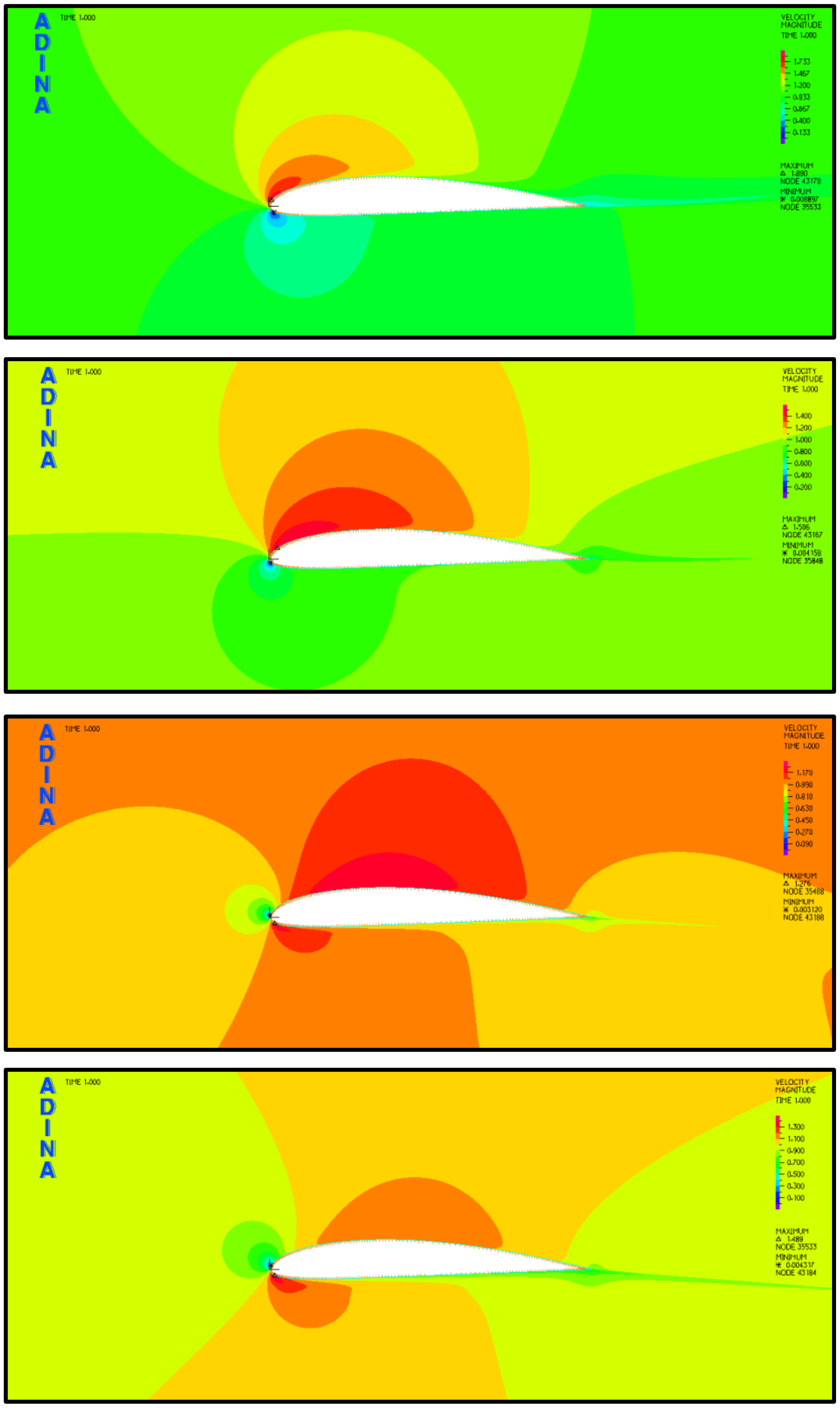

α = 9.55°

α = 5.32°

α = -1.27°

α = -3.25°

Figure 17. The velocity field for a single foil for the 4 different angles of attack.

The following figures compare between the analytical solution, experimental and the CFD results. Each figure shows the pressure distribution along the upper and lower surface of the foil. The graphs are all dimensionless where the y-coordinate is the dimensionless pressure (C_P) and the x-coordinate is the chord length in %.

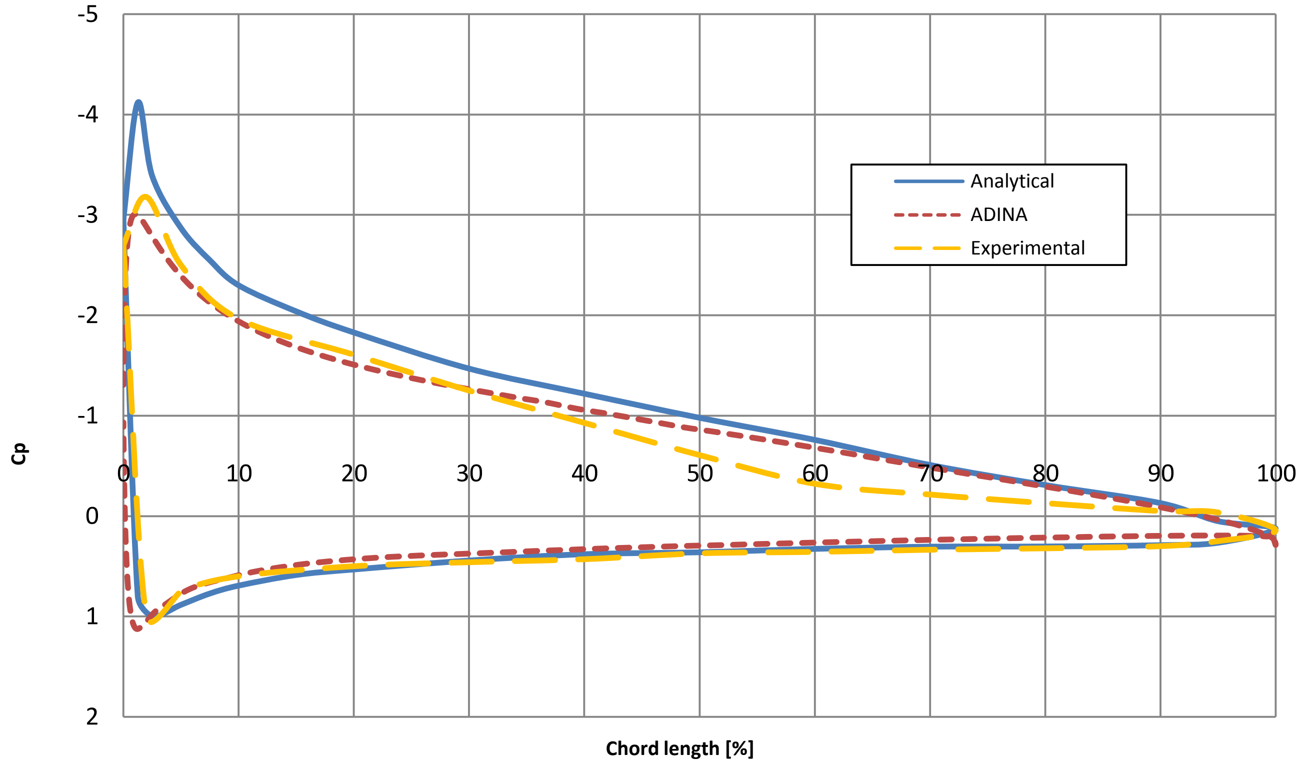

Figure 18. Comparison of pressure distribution for a single foil at α= 9.55°.

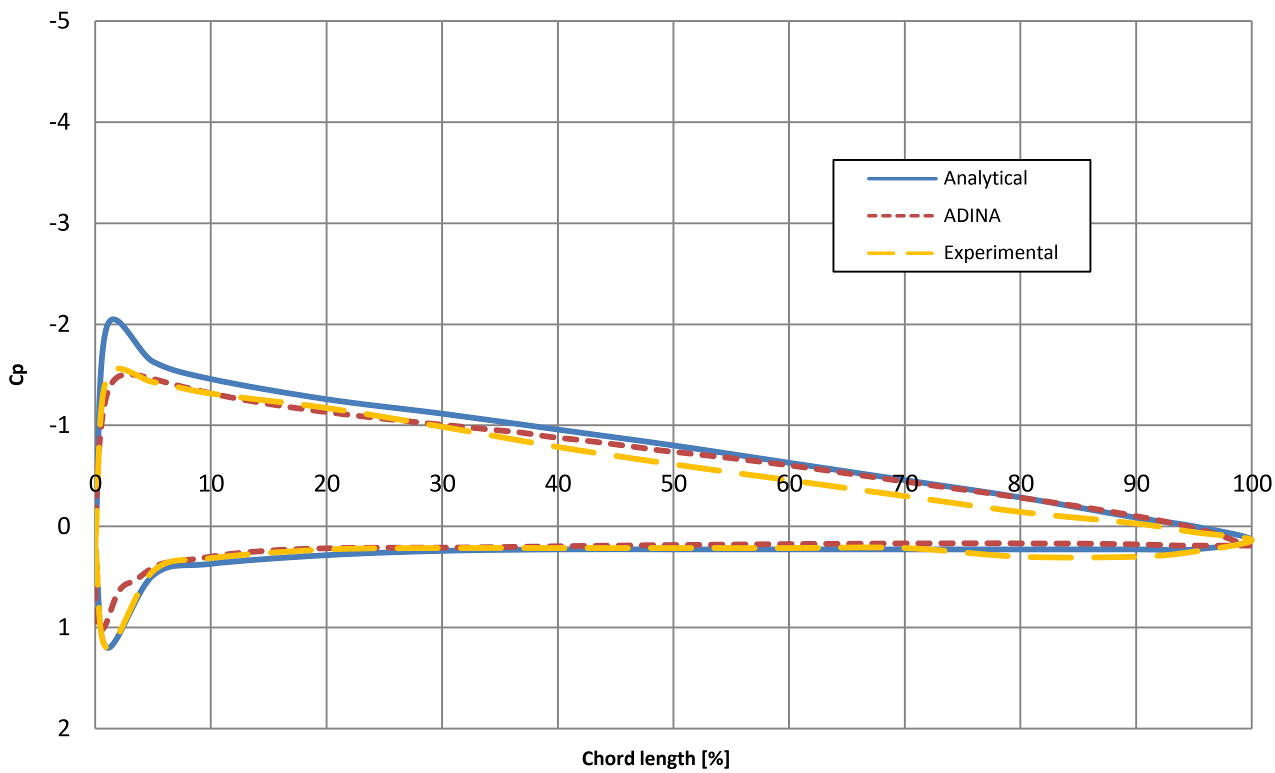

Figure 19. Comparison of pressure distribution for a single foil at α= 5.32°.

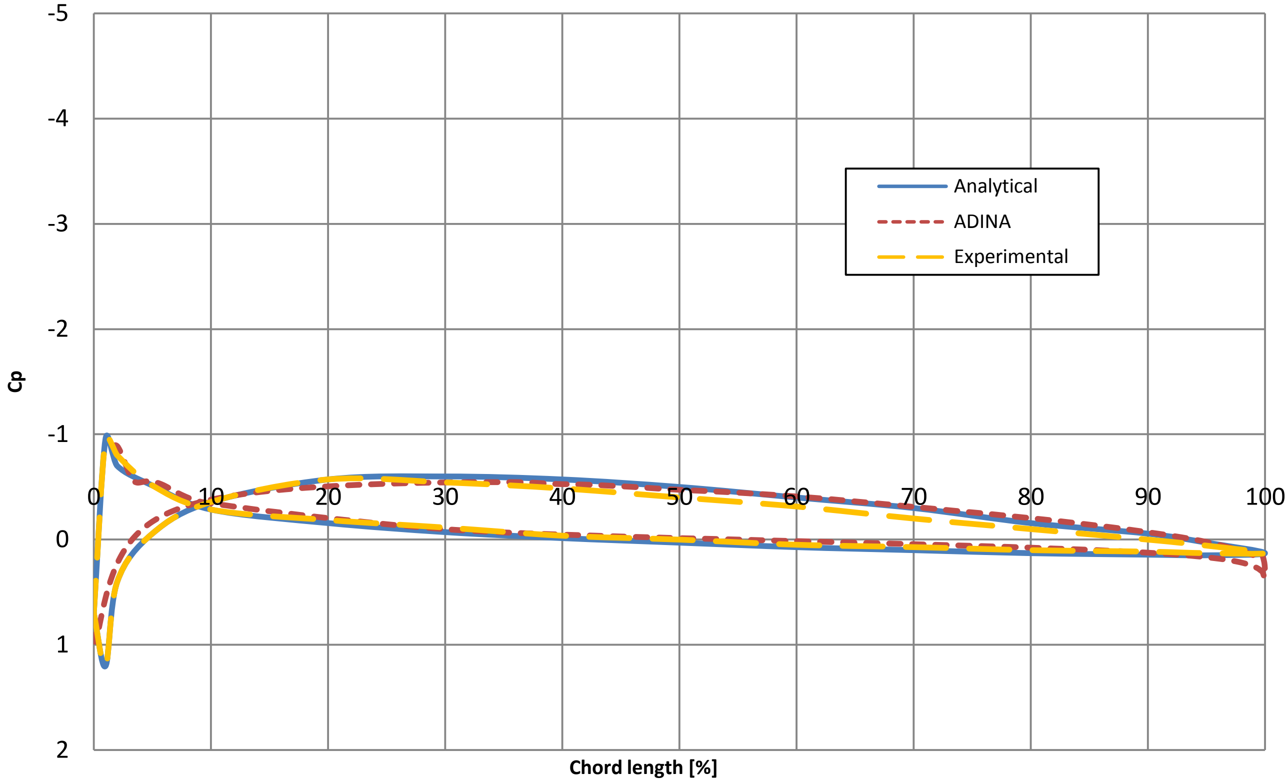

Figure 20. Comparison of pressure distribution for a single foil at α= -1.27°.

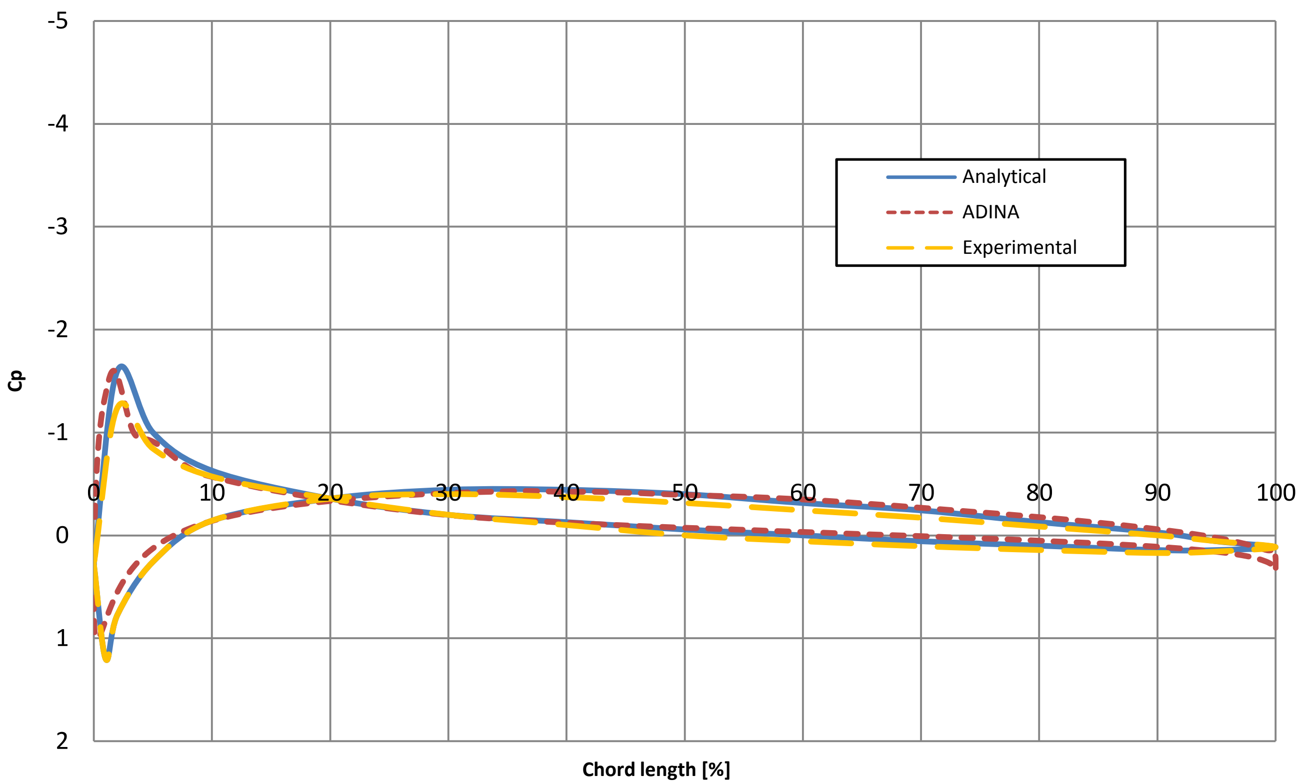

Figure 21. Comparison of pressure distribution for a single foil at α= -3.25°.

Integrating the pressure distribution curve along the foil produces the lift coefficient; second integration of the pressure curve with respect to the middle of chord produces the moment coefficient. The following figure describes the lift and moment coefficients obtained by integrating the above results versus the theoretical values:

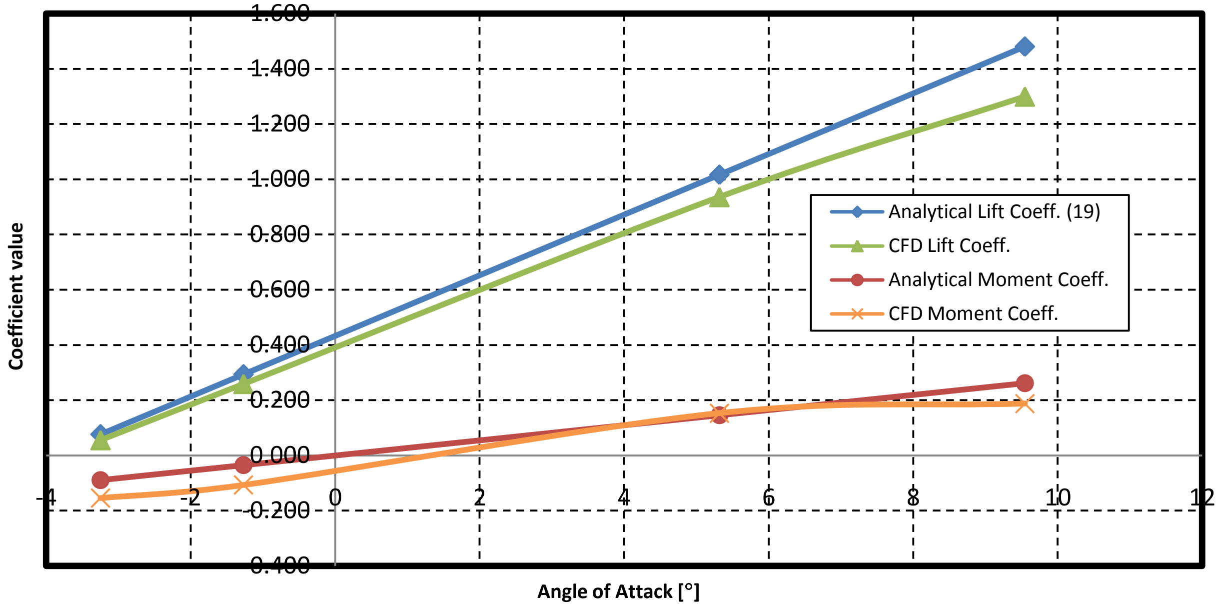

Figure 22. Lift and Moment coefficients for a single foil - CFD vs. Analytical results.

According to the graph, the lift coefficient behaves the same between the analytical solution and the CFD solution. However, the moment coefficient of the CFD solution with respect to the center of the chord is not linear like the analytical one since the analytical solution is based on approximating the foil as a parabolic curve with the maximum camber at its center. This approximation is good for small angle of attack only and the behavior of the curve is linear. However, the actual geometry of the foil section is not parabolic and that explains the differences in values and behavior of the moment coefficient.

One of the main important advantages of CFD software is the ability to plot the stream lines around the foil without much of an effort. Before the CFD became a proven tool, one would have gone through complicated experiments with colored inks and sophisticated equipment like adequate cameras and measurement devices in order to accomplish the streamline view around the foil. According to [16], few steps are needed to plot the stream lines. The following figures describe the stream lines around the foil for each of the 4 angles of attack analyzed above:

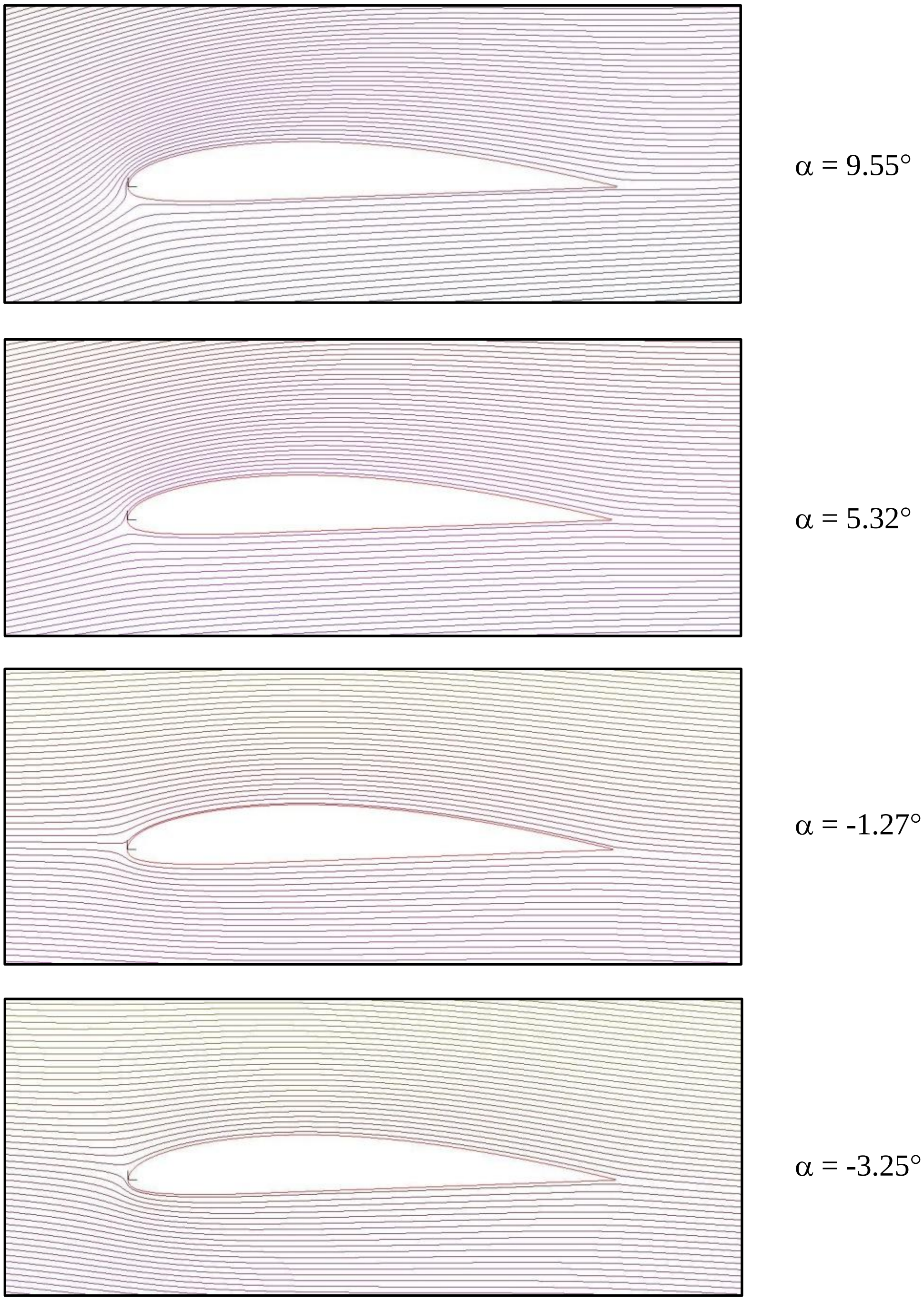

Figure 23. Stream lines around the single foil for the 4 angles of attack.

It is interesting to see that although the angle of attack of the flow is given in the CFD model, the streamlines very close to the foil do not follow this angle due to the presence of the foil. For example, looking at the streamlines at $\alpha = 9.55°$, one can easily see that the streamline which get to the leading edge has a bigger angle approximated as 30°.

4.5 Discussion of the Results

Looking into the results one can easily see that the analytical, experimental and CFD pressure distribution curves are almost the same for each one of the four angles of attack. Integrating those curves into lift and moment coefficients, a very good accuracy and similarity is obtained between the curves. However, there are slight differences between the curves and they do not match in every point along the foil. Several reasons can cause to those differences such as:

1. The analytical solution is based on the basic assumptions which are only close to reality but not exact.
2. The analytical solution solves the mathematical model and not the physical model.
3. The foil in the experiments was not smooth enough but had some humps along it.
4. The measurements of the experiments were not exact and also adjusting the angle of attack of the foil was only accurate up to one decimal place.
5. The viscosity of the fluid is not zero and there are boundary layer effects that needed to be taken into account.
6. Small separations of the flow might have taken place right after the leading edge which made the physical flow vary from the solved model.

In addition to successfully comparing the results and getting high accuracy of the model, a great advantage of the CFD was used - the ability to plot the streamlines around the foil for different angles of attack in seconds without any effort. One can learn a lot from those streamlines, for example how big the pressure is at the leading edge, the size of the stagnation zone at the leading edge, how the flow leaves the tail and whether the Kutta condition is satisfied, whether there are any jumps of the flow or the stream lines are smooth and fair.

In summary, one can see that the accuracy of the results is very high and definitely satisfactory.

4.6 Optimal Mesh Study & Validating the CFD solution (Bands)

One of the main aspects of the CFD software is the mesh density. On the one hand, the user wants to get the most accurate results he can get while on the other hand the system is limited by the memory usage and the CPU ability of the computer he uses. In addition, one of the main goals of a CFD model is to get accurate enough results in minimum time. Combining those parameters together to the effective solution where a precise enough model is run using adequate resources in a reasonable time led to the search for the optimal mesh of the domain. Some zones of the model require a refined mesh i.e. leading and trailing edges, while other parts of the domain can be meshed using coarse divisions along the lines and in the areas.

In order to verify the results of the CFD model, one should compare the results to experiments, as was done and described in the previous sections. Since such experiments did not always exist nor it is easy to perform and conduct such experiments when required, another tool is needed to validate the CFD process and the obtained results. Such a tool is given in [16] and it is called the repeating bands. After solving the CFD model, one can easily plot the error of the solution (like pressure and vorticity) in the nodes of adjacent elements. Since the solution within the element is continuous but still the overall solution is numeric, there are different values at the nodes of the model. Thus, plotting the error at those nodes can help the user to know where a refined mesh is needed. Where there are high jumps, there will be mixed colors (symbolizing the errors) at the problematic zones while clear zones under the same color represent a good and sufficient refined mesh. Those zones are called the repeated bands.

Considering our CFD model, different meshes were used on the model and the pressure distribution curves were compared with the experimental results. The following figure illustrates those curves for the 9.55° angle of attack:

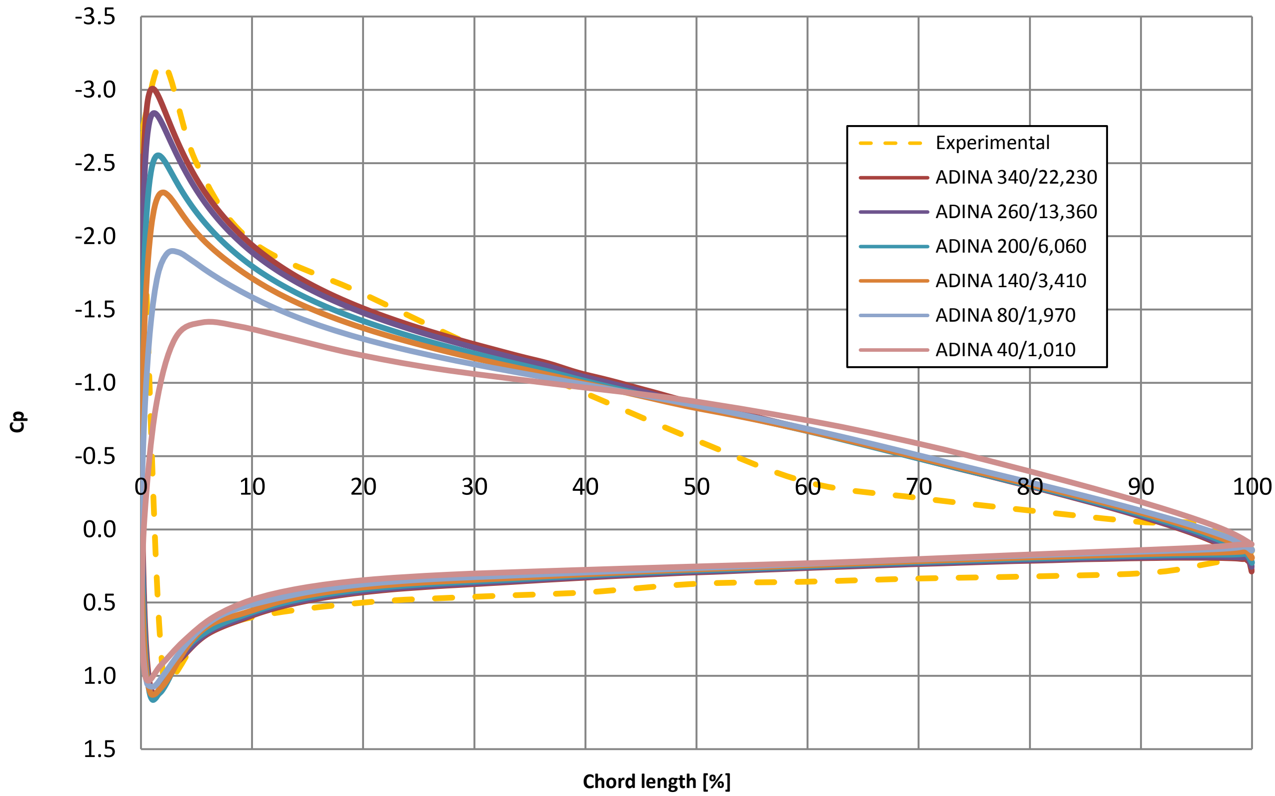

Figure 24. Pressure curves along the single foil domain at 9.55° with different meshes.

Two numbers are given for each of the curves where the format is xx/yy. The first number (xx) represents the number of elements along the foil and the second number (yy) represents the total number of elements of the entire domain. It is easy to see that for coarse meshes one gets poor results. On the other hand, when refining the model with sufficient number of elements, very good results are obtained which are very close to the experimental results. Only the two closest CFD curves are satisfactory enough (22,230 and 13,360 elements) while the other 4 meshes are far from being a good model. In addition, one should pay attention to the fact that there is a big jump in the number of elements between the 2 satisfying curves while there is not much of a difference between them. This fact shows that in order to get a very high and accurate model, a very refined mesh is needed which requires high resources of memory usage and CPU performance. However, as mentioned above, the user must realize that sometimes there is no need to go so far and using the second curve (13,360) is good and sufficient enough.

In addition, assuming there are no experimental results and avoiding the yellow dashed curve, the repeated bands are being used as a tool of determining the appropriate mesh one should use in this model. The following figures describe the repeated bands for each of the 6 meshes above. The left side of each figure describes the repeating bands around the foil and the right side is zooming in on the leading edge. In addition, the mesh appears in each figure.

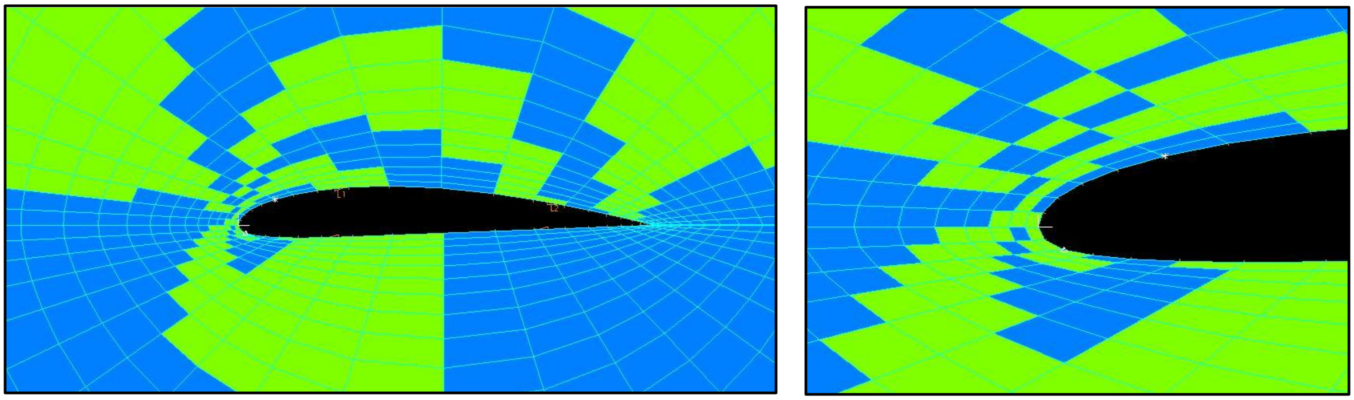

Figure 25. Repeated bands for the 40/1,010 mesh at 9.55° angle of attack.

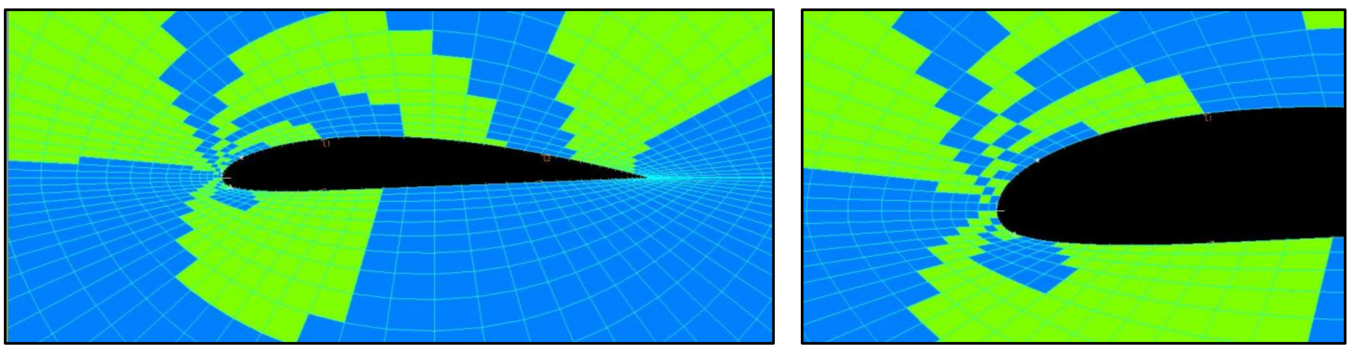

Figure 26. Repeated bands for the 80/1,970 mesh at 9.55° angle of attack.

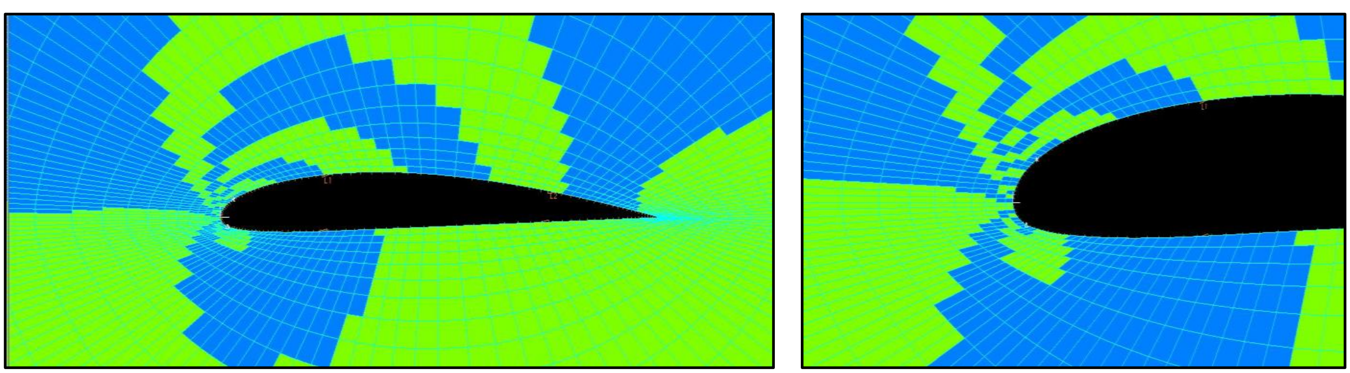

Figure 27. Repeated bands for the 140/3,410 mesh at 9.55° angle of attack.

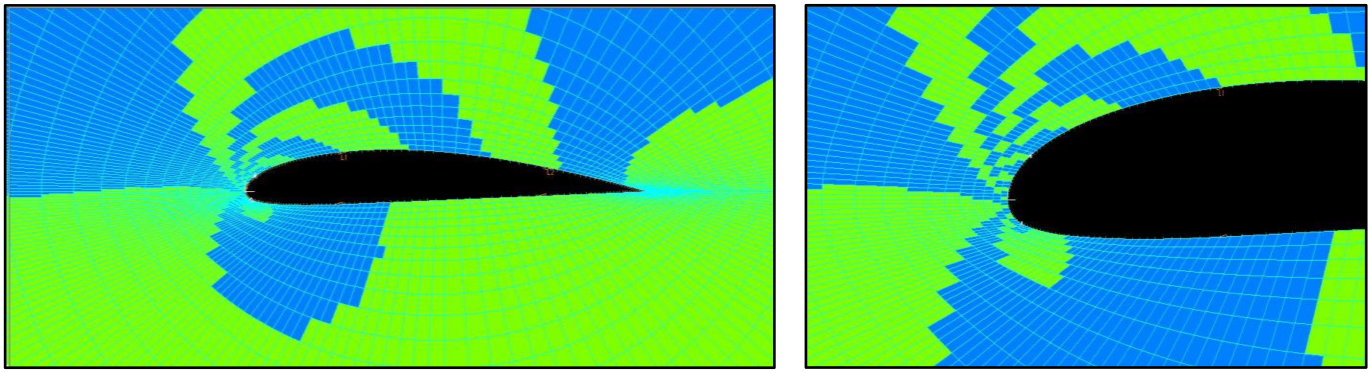

Figure 28. Repeated bands for the 200/6,060 mesh at 9.55° angle of attack.

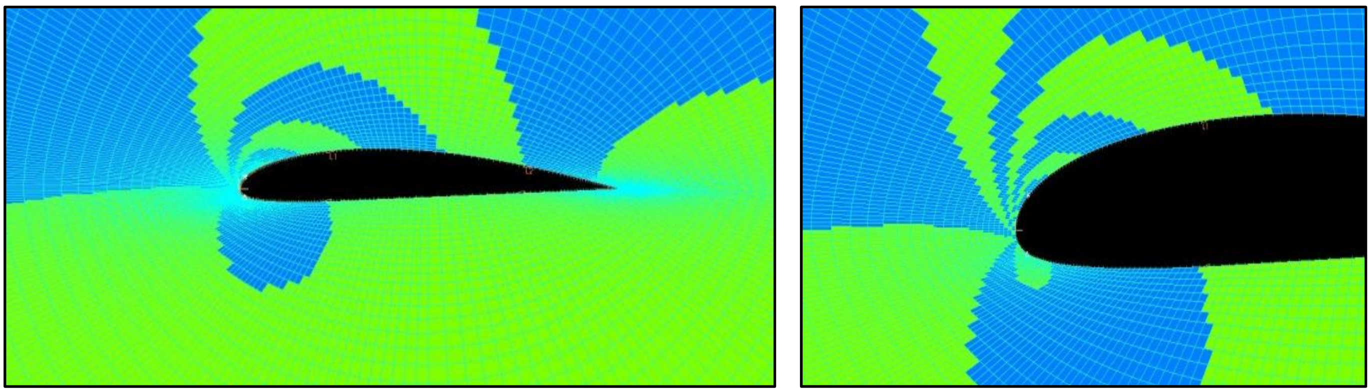

Figure 29. Repeated bands for the 260/13,360 mesh at 9.55° angle of attack.

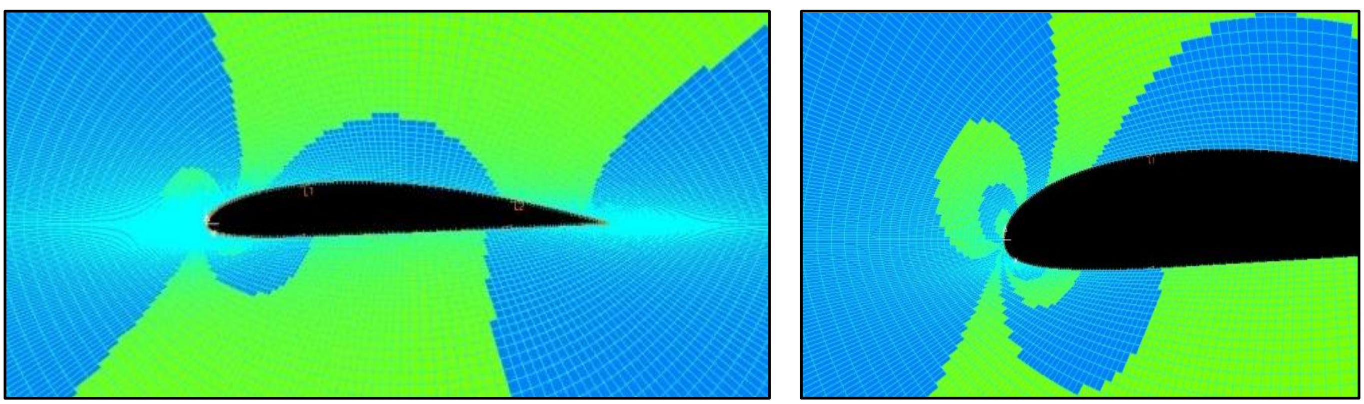

Figure 30. Repeated bands for the 340/22,230 mesh at 9.55° angle of attack.

One can see that for the last 2 meshes the repeated bands are clear zones which point out the fact that the model is converged and the error between the nodes is small at those two meshes. Comparing with the experimental results, it can be seen that the last 2 meshes are much closer to those results as also shown by the repeated bands.

However, another issue is arising when exploring the optimal mesh. While the leading edge requires a refined mesh, there are some zones in the domain where a coarse mesh can be implemented such as the back part of the flow when passing the foil. Consequently, two other meshes were examined in order to optimize the model where accurate results can be obtained with fewer elements in the model.

The first mesh indicated as 170/4,130-10% is obtained by cutting the model after the first 10% of its chord length and refining that zone while using a coarse mesh along the rest of the foil. The second mesh indicated as 190/9,600-50% is obtained by cutting the model in its center and using a refined mesh at the first 50% and a coarse mesh at the last 50%. The following figure describes plotting the distributed pressure curve of each of those meshes (blue and green dashed curves respectively) with the other meshes examined above:

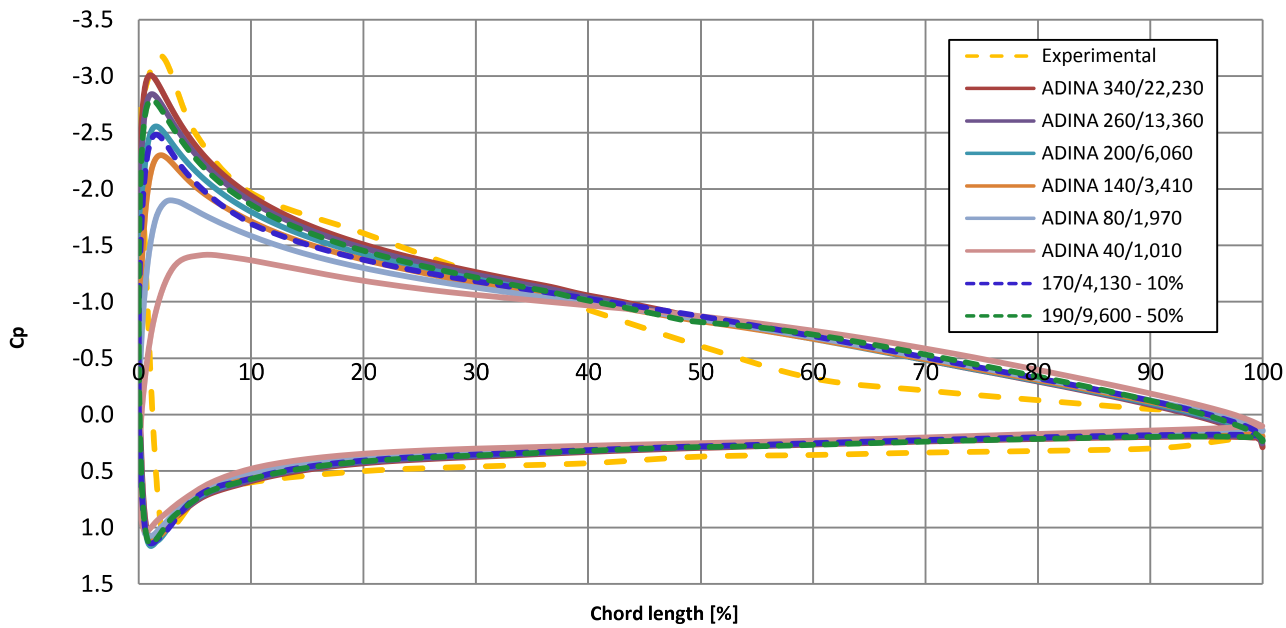

Figure 31. Pressure curves along the single foil domain at 9.55° with 2 additional meshes.

It can be seen that the second mesh gives satisfying results while it has only 9,600 elements in the entire model. This kind of mesh can be considered as the optimal mesh for the CFD model discussed above. Using the repeated bands tool as another comparison and validation of this conclusion one would find the following: The repeated bands are nice and clear at the second mesh while there is disarray at the first one.

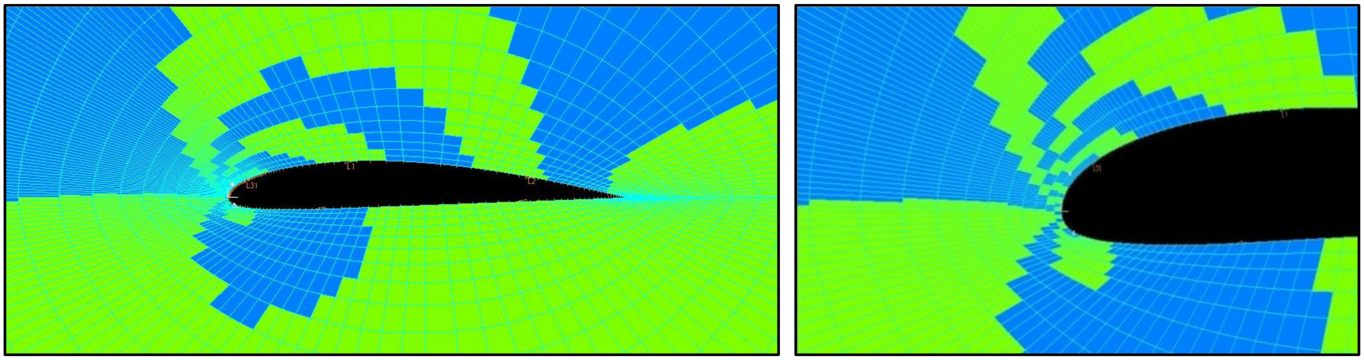

Figure 32. Repeated bands for the 170/4,130-10% mesh at 9.55° angle of attack.

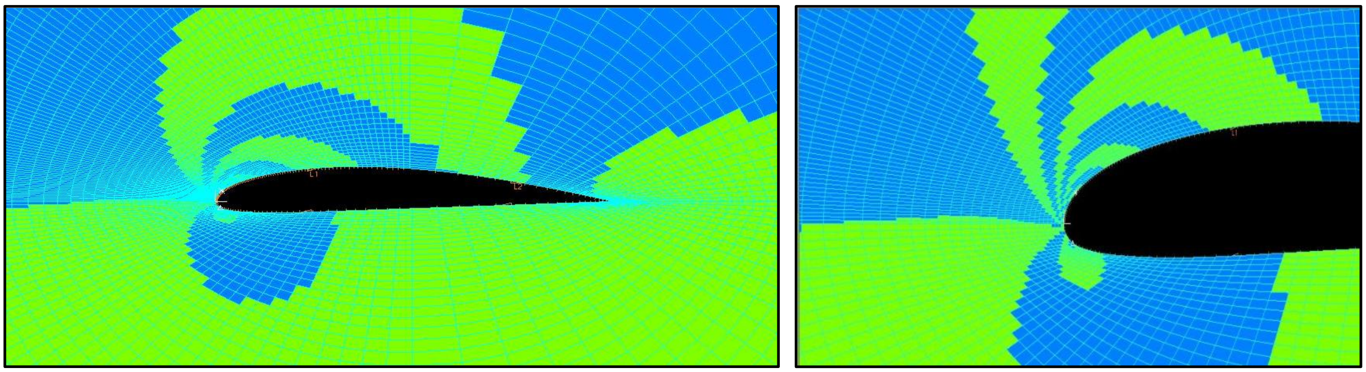

Figure 33. Repeated bands for the 190/9,600-50% mesh at 9.55° angle of attack.

The following figure describes taking all the above 8 different meshes and calculating the lift and moment (with respect to the origin) coefficients:

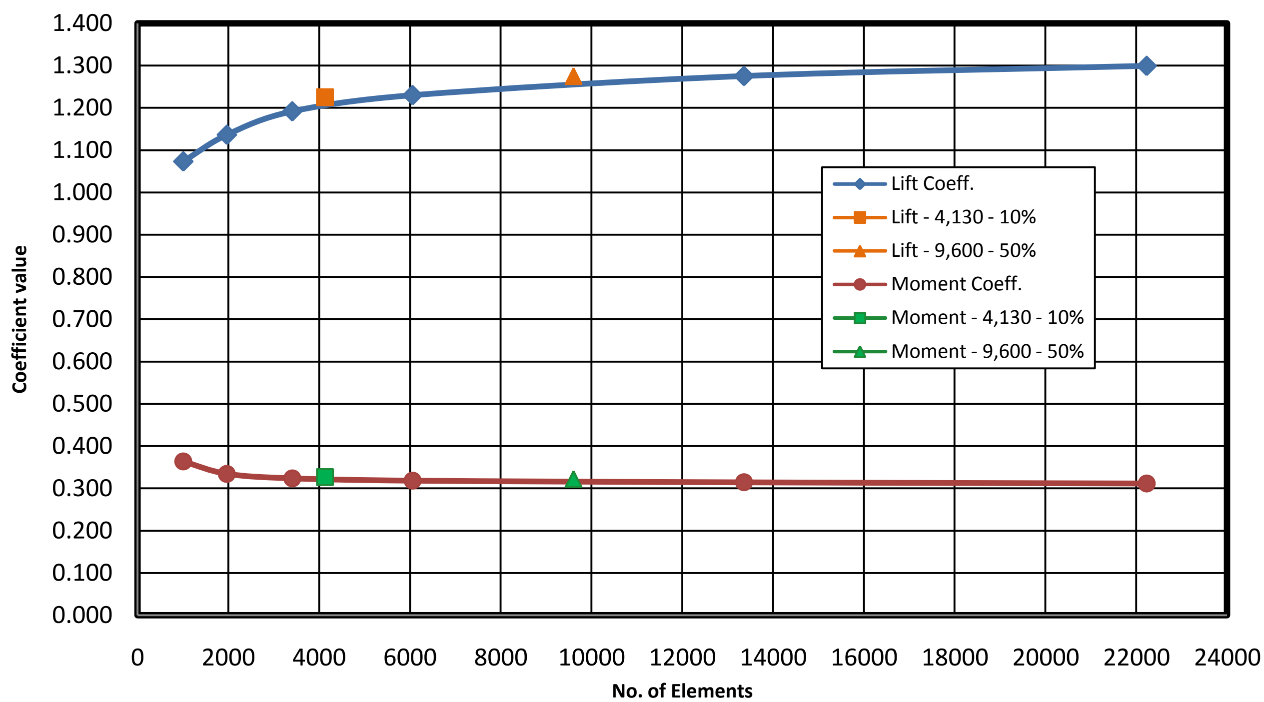

Figure 34. Lift and Moment coefficients of different meshes at 9.55°.

According to this figure, the second mesh (190/9,600-50%) gets the same results as the 260/13,360 mesh while is saves 3,760 elements which is a 28% reduction. This is very meaningful evidence. In order to solve a CFD model in a beneficial and effective way, the user must have an idea of the physical problem and to make a smart mesh. Otherwise, he might use a vey refined mesh where his system cannot support the computations being performed by the finite elements software or the calculation will last for too long.

4.7 NO Slip Condition

One of the main assumptions of the mathematical model solved by the finite elements method was that there is a FREE slip along the foil as part of the boundary conditions. Actually, in the physical model, there is a NO slip condition along the foil because of the viscosity of the fluid. That viscosity causes a boundary layer along the foil where the Navier-Stokes equations apply. Only outside this boundary layer the flow acts as potential one. Due to that phenomenon, there is separation of flow and it is not potential at all. However, for many naval engineering purposes where sea water is the fluid, its viscosity effects can be neglected.

In order to examine this assumption in the CFD model, few runs were made with NO slip condition along the foil for 2 angles of attack. It is noted that for a potential flow where there is no separation of the flow, same results are obtained for different *Re* numbers. The potential flow is independent in *Re* number. When the NO slip condition is applied, the flow becomes dependent on *Re* number and two regimes are considered, the laminar regime and the turbulent regime. For the turbulent regime, many variable-based parameters should be used in CFD model (such as turbulence-k, turbulence-ε, etc.). Those parameters are of vital importance and they influence the flow in many ways. This field is not part of this research and it may be considered as future research. Thus, the NO slip condition was examined in the laminar regime for 2 of the 4 angles of attack discussed above: -1.27° and -3.25°. The following two figures describe the pressure distribution along the foil with comparison to the experimental results and the FREE slip condition results of the CFD model.

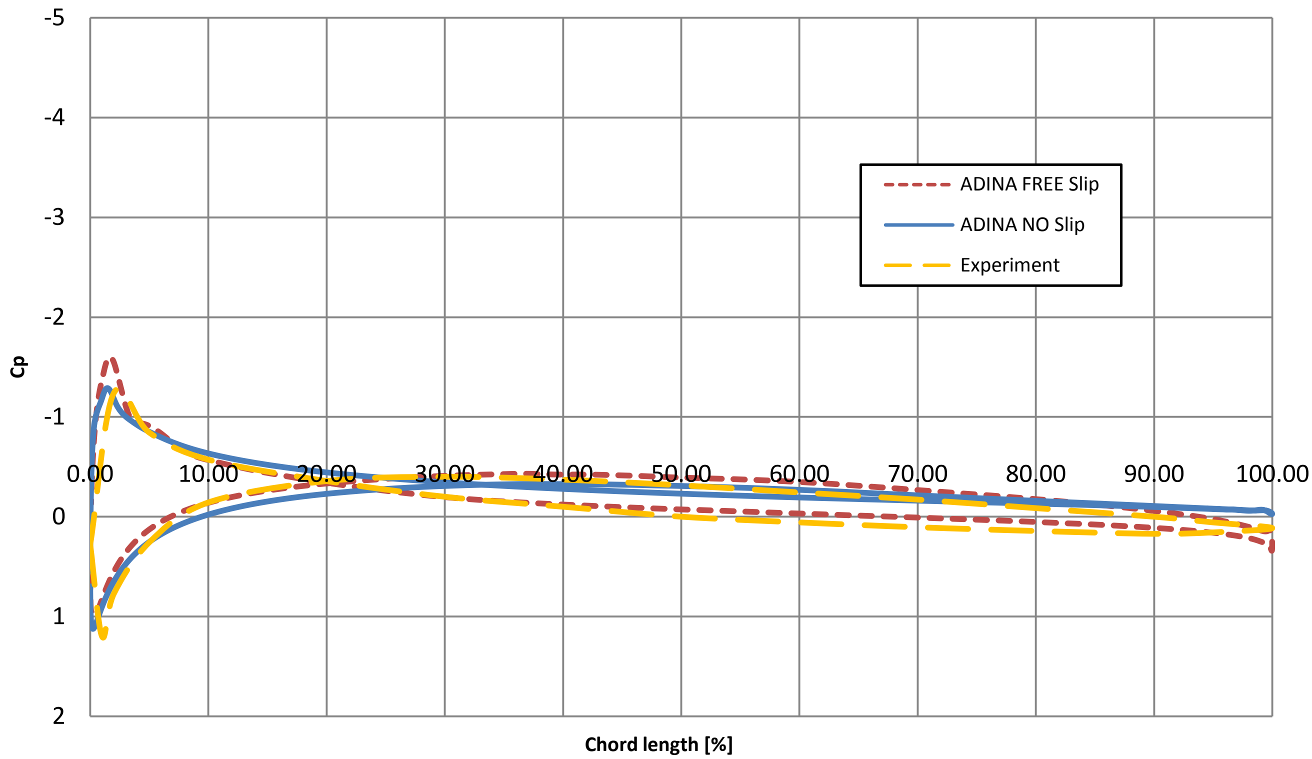

Figure 35. pressure distribution curve with NO Slip condition at -3.25°.

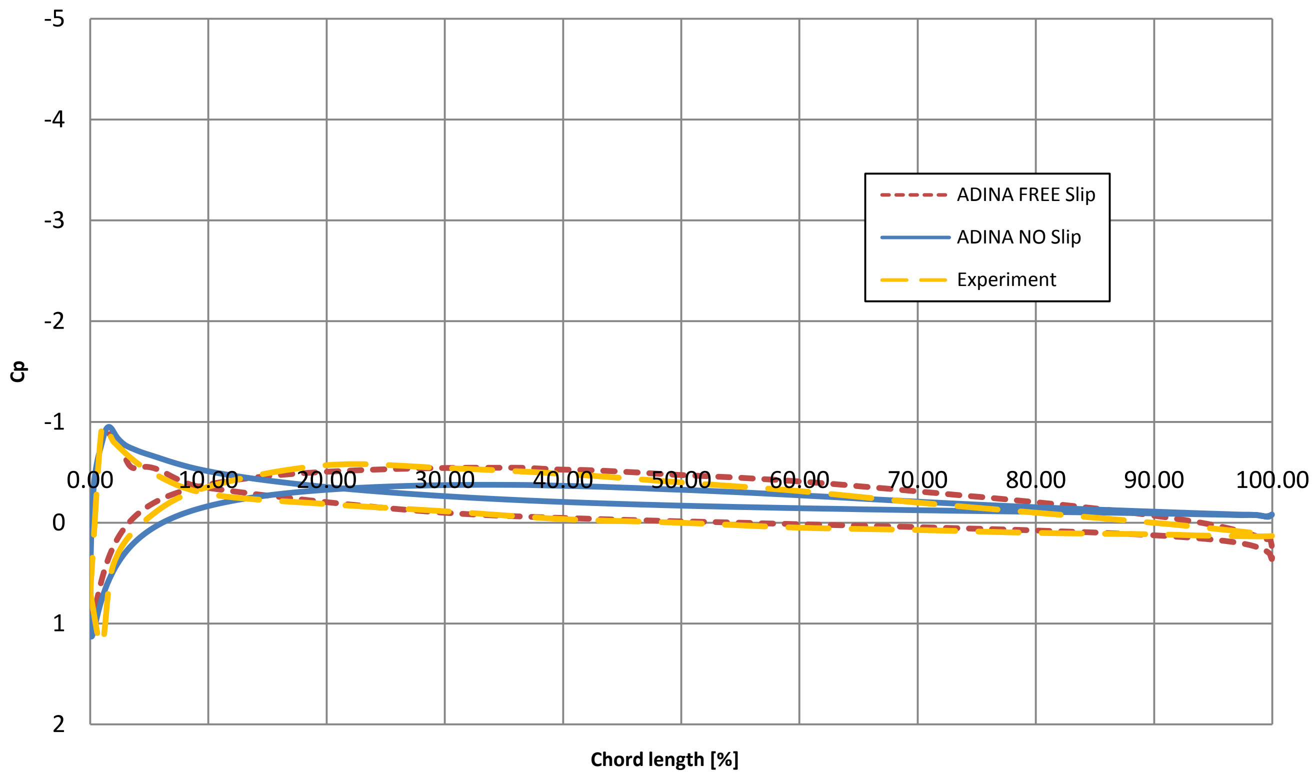

Figure 36. pressure distribution curve with NO Slip condition at -1.27°.

Apparently, the NO slip condition, which represents the real life case, should give closer results to the experimental results. However, looking carefully into the graphs, it turns out that the NO slip condition curve is quite different from the experimental curve. On top of that, the FREE slip which represents a potential flow is much closer and almost the same as the experimental curve. In order to understand this finding, it is a necessity to get deeply into what really happens in physics and in the CFD model.

When the flow is in the laminar regime, the boundary layer is growing up as we move away from the leading edge. As a matter of fact, for a foil in very small angle of attack separation almost does not occur and the flow can be considered as potential, but when increasing the angle of attack a little bit, separation takes place right away. The following 3 figures taken from [17] describe the stream lines around a foil in the laminar regime. The first figure shows the flow for a symmetrical foil in zero angle of attack and the 2 other figures show the separation when a small angle of attack is applied.

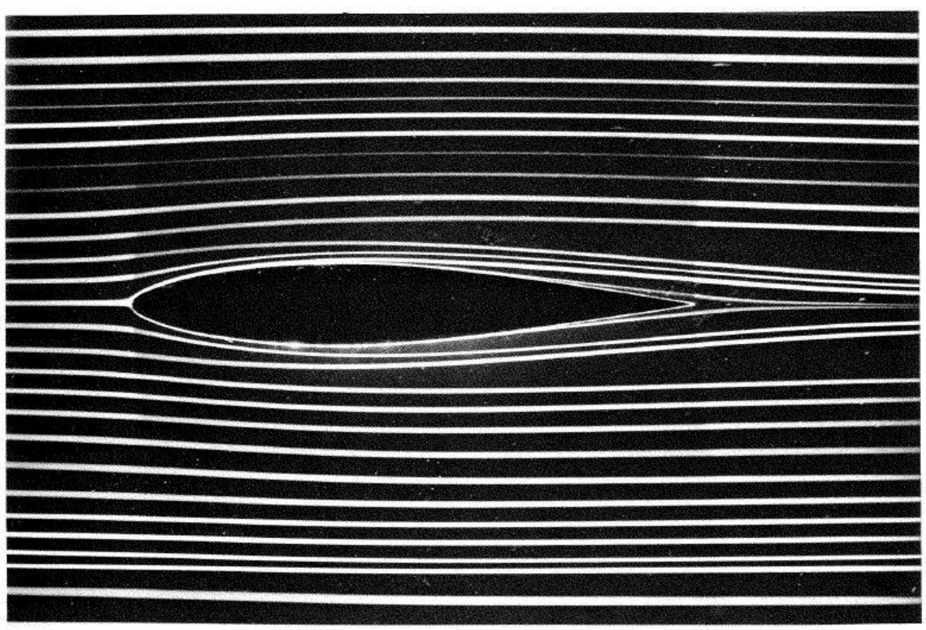

23. Symmetric plane flow past an airfoil. An NACA 64A015 profile is at zero incidence in a water tunnel. The Reynolds number is 7000 based on the chordlength. Streamlines are shown by colored fluid introduced upstream. The flow is evidently laminar and appears to be unseparated, though one might anticipate a small separated region near the trailing edge. *ONERA photograph, Werlé 1974*

Figure 37. Stream lines around a foil in the laminar regime at 0°.

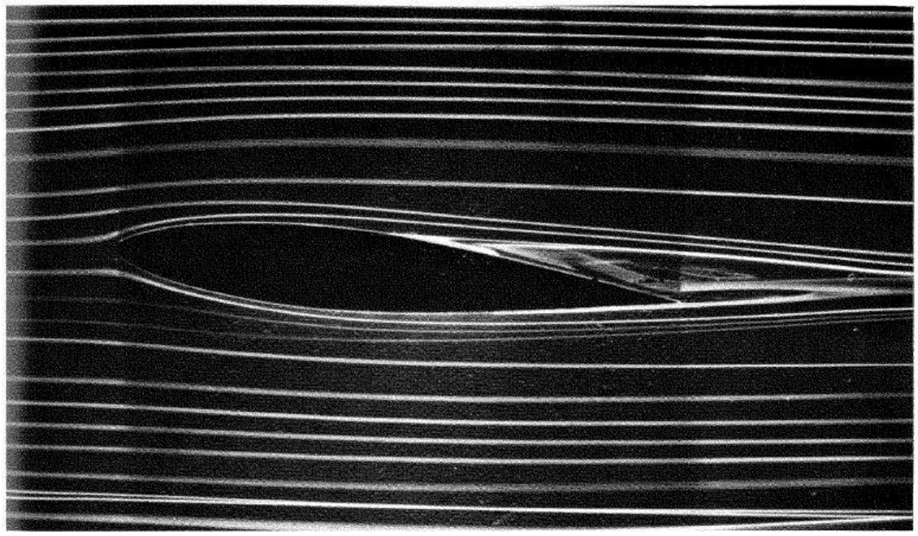

34. Boundary-layer separation on an inclined airfoil. When the NACA 64A015 airfoil of figure 23 is raised to 5° incidence the laminar boundary layer separates from the rear half of the upper surface. The flow remains attached to the lower surface, from which it leaves tangentially at the trailing edge. Streamlines are shown by colored fluid filaments in water. *ONERA photograph, Werlé 1974*

Figure 38. Stream lines around a foil in the laminar regime at 5°.

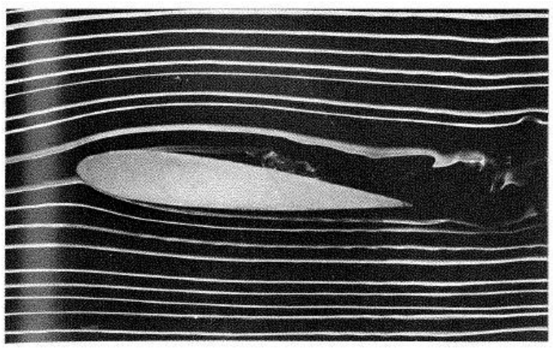

72. Symmetrical airfoil at angle of attack. Smoke in a wind tunnel shows separation over the upper surface of a profile that is 15 per cent thick at 6° incidence and a Reynolds number of 20,000. *Photograph by Peter Bradshaw*

Figure 39. Stream lines around a foil in the laminar regime at 6°.

According to these figures, separation occurs very early in the laminar regime when small angles of attack are applied. In addition, since the flow separates and according to the Kutta condition as explained above, the pressure at the tail is very low and pressure is not being built along the foil. Thus the pressure distribution curve is very low and narrow since no lift is produced. Taking that into consideration and having better understanding of the flow field, it is easier to look back at the pressure distribution curves of the CFD model when NO slip condition is applied. The blue curve which represents the pressure along the foil is narrow and the area under this curve is small, i.e. no lift is gained from a foil in the laminar regime. Therefore, the No slip curve makes sense and actually does follow with reality.

However, that conclusion leads to another question; how come the FREE slip condition which represents potential flow gives such a pressure distribution curve which matches the experimental curve so well? We saw that it is not beneficial to use a foil in the laminar regime since no lift is produced. Every airplane or hydrofoil is functioning in the turbulent regime only. Thus, the inquiry becomes how the FREE slip condition fits the turbulent flow. That inquiry can be understood by going back to the assumptions of the mathematical model.

In the turbulent regime, the flow detaches from the foil when separation occurs. However, when small angles of attack are applied, the flow is incompressible and the viscosity of the fluid is very small that can be neglected - the boundary layer is very thin and although the flow detaches, it reattaches back to the foil due to the high velocity field. Since the fluid we deal with is sea water, the flow is incompressible and the viscosity can be neglected. Consequently, when keeping on small angles of attack, the flow remains attached to the foil in the turbulent regime and this is why it can be considered as potential flow since separation does not take place. The potential flow is nothing else but applying the FREE slip condition on the foil as the right boundary condition under those assumptions.

Chapter 5 - Stretching the foil

5.1 The Geometry of the Model

After using the CFD module in ADINA (called ADINA-F) to examine the single foil under 4 angles of attack and successfully comparing it with analytical and experimental results, the stage of stretching the geometry of foil has taken place. This stage has a very important consequence which is to show how easy and fast it is to change the geometry of the foil and to optimize it until the desired design for lift is achieved, that is instead of going through massive experiments again or the analytical process which gives only approximation of the real results.

The stretching of the foil was along its horizontal axis only, i.e. its camber remained constant but its chord length was enlarged. Four different stretches were examined with comparison to the original geometry of the foil (the corrected geometry as detailed in the previous chapter). The foil was stretched in 25%, 50%, 75% and 100% of its chord length. The following figure shows a side view of the foil in each of the 5 cases as modeled in Unigraphics software:

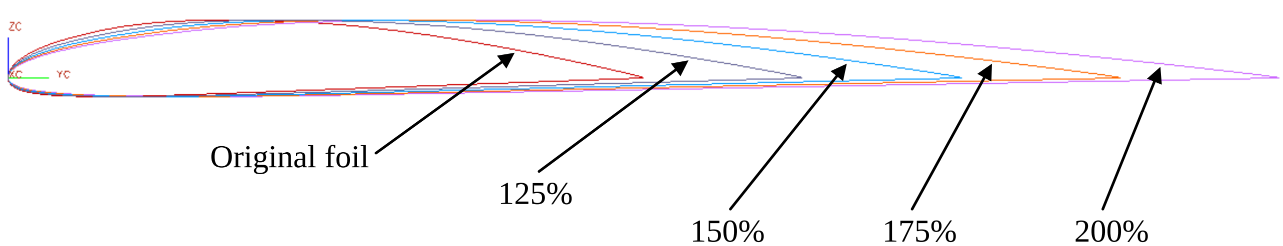

Figure 40. Side view of the stretched foil for all the 5 cases.

5.2 CFD Analysis and Results

All of those 5 cases were examined for one angle of attack only (5.32°). All the boundary conditions, fluid characters and applied loads are the same as for the single foil in the previous chapter. The following figure describes the pressure distribution along the foil for each of the stretches discussed above:

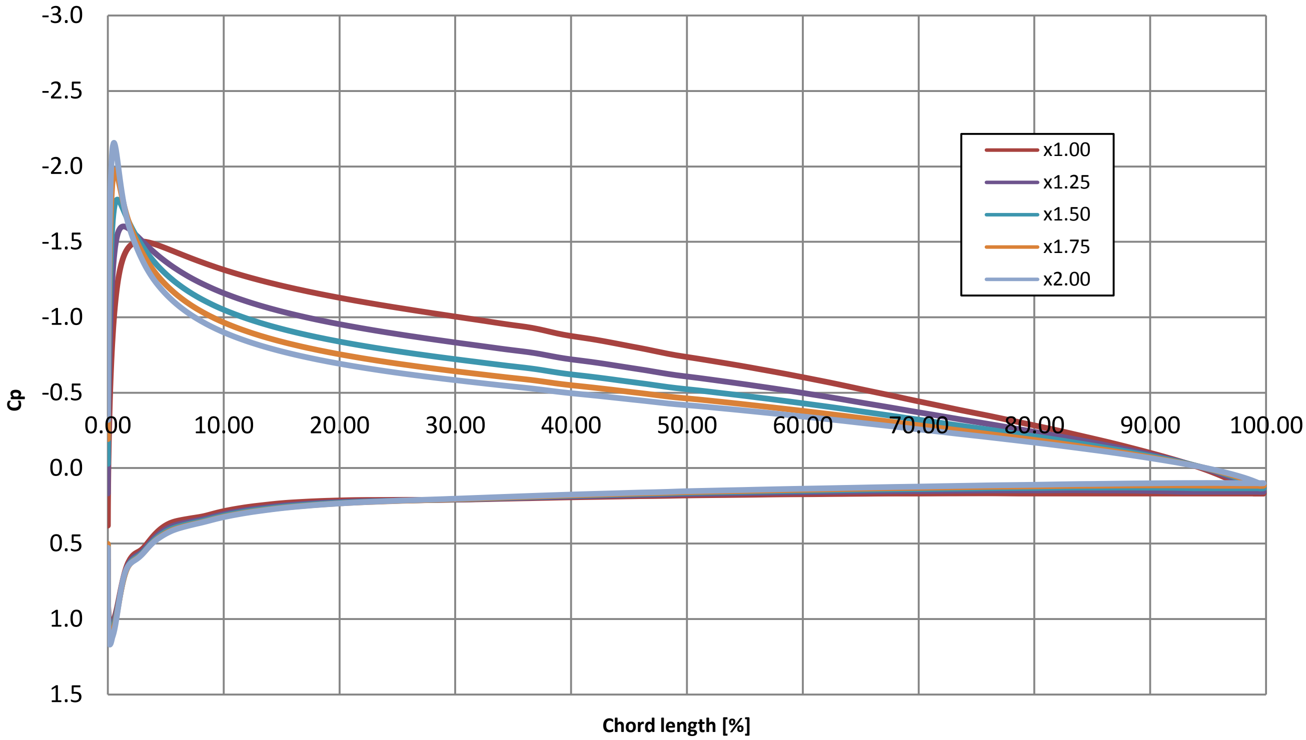

Figure 41. Pressure distribution along the stretched foil at 5.32°.

Looking at the leading edge, a very interesting finding is being observed. As the foil is stretched, a higher jump in the pressure distribution curve is obtained. This is due to the fact that the leading edge of the foil becomes sharper with its stretching and the flow is facing a sharper obstacle it needs to overcome. Another finding is that the pressure distribution along most of the foil is getting lower as the foil is being stretched. That evidence makes sense since the foil becomes flatter and the flow has less curvature in its way.

5.3 Discussion of the Results

According to equation (19), the lift of a foil is dependent on its camber (η_0) and on its chord length (l) when the angle of attack (α) is given. Thus, when keeping the camber as a constant and increasing the chord length, the lift of the foil should be reduced. The following figure shows the lift coefficient behavior and how is reduces with increasing the chord length, as expected. In addition, the moment coefficient is given as well, with respect to the origin of the foil.

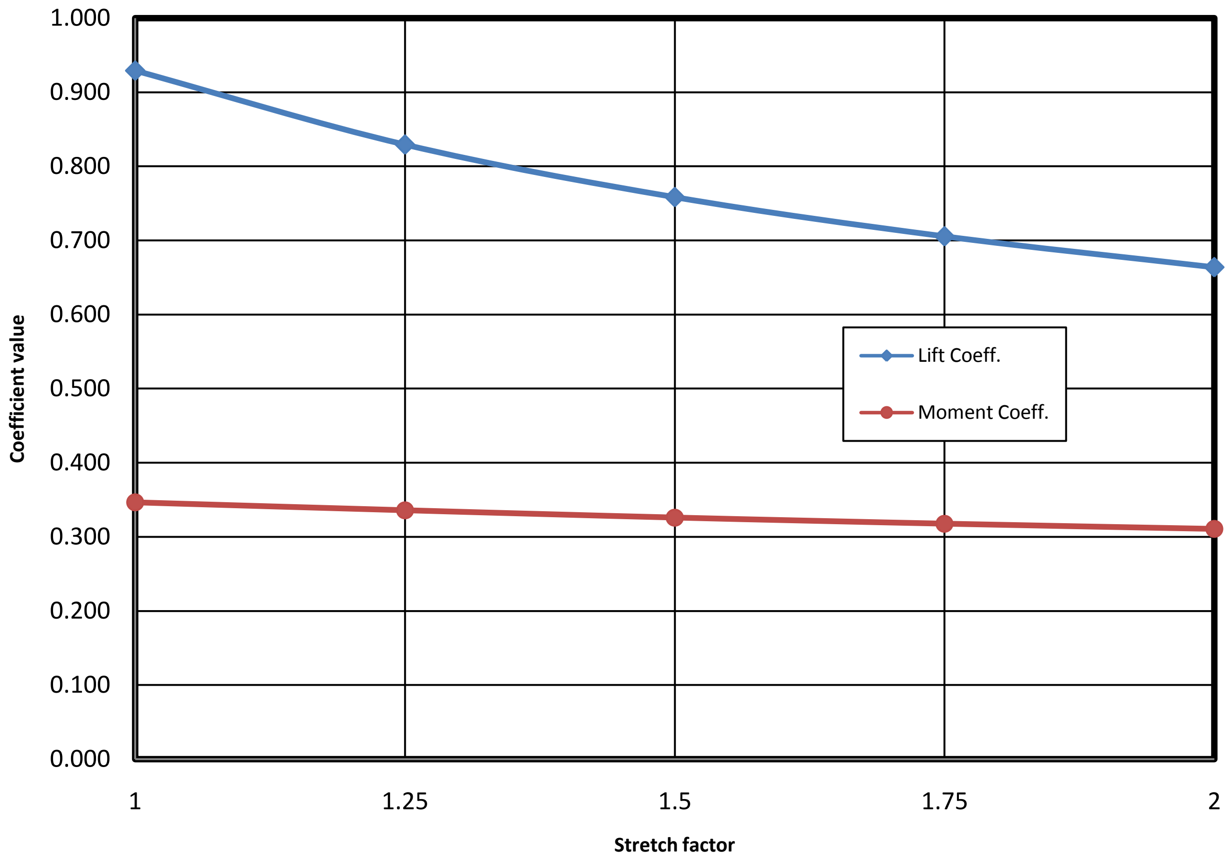

Figure 42. Lift and Moment coefficients of the stretched foil at 5.32°.

Chapter 6 - Analysis of two Vertical Foils (bi-plane)

6.1 Bi-plane Theory

Although it is sophisticated and takes much effort to calculate analytically the pressure distribution around a single foil, it is much harder when the case of two vertically displaced foils is involved. This case is known and called the bi-plane case. According to [18], such a problem is a three dimensional one and although the governing physical laws are simple, the effect on the fluid cannot be predicted accurately. However, most of the wing can be considered as two dimensional once it has a large span, that fact simplifies the calculations. In addition, the viscosity of the fluid plays a nontrivial part and only if its value is very small, its influence can be neglected at first and later be taken into account by using empirical rules. The analytical procedure described in [18] in order to find the flow characteristics assumes each foil is a straight horizontal line. Then, 4 different flows (Longitudinal flow, Vertical flow, Circulation flow and Counter-circulation flow) are applied on those two vertical lines as described in the following figure:

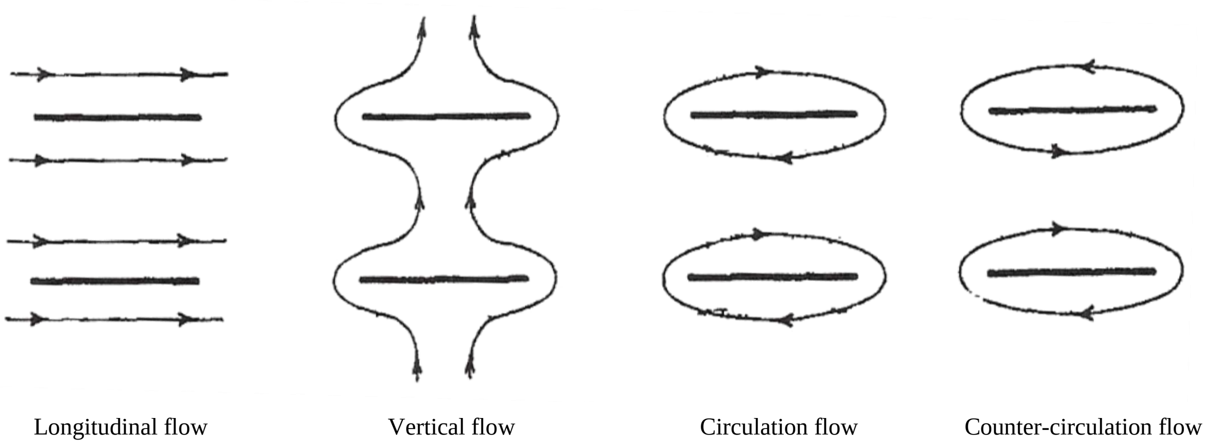

Figure 43. Different flows applied separately on a bi-plane system.

After solving for each of those 4 cases, the following stage is superposition. One should notice that the last two kinds of flow (Circulation flow and Counter-circulation flow) make the velocity at the rear edge finite and thus the Kutta condition is satisfied. The idea behind the division into 4 different flows and presenting the foil as a line is to change the edge condition in order to take the curvature of the foil into account. The same principle of converting the geometry of the single foil to a circular body is applied here as well. The two horizontal lines are transferred to two parts of the same vertical line where the upper edge of the upper line is at (0,1) and the lower edge of the lower line is at (0,-1). The following figure describes the two planes of transformation:

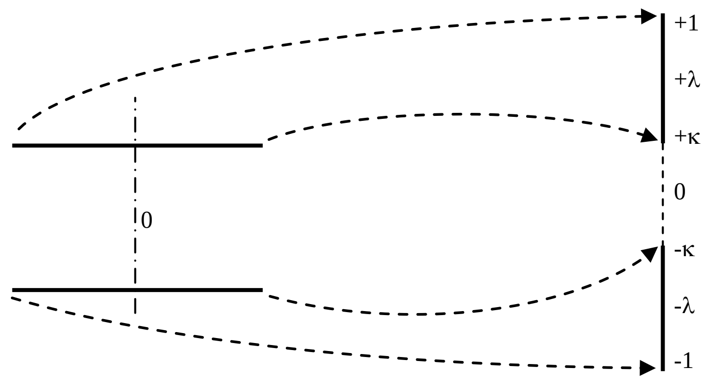

Figure 44. Transformation of a bi-plane geometry between two planes.

Consequently, the calculations become simpler and the expressions derived are friendlier. One of the important conclusions obtained by this theory is that for a bi-plane, the angle of attack is a larger contributor to gain lift than is the curvature of the foils. Reference [19] is much more detailed and also uses the theory of elliptic functions and the velocity function instead of the complex potential function. According to [19], the essence of this theory is summarized by the following important formula describing the circulation around each foil:

$$\Gamma_1 = \Gamma_2 = \frac{\pi \cdot U_\infty \cdot \sin(\alpha) \cdot \sqrt{\left(\lambda^2 - \kappa^2\right) \cdot \left(1 - \lambda^2\right)}}{\lambda} \tag{62}$$

where both λ and κ are given in the figure above. It should be noted that this formula is valid when the two foils are identical. Otherwise, the formula would carry λ_1, κ_1 and

λ_2, κ_2 corresponding to the geometry of two different foils. Using this formula, it is easy to find the lift from a bi-plane system using formula (17).

6.2 The Geometry of the Model

In order to expand the study of the bi-plane case, 7 different cellules were examined using the same Clark-Y foil. The following table and figure describe the geometry of the model. The blue foil is fixed and the green foil is the upper foil of each of the cellules:

Table 4. Bi-planes cellules that were examined.

case	G
1	25%
2	50%
3	75%
4	100%
5	150%
6	200%
7	300%

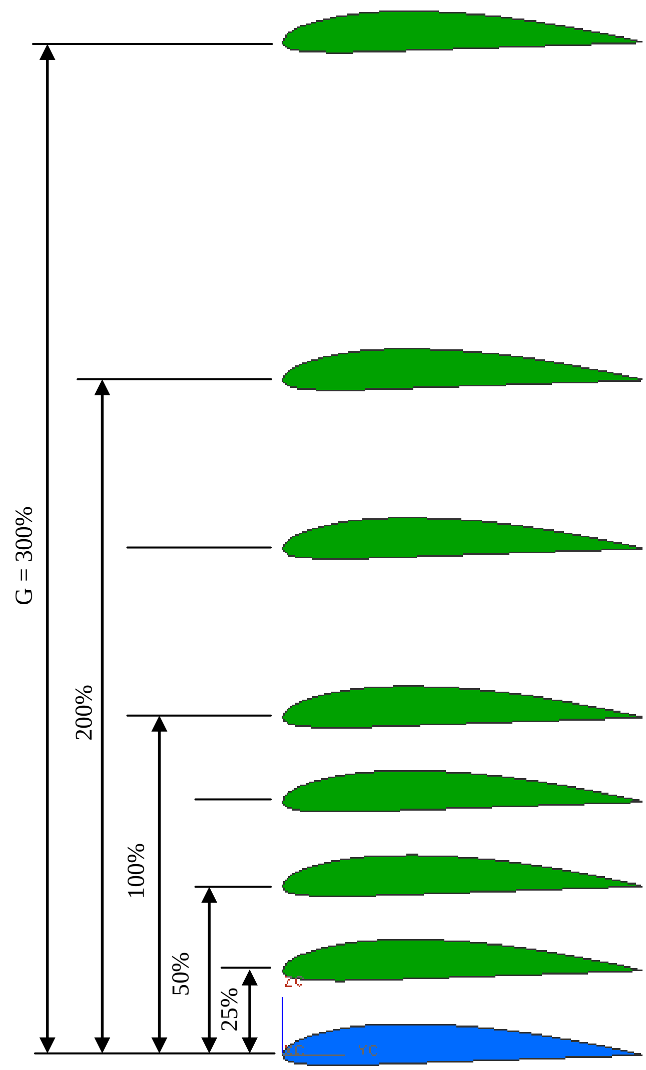

Figure 45. Bi-planes cellules that were examined.

6.3 Loading and Boundary Conditions

The boundary conditions and applied loads are the same as for the single foil, i.e. the FREE slip condition is imposed on each foil and the velocity upstream is unity. For each model of the 7 cellules shown above, the pressure distribution curve was calculated for the upper foil and for the lower foil. For each model of the cellules, 4 different angles of attack were applied: -6°, -2°, +2° and +6°.

6.4 CFD Analysis and Results

Surveying literature led to reference [20] which has experimental results for a bi-plane cellule composed of 2 identical Clark-Y foils. The results include graphs of lift and moment coefficients for 4 out of the 7 cellules described above where the range of angle of attack is from -10° to 90°. Since this research deals with small angles of attack where no separation occurs and the flow can be considered as potential, the comparison was made for the range of -6° to 6°. The 4 cellules described in [20] are G= 50%, 75%, 100% and 150%.

The comparison was made for the upper foil, lower foil and the cellule for the lift and moment coefficients for each of the 4 angles of attack. Each of those 6 curves (per angle of attack) was plotted versus the chord space factor which is the gap between the vertical foils over the chord length, i.e. $\frac{G}{c}$. In addition, a summary of those 24 graphs (figures 56÷79) is given in 6 graphs (figures 81÷86) describing the lift and moment coefficients of upper foil, lower foil and the cellule. Those graphs include all of the 7 cellules together, are plotted versus the angle of attack. The moment coefficient is plotted with respect to the leading edge of the foil and not its middle as performed in the experiments in [20]. In addition to those 30 following figures, plotting the pressure distribution curves for both the upper and lower foils for the 4 different angles of attack is given. Each of those 8 graphs (figures 48÷55) contains all of the 7 different cellules together. For each of the 38 graphs, the results of the single foil under the same conditions are also given for easy and comfortable comparison.

The following figure demonstrates the meshed model of the bi-plane case when the gap between the foils is G = 50%. In addition, the velocity field at +6° is given as well in the second figure in order to show to the reader how clear is that view in ADINA. This case was chosen coincidentally.

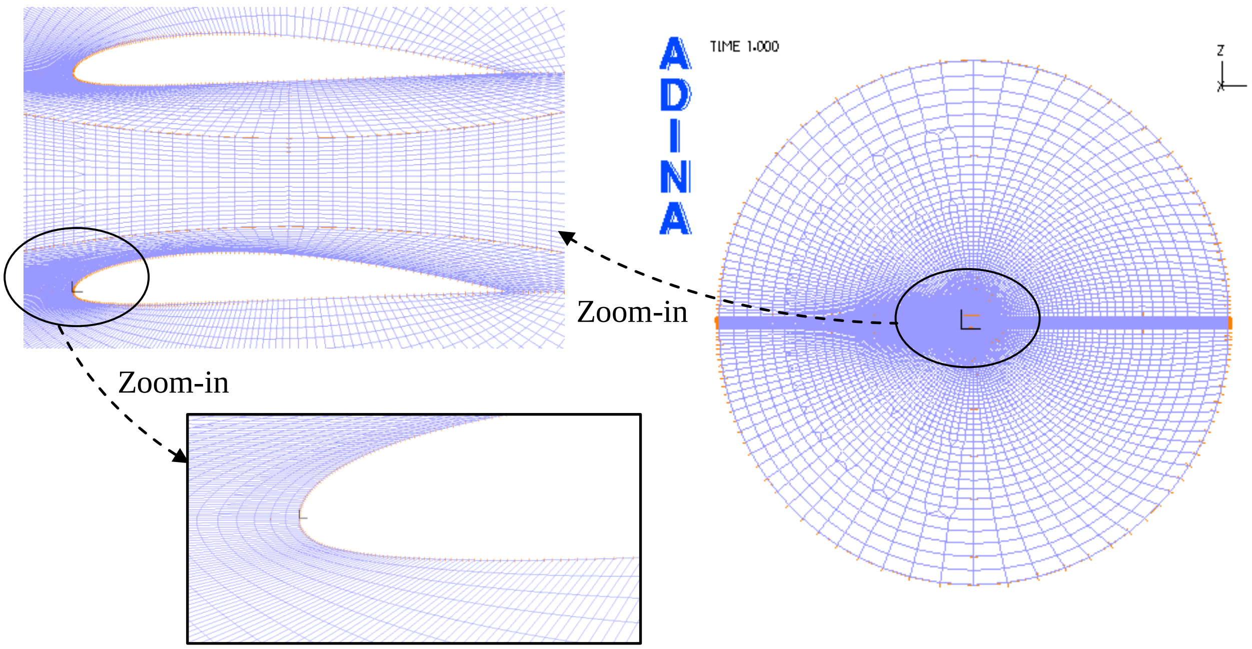

Figure 46. Bi-plane meshed model in ADINA for G=50%.

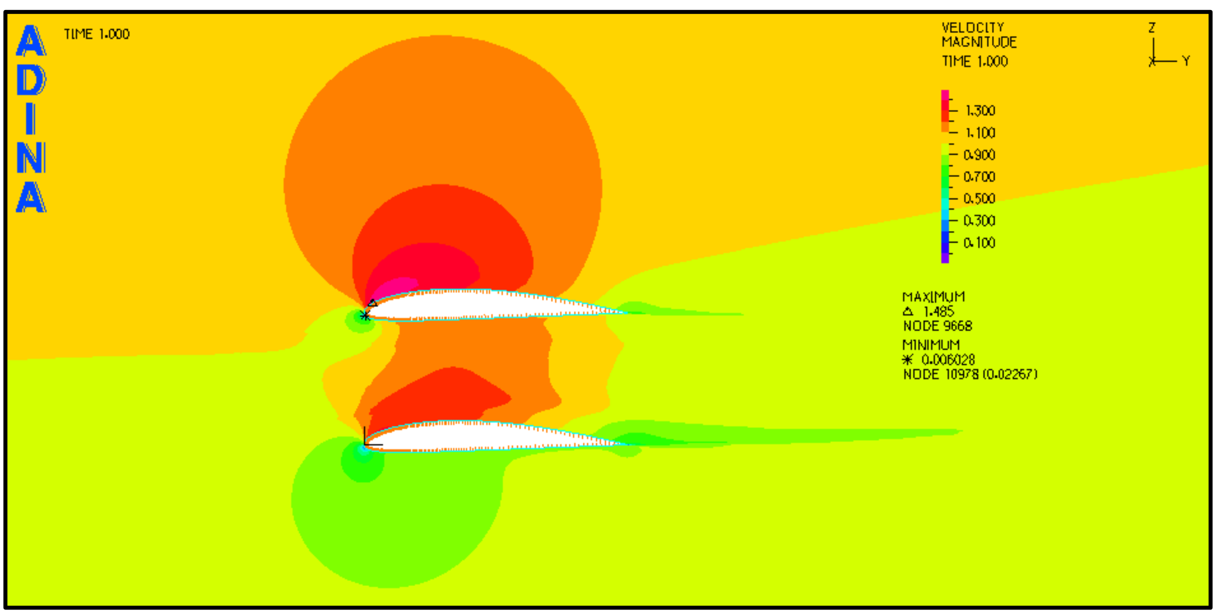

Figure 47. Bi-plane velocity field in ADINA for G=50% at +6°.

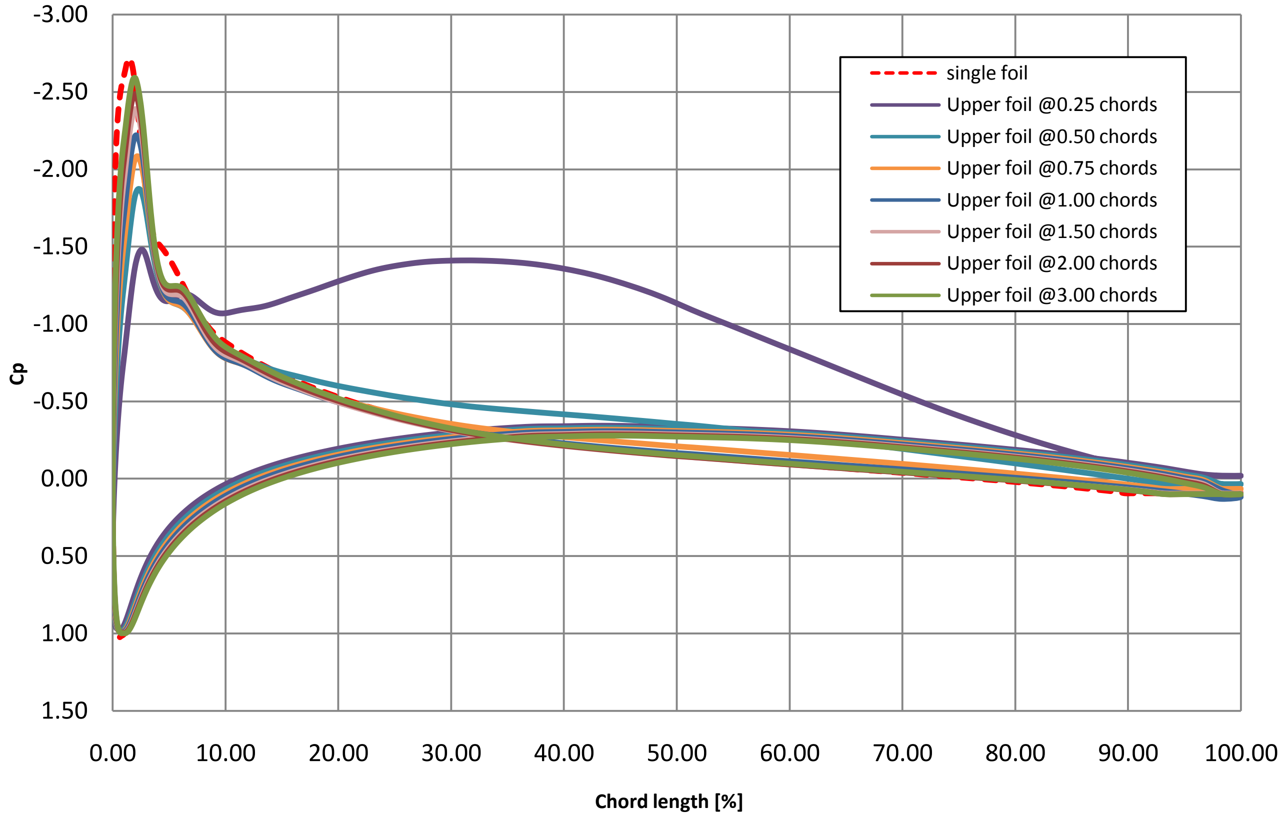

Figure 48. Pressure distribution curve of upper foil at -6°.

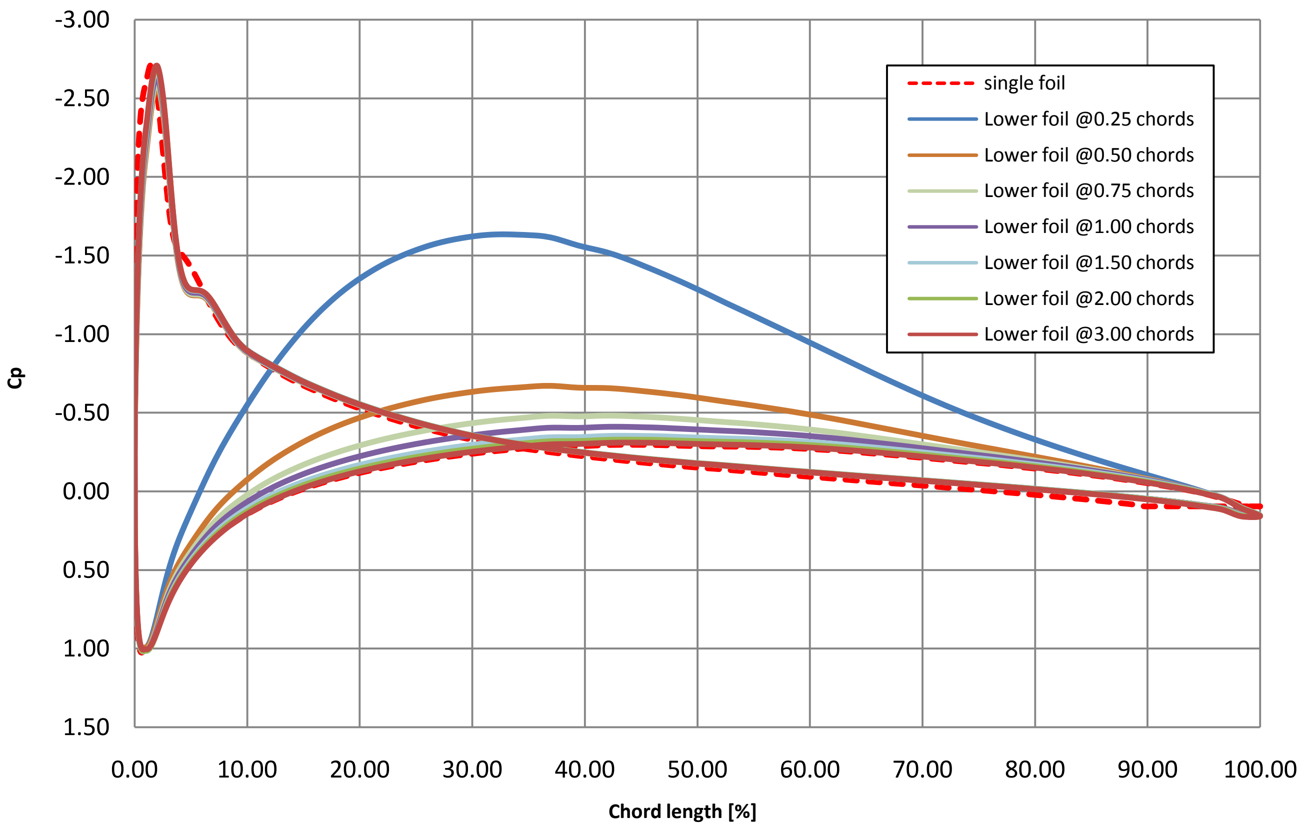

Figure 49. Pressure distribution curve of lower foil at -6°.

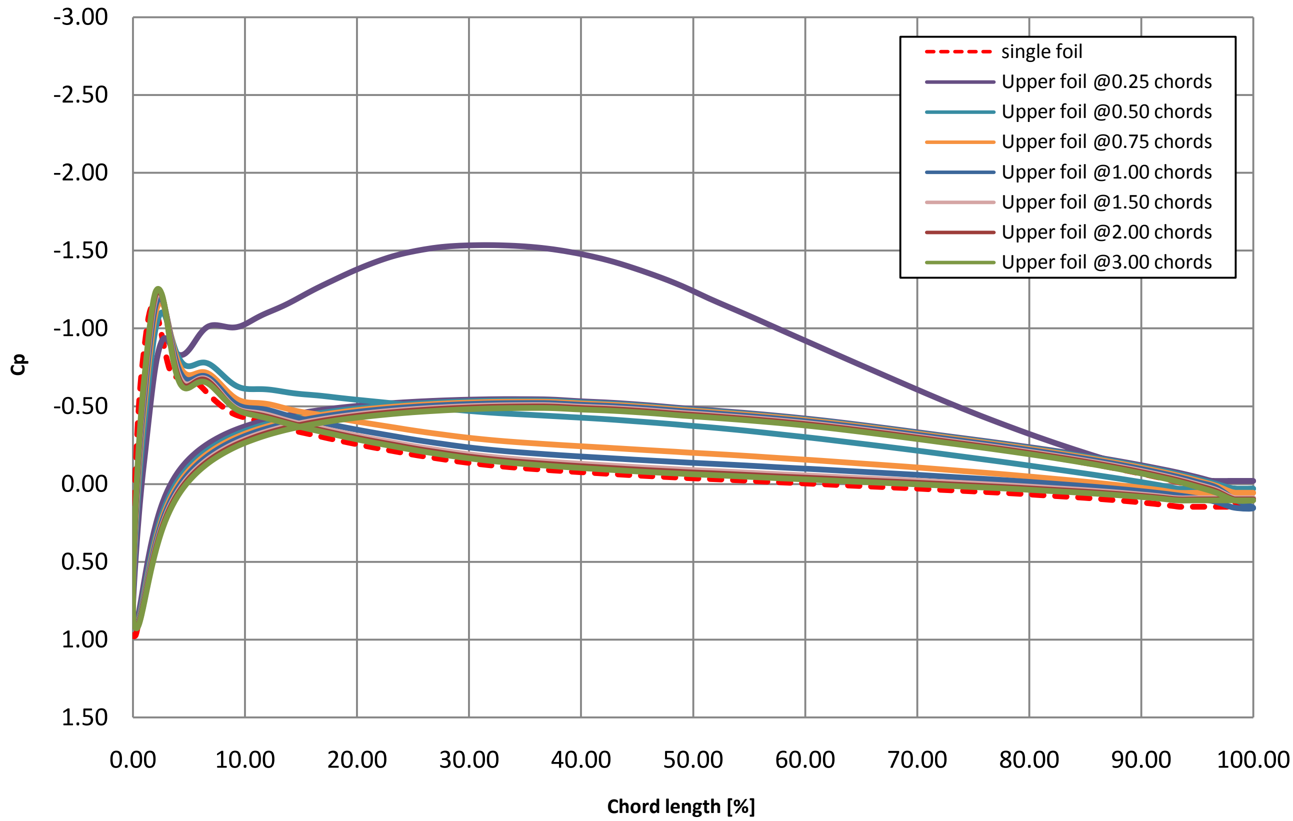

Figure 50. Pressure distribution curve of upper foil at -2°.

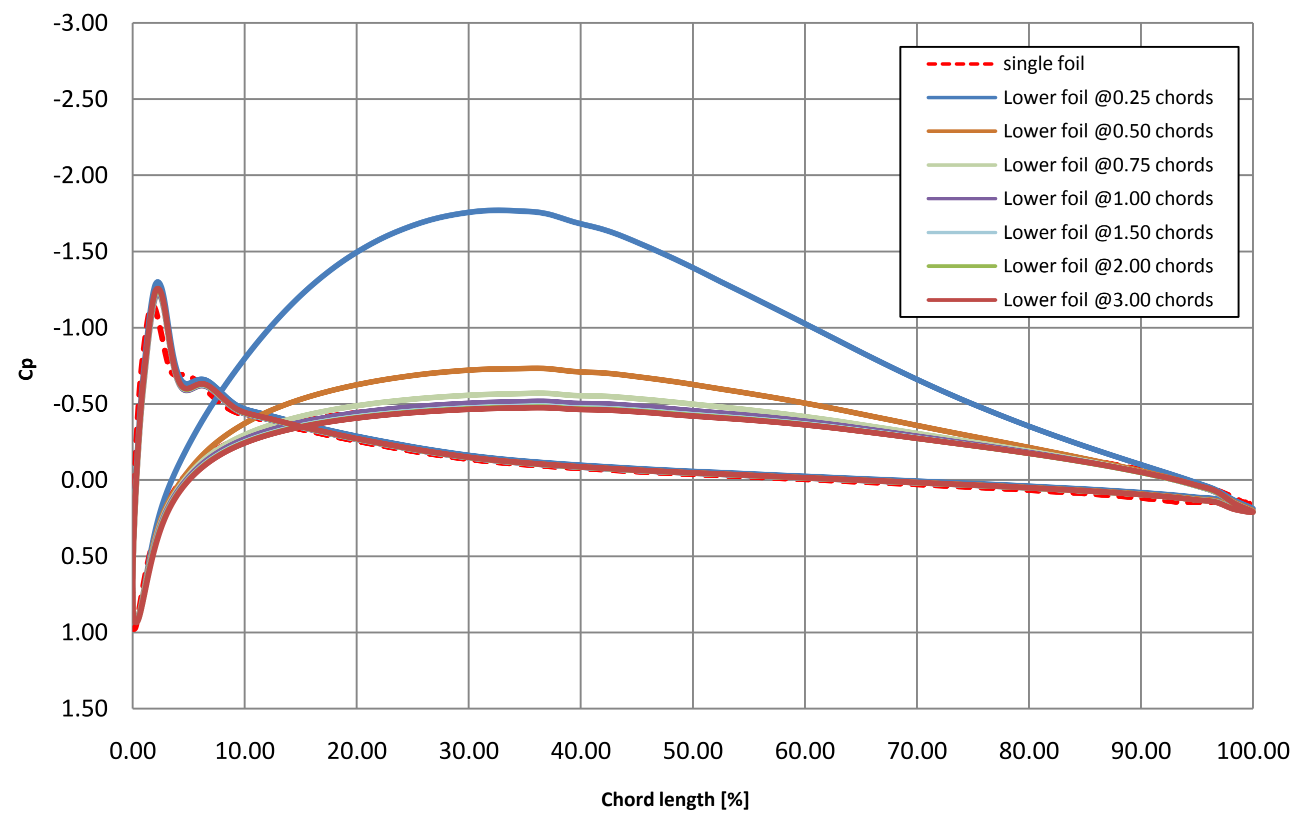

Figure 51. Pressure distribution curve of lower foil at -2°.

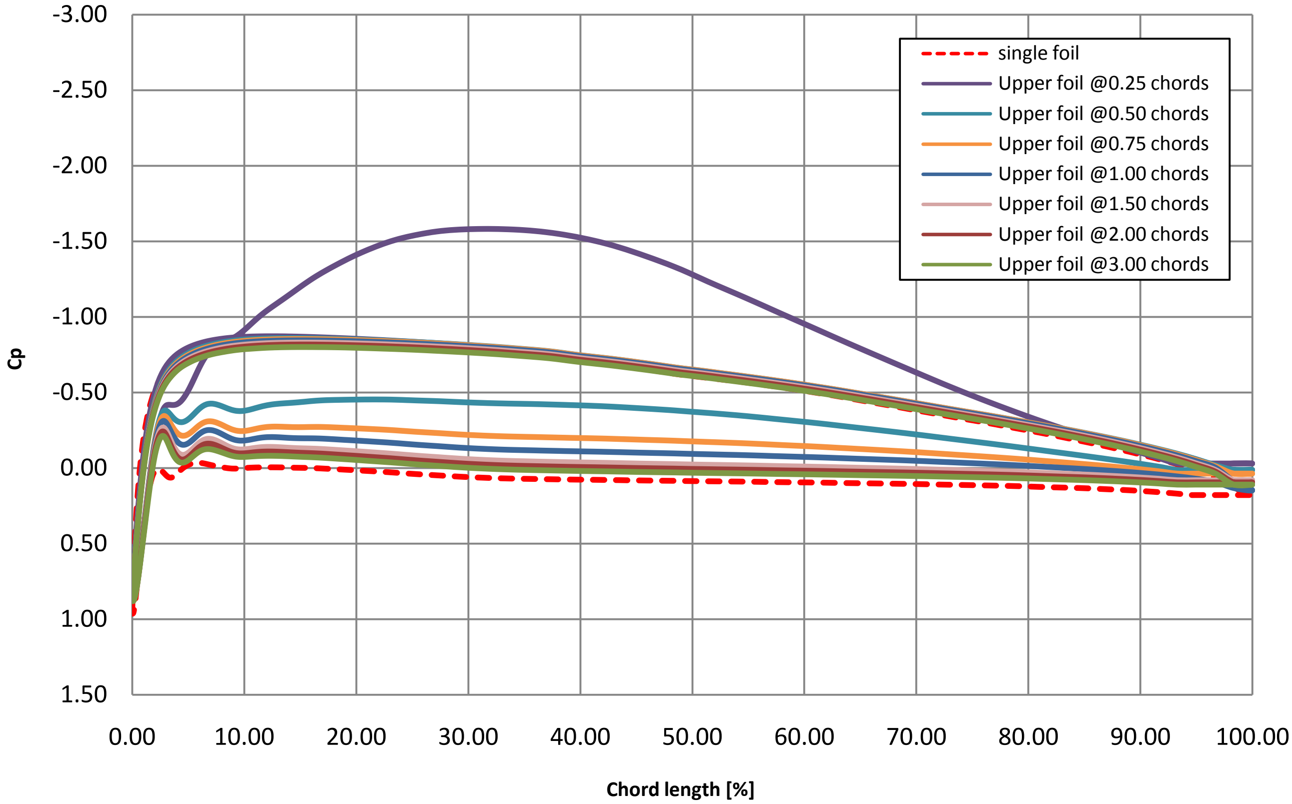

Figure 52. Pressure distribution curve of upper foil at +2°.

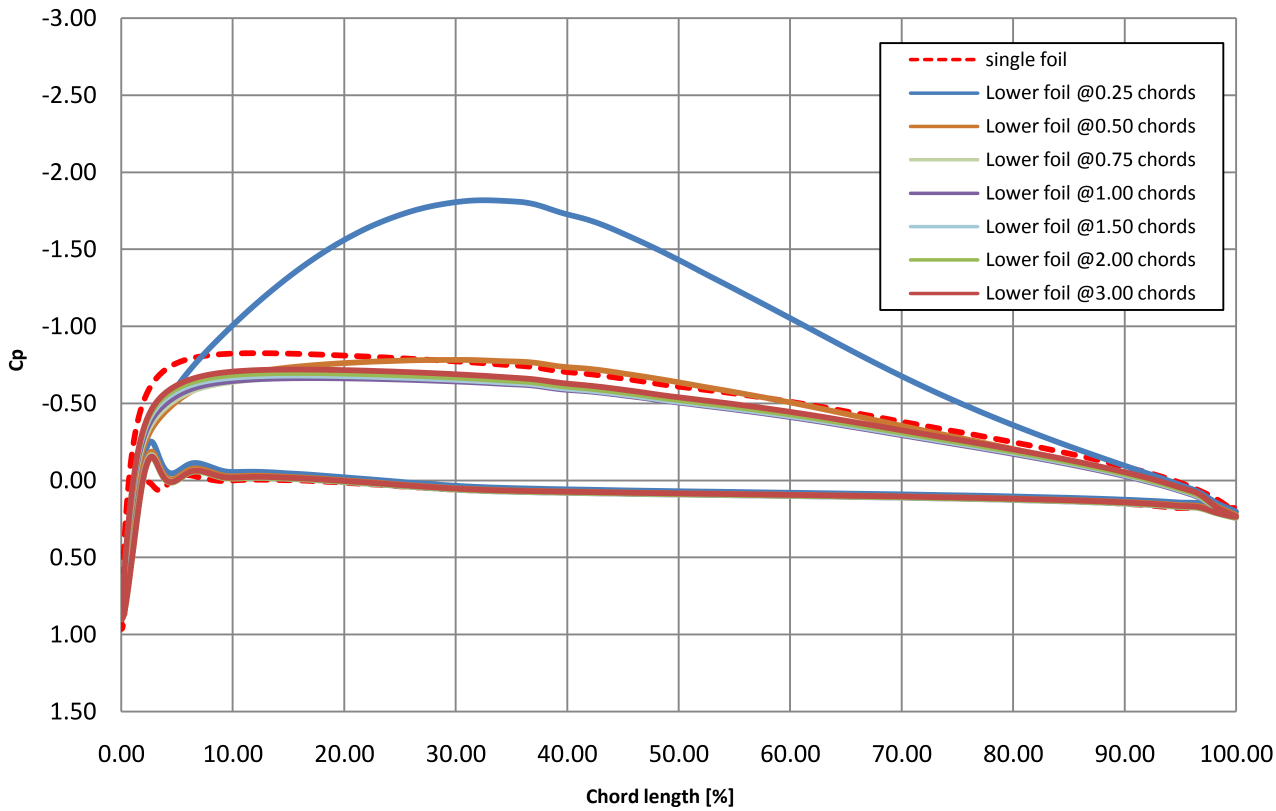

Figure 53. Pressure distribution curve of lower foil at +2°.

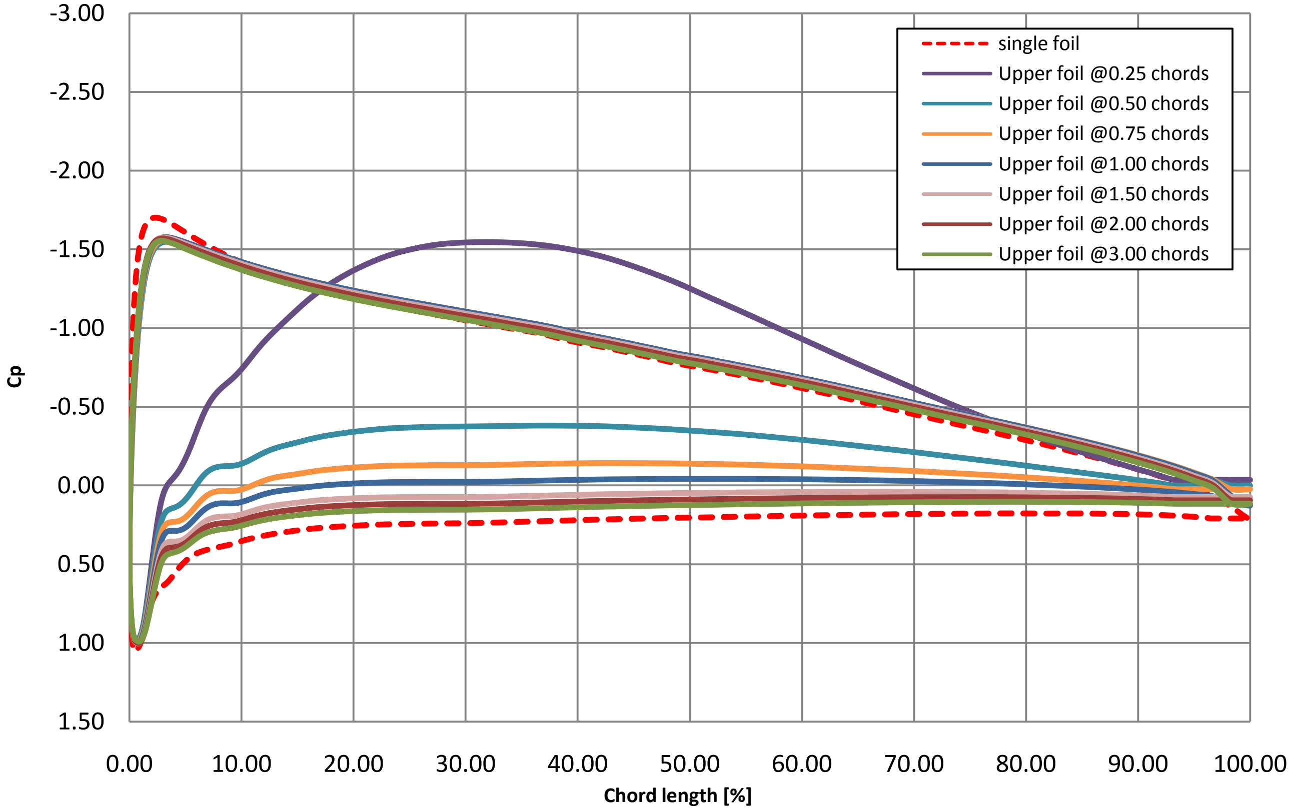

Figure 54. Pressure distribution curve of upper foil at +6°.

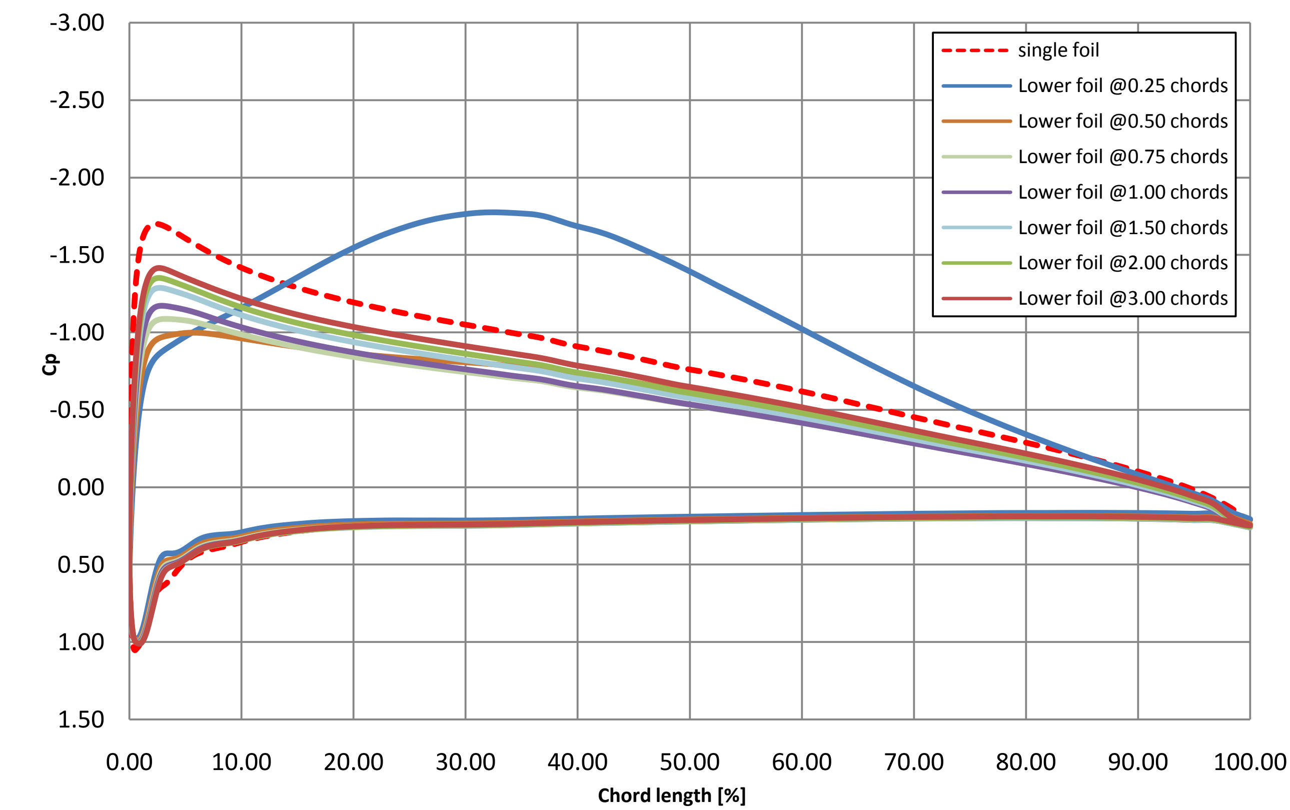

Figure 55. Pressure distribution curve of lower foil at +6°.

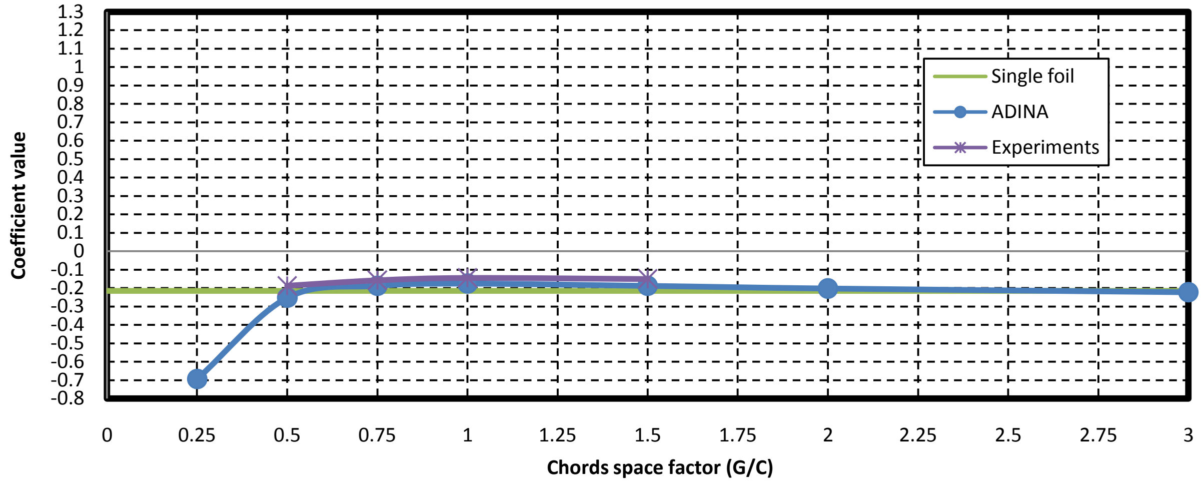

Figure 56. Lift Coefficient of upper foil at -6°.

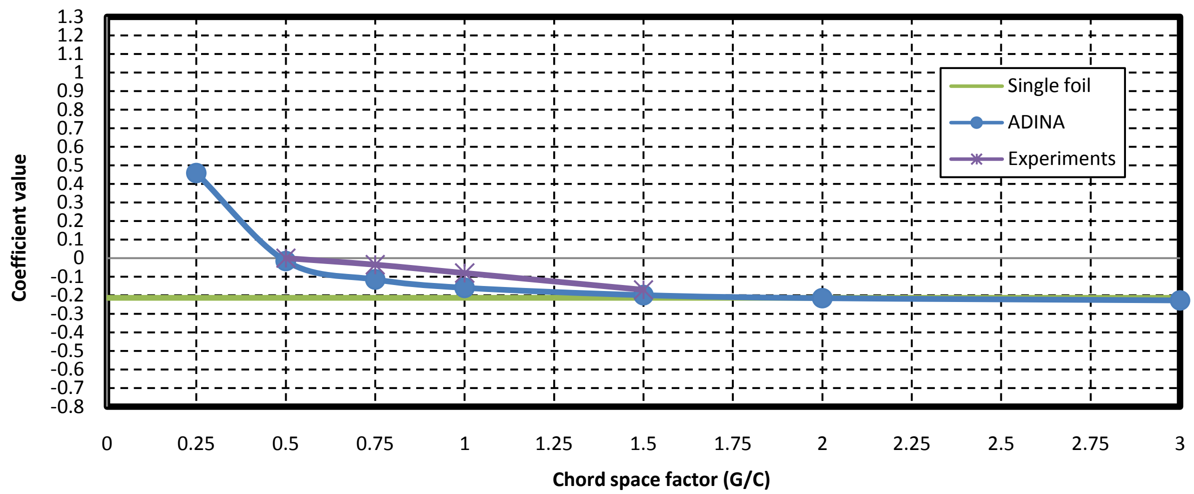

Figure 57. Lift Coefficient of lower foil at -6°.

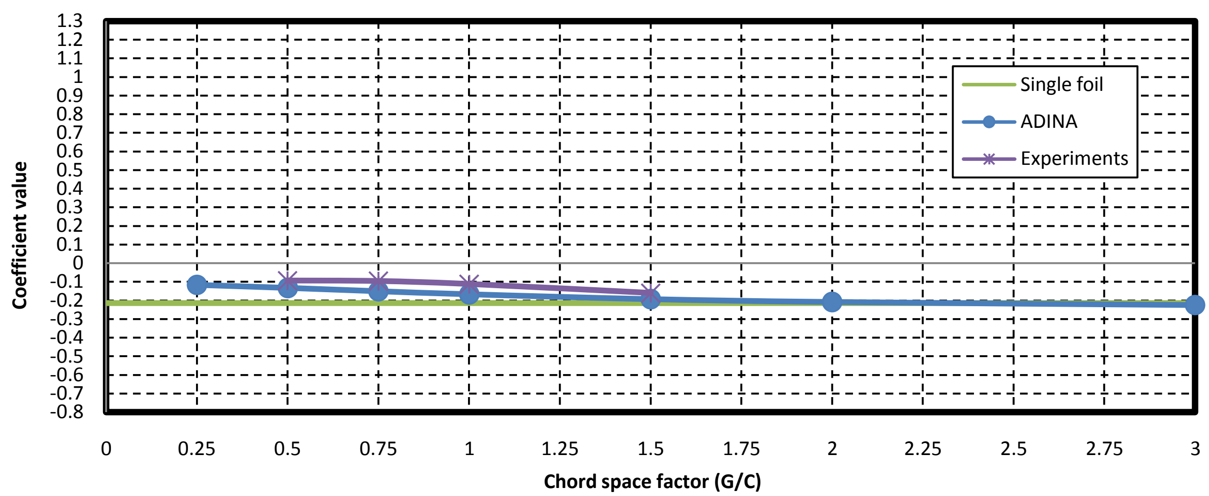

Figure 58. Lift Coefficient of cellule at -6°.

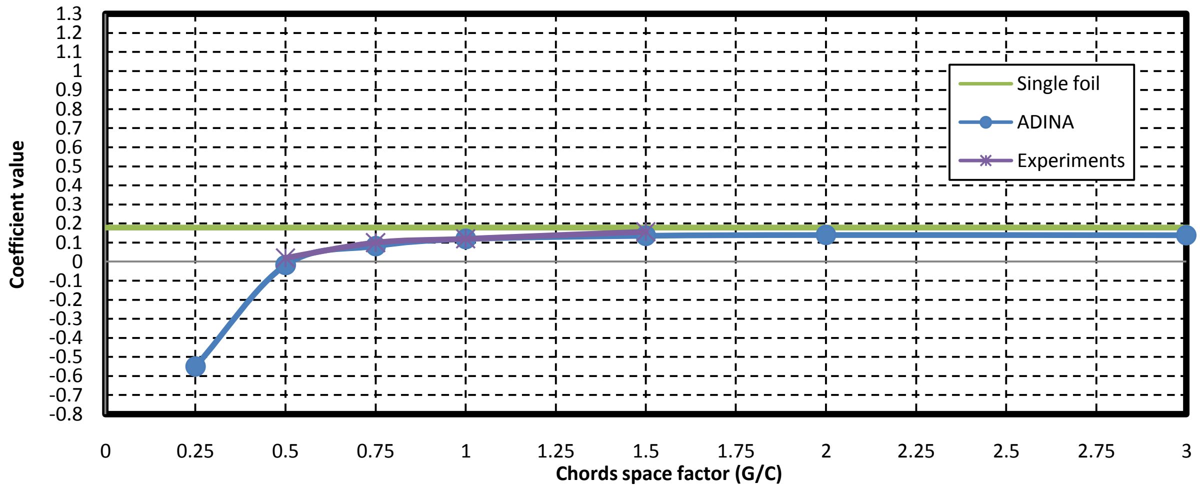

Figure 59. Lift Coefficient of upper foil at -2°.

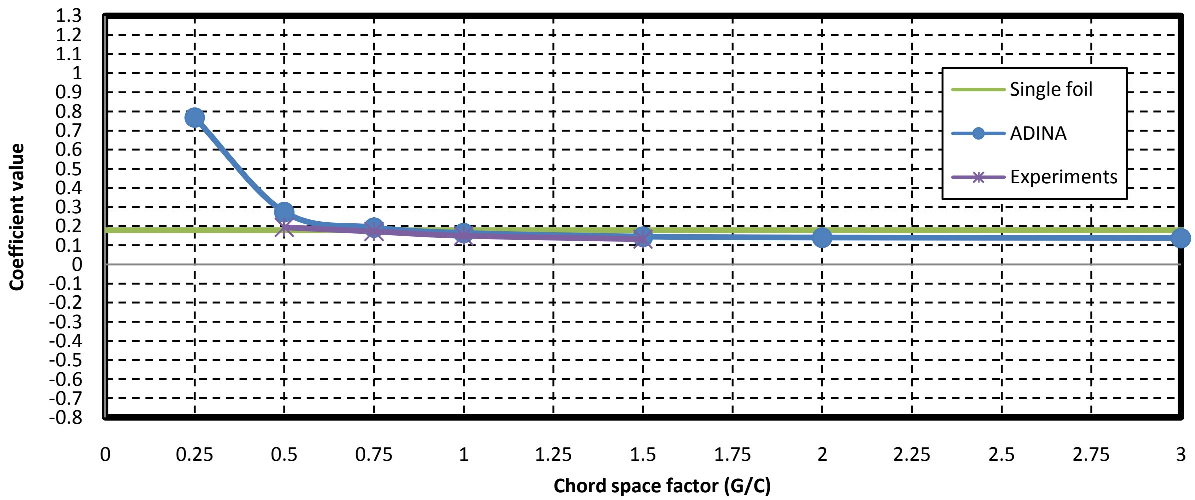

Figure 60. Lift Coefficient of lower foil at -2°.

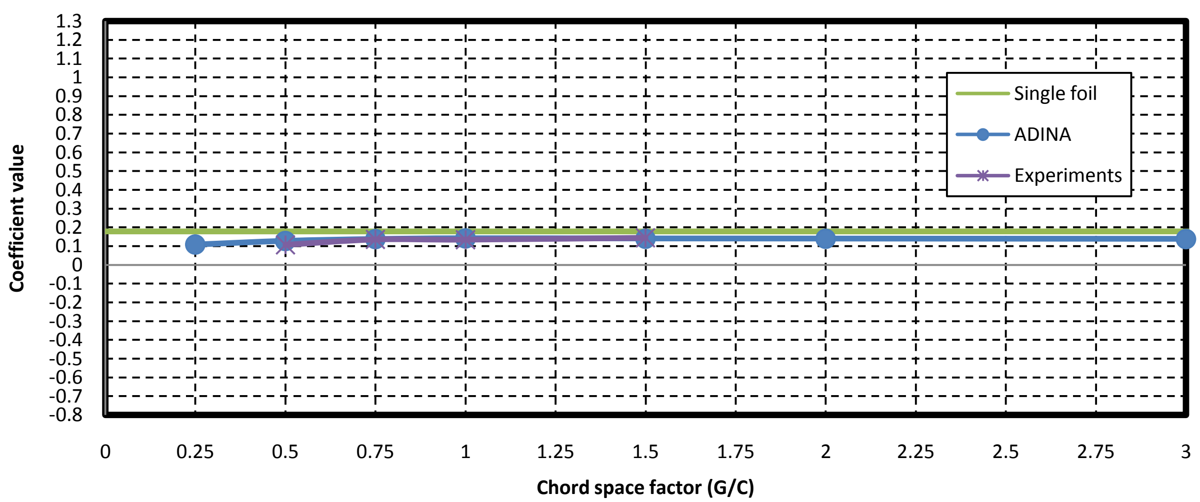

Figure 61. Lift Coefficient of cellule at -2°.

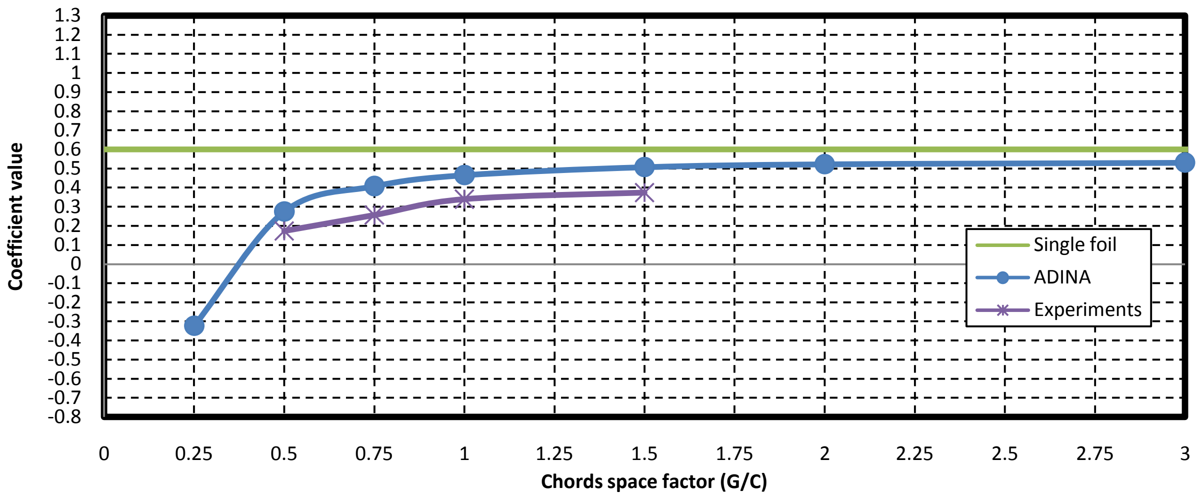

Figure 62. Lift Coefficient of upper foil at +2°.

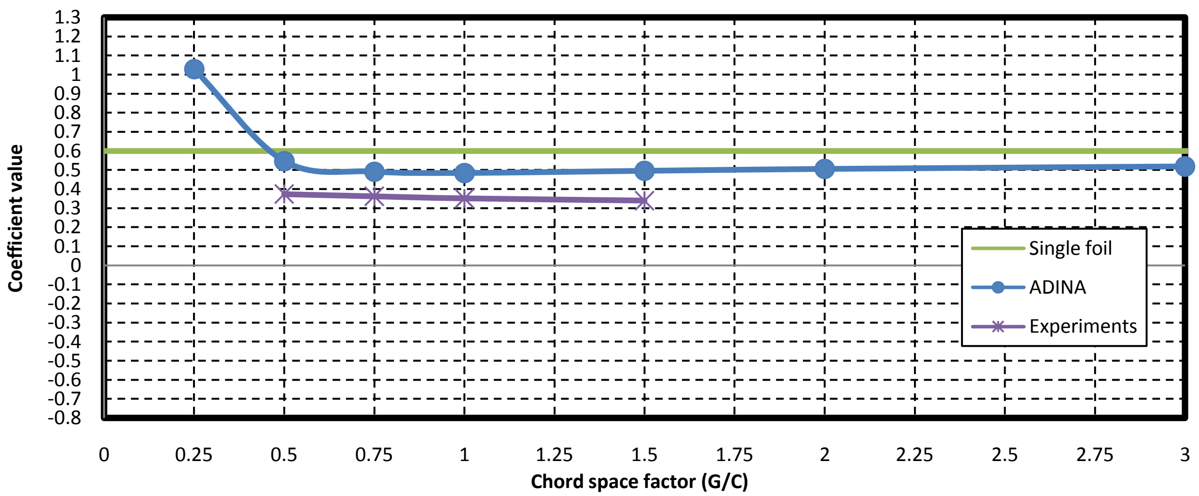

Figure 63. Lift Coefficient of lower foil at +2°.

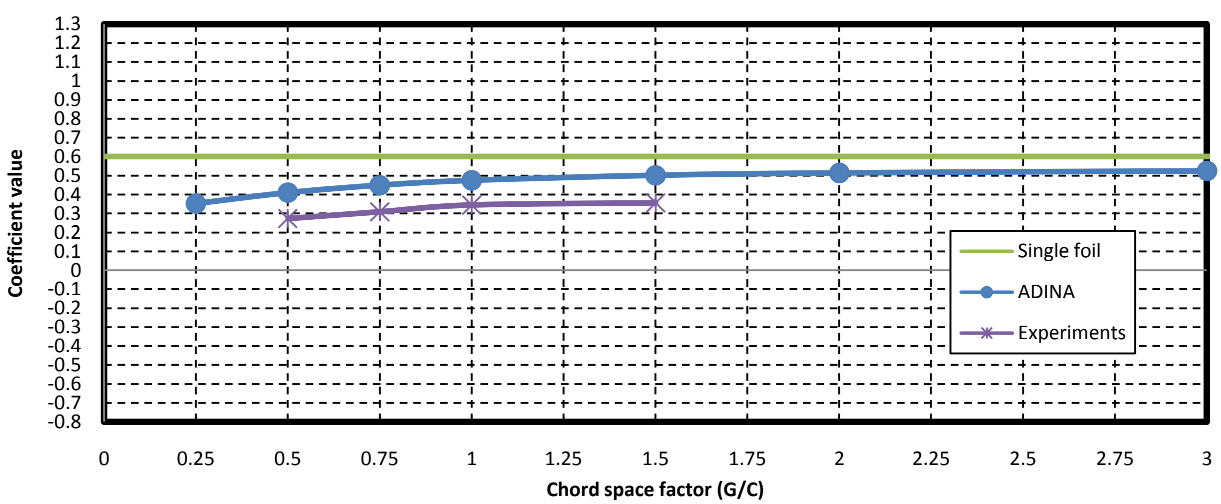

Figure 64. Lift Coefficient of cellule at +2°.

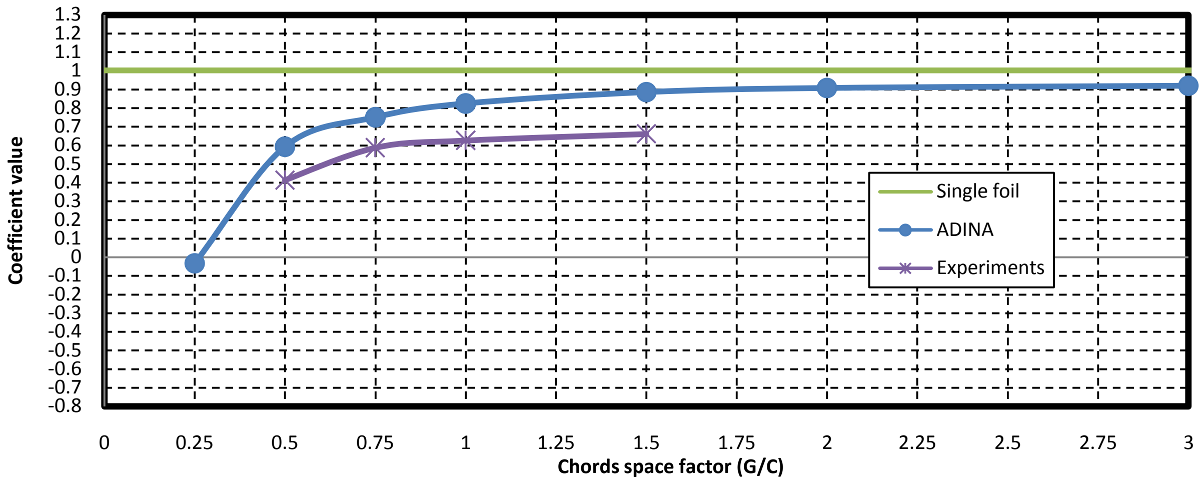

Figure 65. Lift Coefficient of upper foil at +6°.

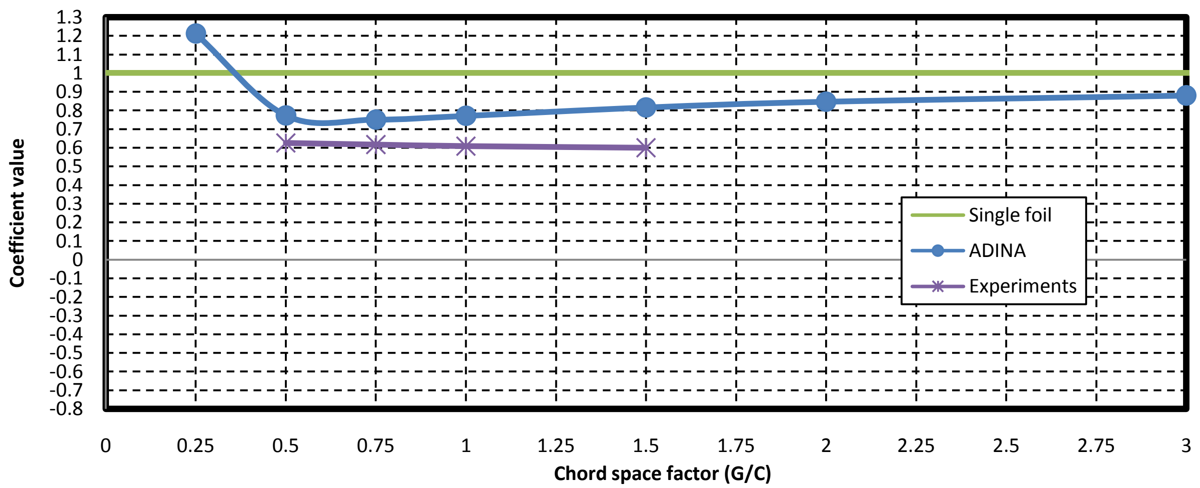

Figure 66. Lift Coefficient of lower foil at +6°.

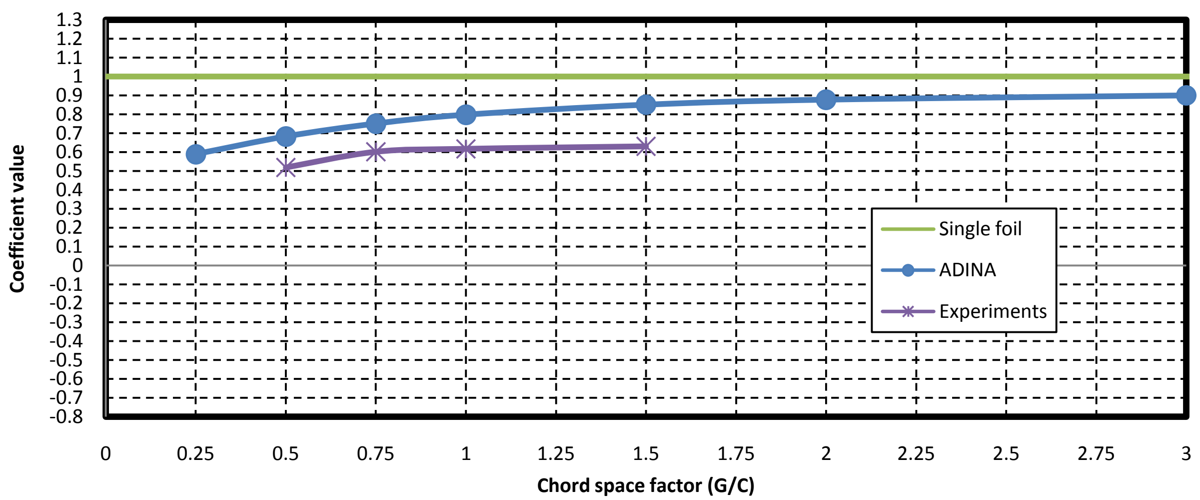

Figure 67. Lift Coefficient of cellule at +6°.

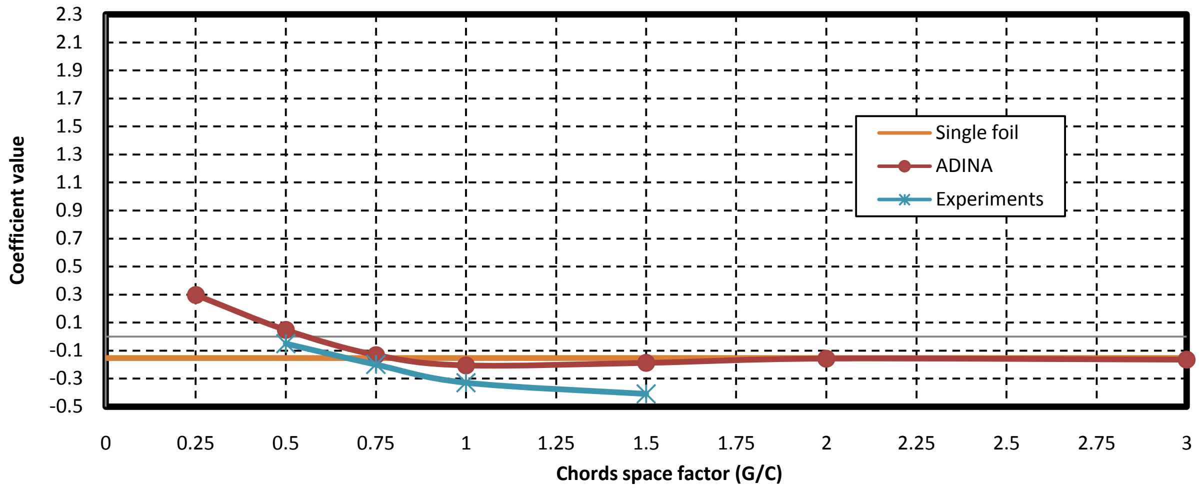

Figure 68. Moment Coefficient of upper foil at -6°.

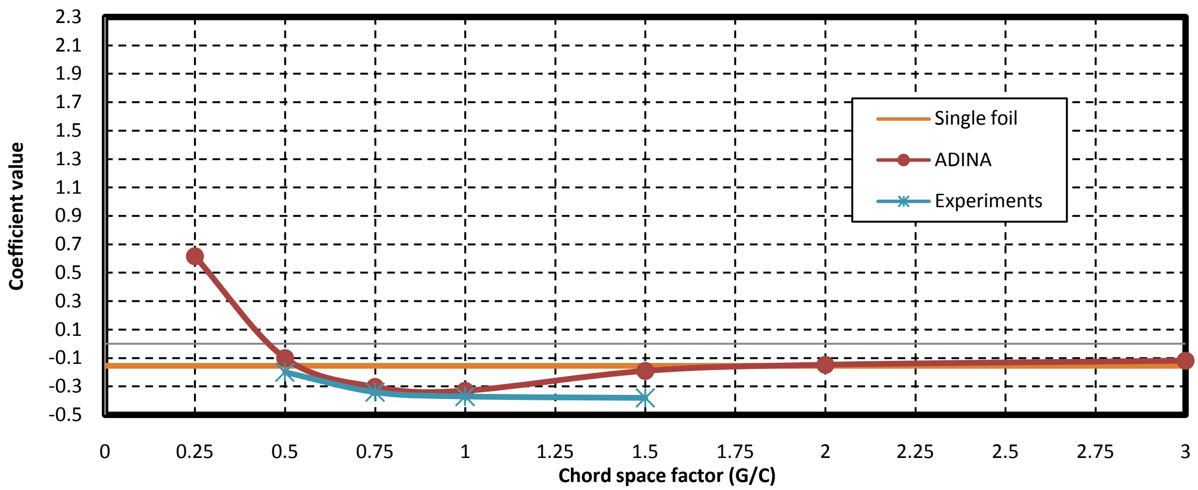

Figure 69. Moment Coefficient of lower foil at -6°.

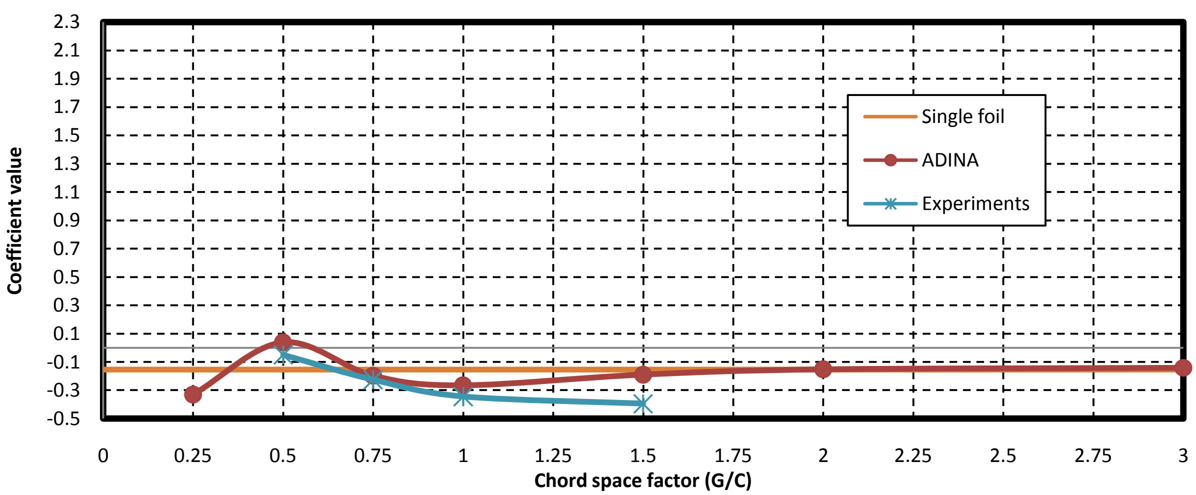

Figure 70. Moment Coefficient of cellule at -6°.

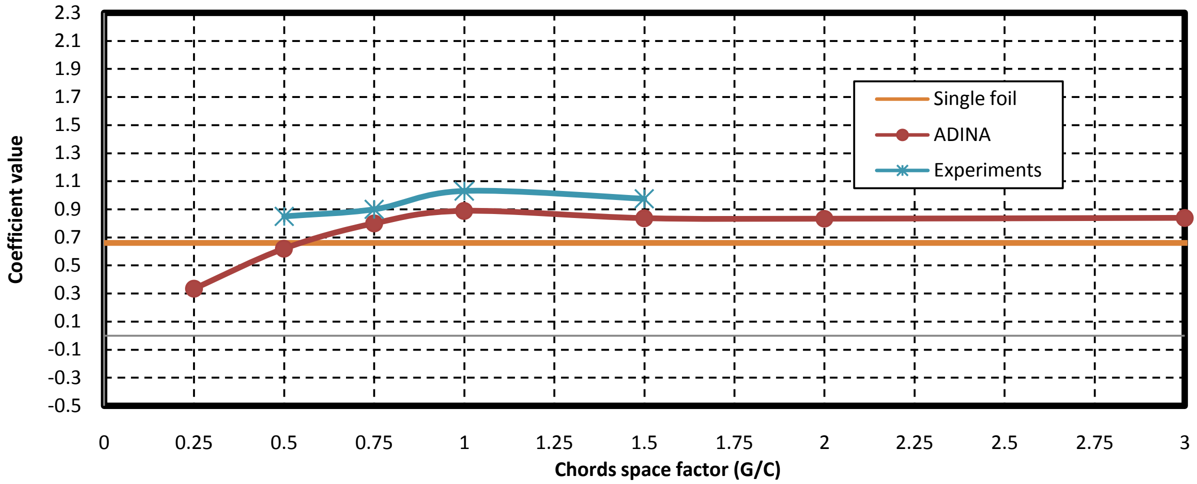

Figure 71. Moment Coefficient of upper foil at -2°.

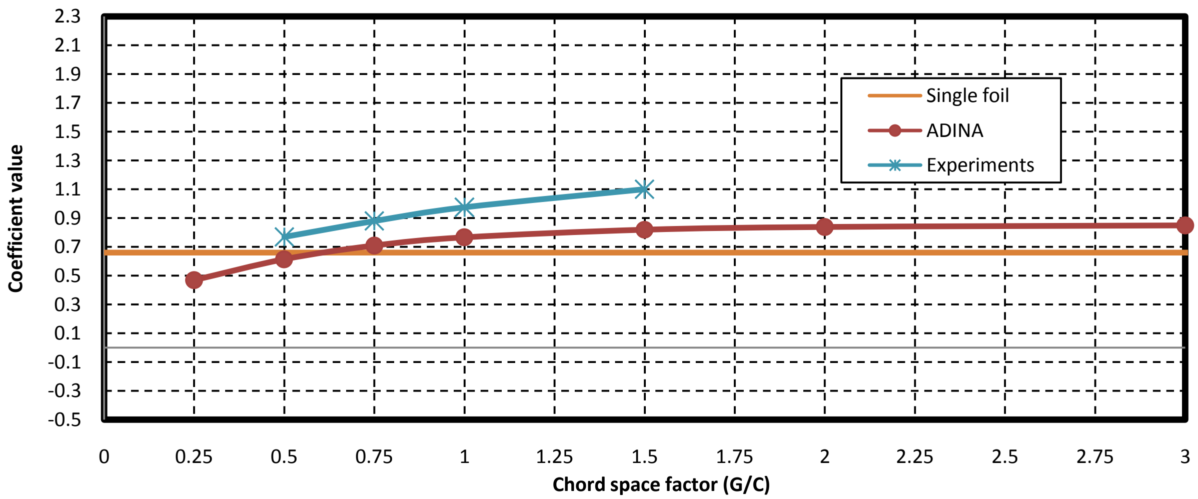

Figure 72. Moment Coefficient of lower foil at -2°.

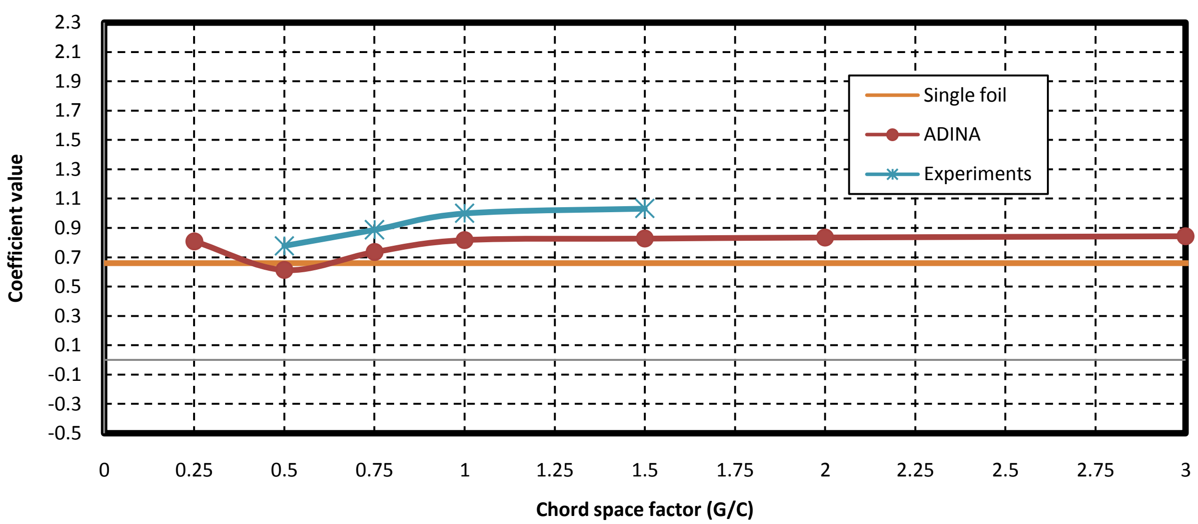

Figure 73. Moment Coefficient of cellule at -2°.

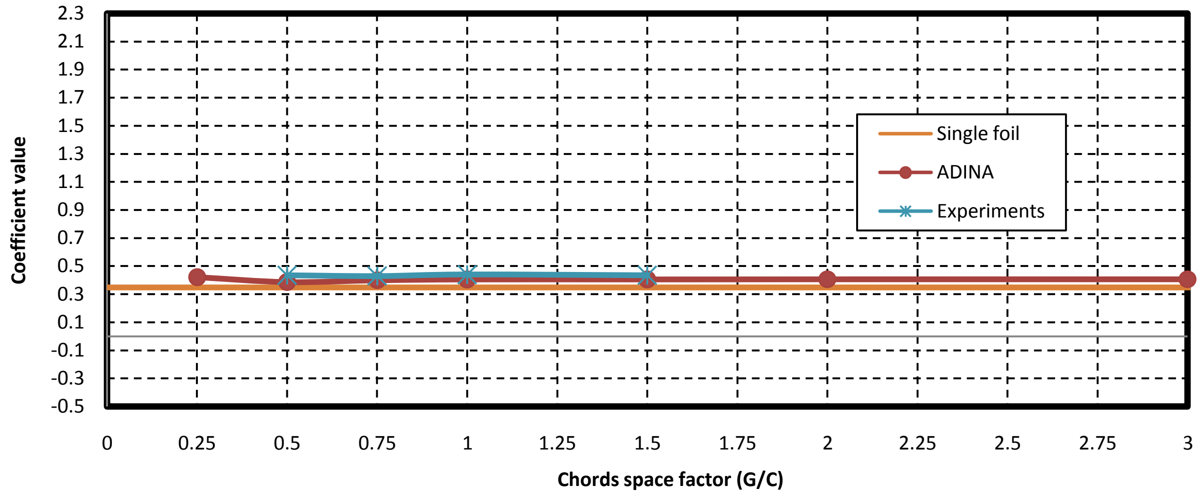

Figure 74. Moment Coefficient of upper foil at +2°.

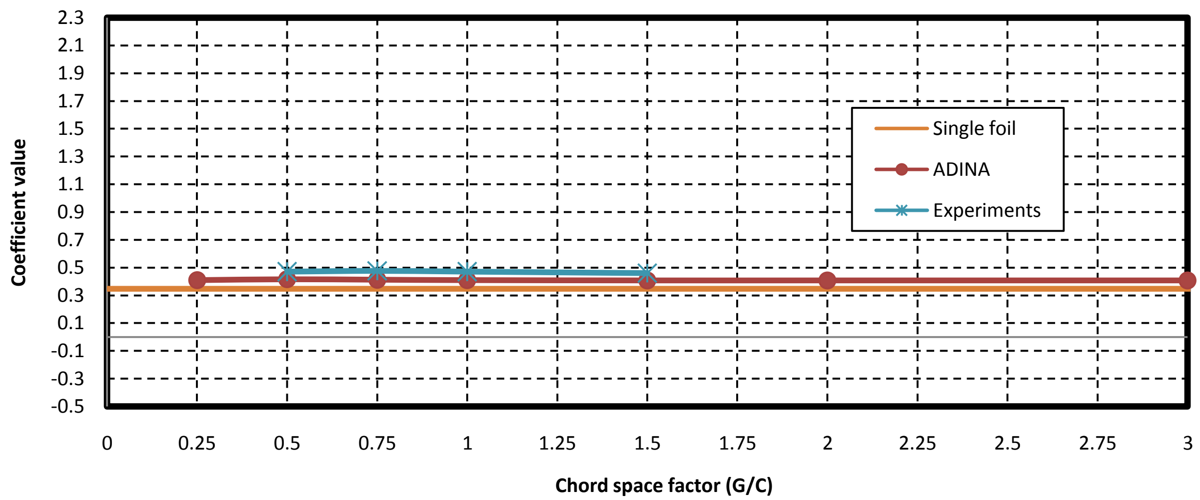

Figure 75. Moment Coefficient of lower foil at +2°.

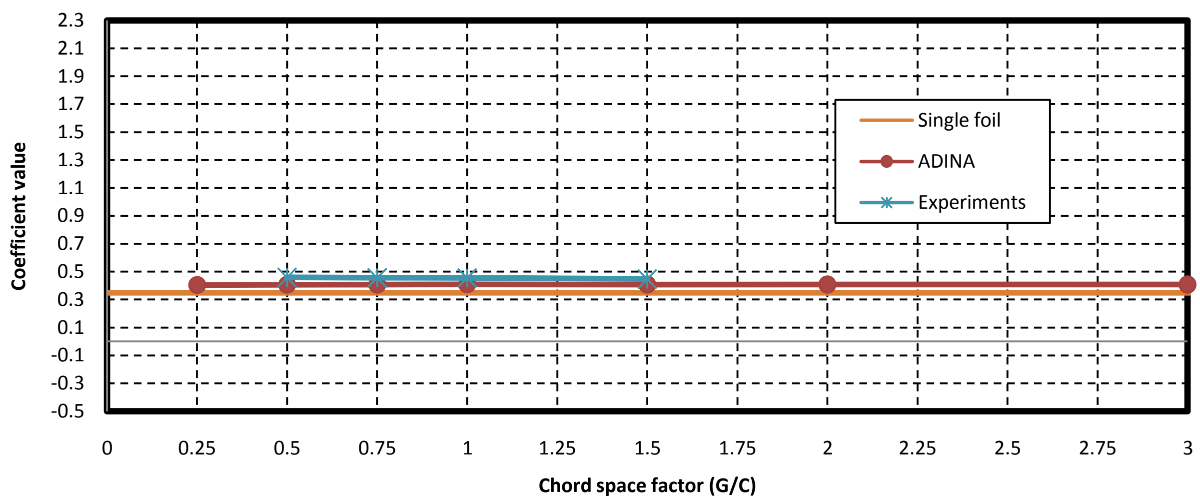

Figure 76. Moment Coefficient of cellule at +2°.

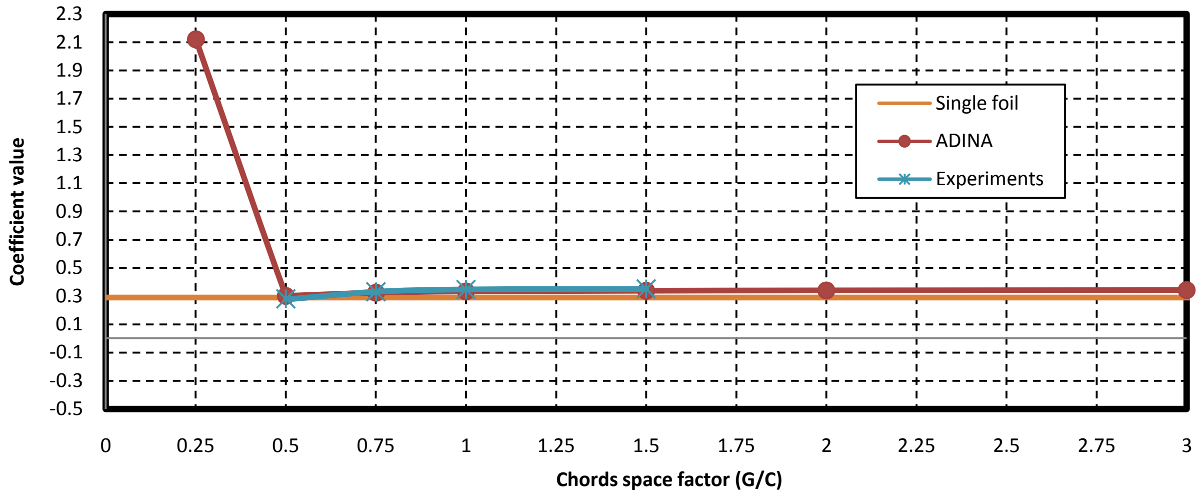

Figure 77. Moment Coefficient of upper foil at +6°.

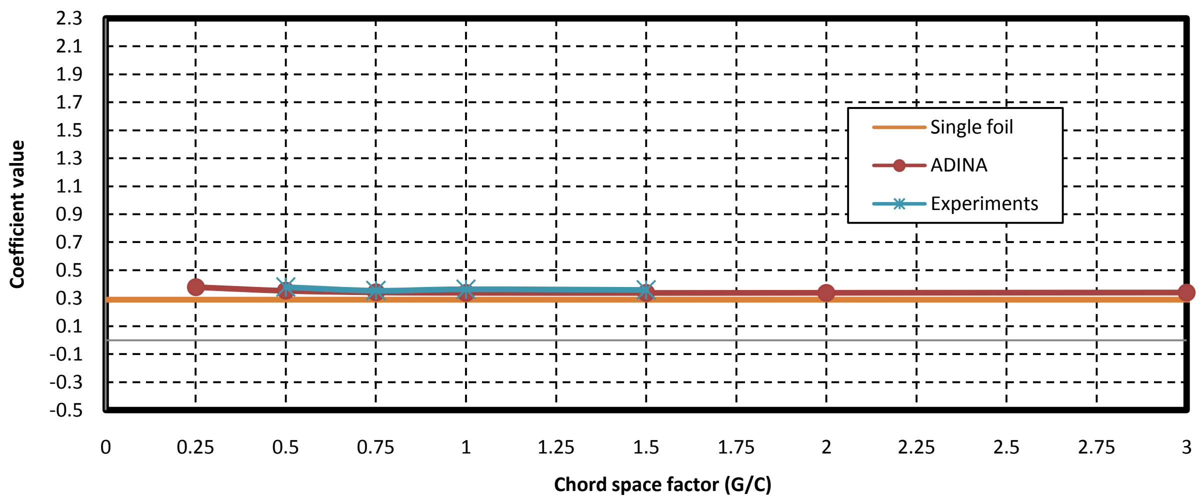

Figure 78. Moment Coefficient of lower foil at +6°.

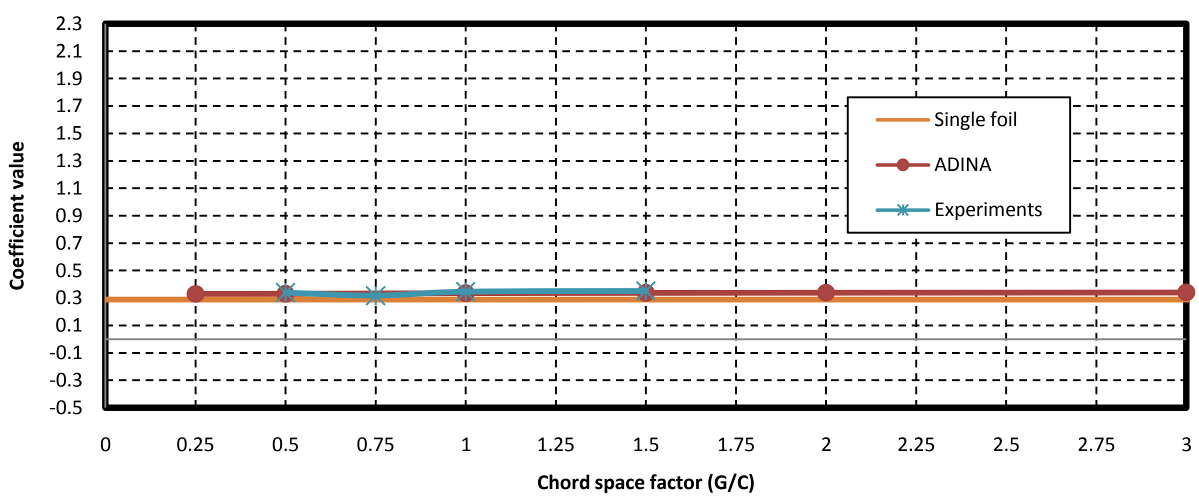

Figure 79. Moment Coefficient of cellule at +6°.

6.5 Discussion of the Results

The main observation that can be made out of the results in the graphs above is that there is high correlation between the CFD results obtained with ADINA and the experimental results given in [20]. Although there are some zones in the graphs where the curves of the lift and moment coefficients are not quite the same between the CFD and the experiments, those gaps can be related to inaccuracies in the experiments since those were performed in 1929 and it is reasonable to assume that the measurement devices, the equipment of the experiments and the foil geometry were not ideal at all. However, in spite of that main reason, the matching of the results is definitely satisfying.

Another prominent finding from the graphs is the behavior of the lift and moment coefficient curves obtained in CFD. One can easily notice how the CFD curves are smooth and act almost as expected in theory. There are not any breaks or distortions of the curves which imply that the CFD model mesh is refined enough and very accurate. As mentioned in chapter 3, the CFD model can never be exact but when refined enough the accuracy tends to be almost perfect.

An expected behavior is also observed from the graphs as one looks on the lift and moment coefficients curves when the distance between the foils gets bigger, i.e. the relation $\frac{G}{c}$ grows up. The lift and moment coefficients of each of the foils, the upper foil and the lower foil, tends to be the same as for a single foil as the distance between them grows up. Thus, the reciprocal influence between them gets weaker and each one of the foils acts as a single foil where there is no other interference in the flow except for itself.

One cannot ignore the surprising value obtained of the moment coefficient of the upper foil at +6°, when the gap between the foils is 25%, i.e. $\frac{G}{c}$=0.25 in the graph. In order to understand this unexpected numeric value of 2.12, one should notice the lift coefficient at that point as well: $C_{L_{upper\ foil}}$ = -0.033 which is almost zero. Since the area under the $C_{p_{upper\ foil}}$ curve at that case goes to zero, the lift coefficient becomes so small.

Consequently, when calculating the moment coefficient by dividing the total moment by the lift, a big numeric value is obtained. This value did not get changed by refining the mesh since the lift coefficient remains so small and thus should be considered with caution.

In addition to the upper and lower foils, the results for each cellule are given as well. The lift and moment coefficients of the cellule were calculated using the following formulas:

$$(63) \quad C_{L_{cellule}} = \frac{C_{L_{upper\ \ foil}} + C_{L_{lower\ \ foil}}}{2}$$

$$(64) \quad C_{M_{cellule}} = \frac{C_{M_{upper\ \ foil}} \cdot C_{L_{upper\ \ foil}} + C_{M_{lower\ \ foil}} \cdot C_{L_{lower\ \ foil}}}{C_{L_{upper\ \ foil}} + C_{L_{lower\ \ foil}}}$$

One of the interesting cases is when the gap between the foils of the bi-plane is 25%. For this case no experiments were done, probably because of the difficulty of executing such an experiment, as will be explained later. The pressure distribution curve behaves differently than curves of the other $\frac{G}{c}$ cases. That is true for all of the 4 angles of attack that the bi-plane case was examined for. When looking at the lift coefficient (figures 56÷67), one can see that the lift of the upper foil is always negative while the lift of the lower foil is always positive. In addition, according to the pressure distribution curve (figures 48÷55), it can be seen that the pressure along the upper part of the lower foil is small as well as the pressure along the lower part of the upper foil. However, the pressure along the upper part of the upper foil is strongly downwards and the pressure along the lower part of the lower foil is strongly upwards. This evidence, as well as the little distance between the 2 foils, led to the conclusion that when the gap is only 25%, the gap between the 2 foils functions as a channel for the flow. The velocity in the channel is much higher with relation to the surrounding flow (figure 80) which makes the pressure very low in between the foils. Consequently, the foils are being pulled to each other, as also pointed by the lift coefficient values of each of the foils. That conclusion points out that such a case where G=25% is neither feasible nor profitable and also why it is hard to conduct such an experiment as previously mentioned.

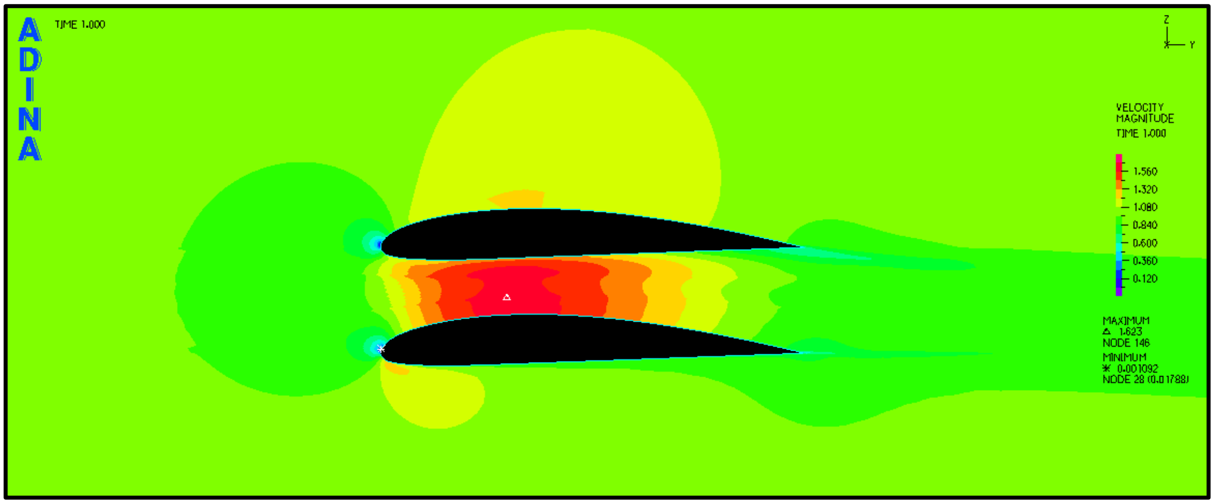

Figure 80. Higher velocity between the vertical foils for G=25% at α=-2°.

Looking carefully at the results of the moment coefficient of the cellule at G=25% at angle of attack of -6° (figure 70), a surprising value is revealed. While the behavior of the curve implies a positive value, a negative value is obtained. In order to understand this unexpected value, one should look at formula (64). While the numerator is positive, the denominator which is two times the total lift of the cellule is negative. Because of that, a negative value is obtained. That explanation is also relevant for the -2° angle of attack of the bi-plane.

The most important finding from the bi-plane analyses is obtained when gathering the above graphs and plotting the lift and moment coefficients of the lower foil, upper foil and the cellule versus the angle of attack. Those 6 graphs (figures 81÷86) are given below. According to those graphs, the lift of a bi-plane is always lower than of a single foil (for this Clark-Y foil). This finding points out that when the bi-plane airplanes were used widely about 50 years ago, there was another reason for having two wings on each side than its lift. The main reason for that was structural rather than stability or speed. At those times, the skin was made of cotton cloth and the spars were wood, thus there were two wings on each side for bending resistance and cross wires for torsion resistance. The only benefit (performance-wise) that bi-plane offered was low wing loading which allowed unbelievably tight turns. The following 6 figures describe the lift and moment coefficients of the lower foil, upper foil and the cellule versus the angle of attack. Notice the strange behavior of the bi-plane when the gap between the foils is 25%. In addition, the moment coefficient was plotted with relation to the leading edge of the foils.

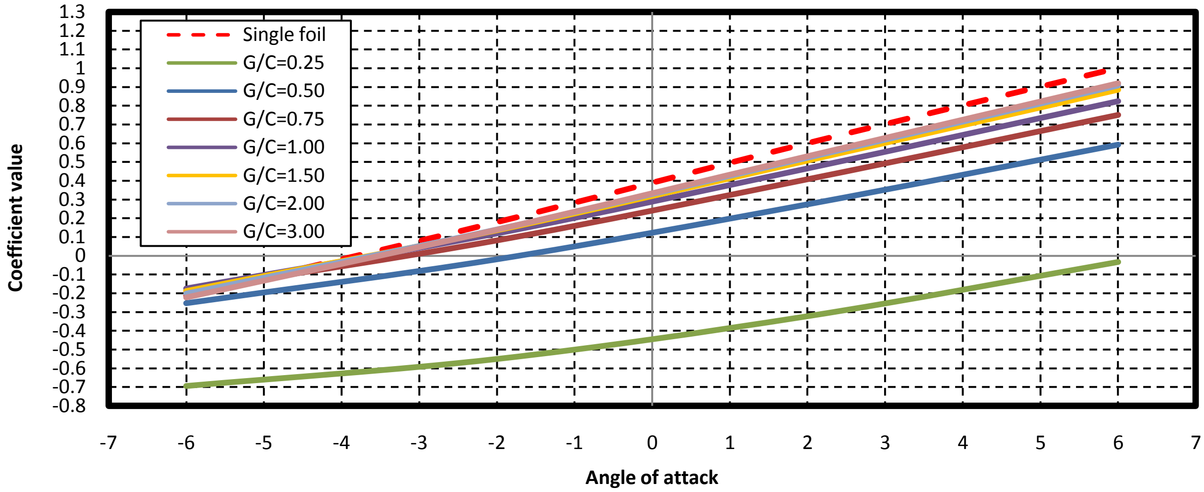

Figure 81. Lift Coefficient of upper foil vs. angle of attack.

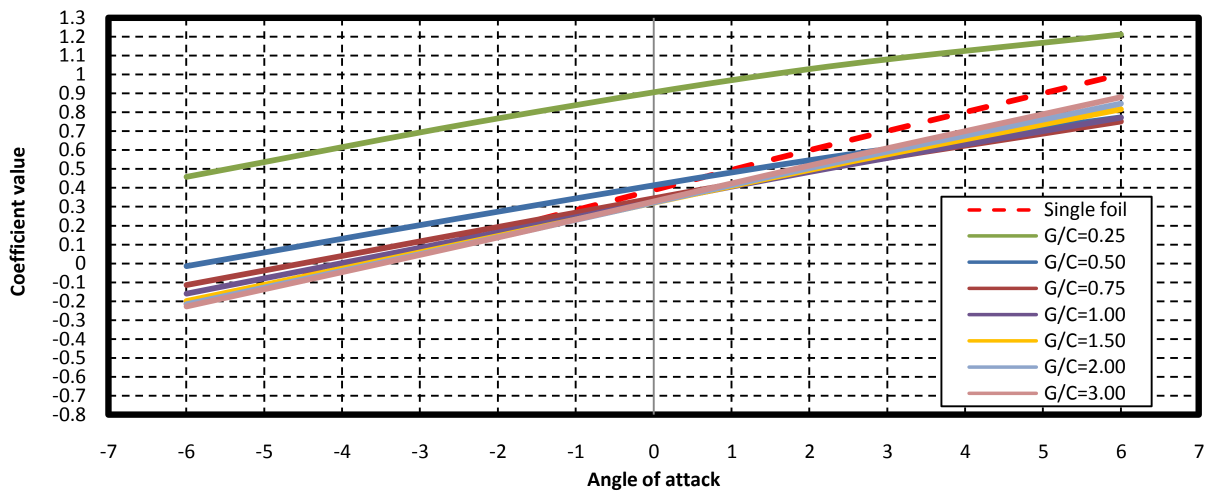

Figure 82. Lift Coefficient of lower foil vs. angle of attack.

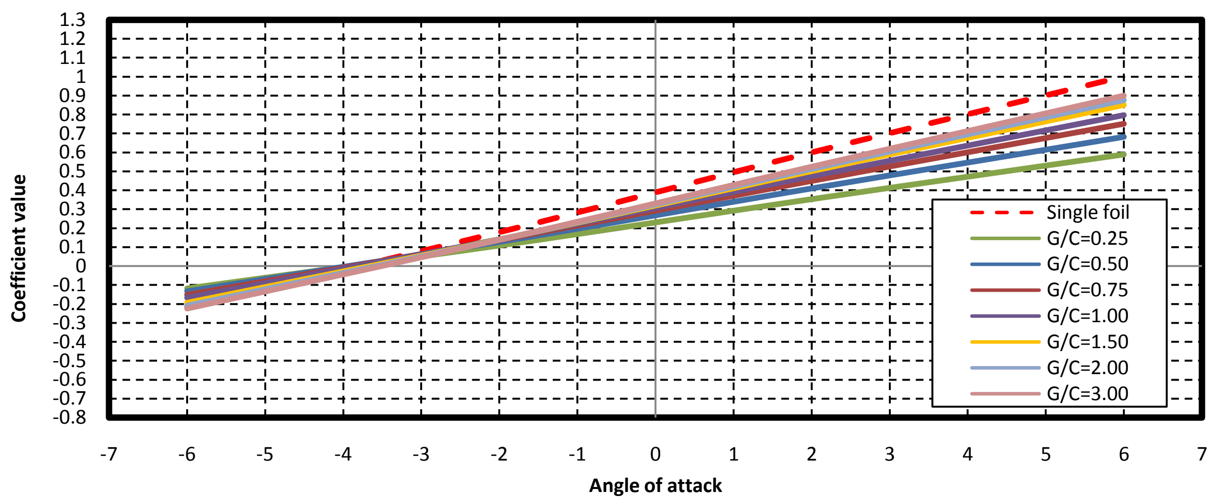

Figure 83. Lift Coefficient of cellule vs. angle of attack.

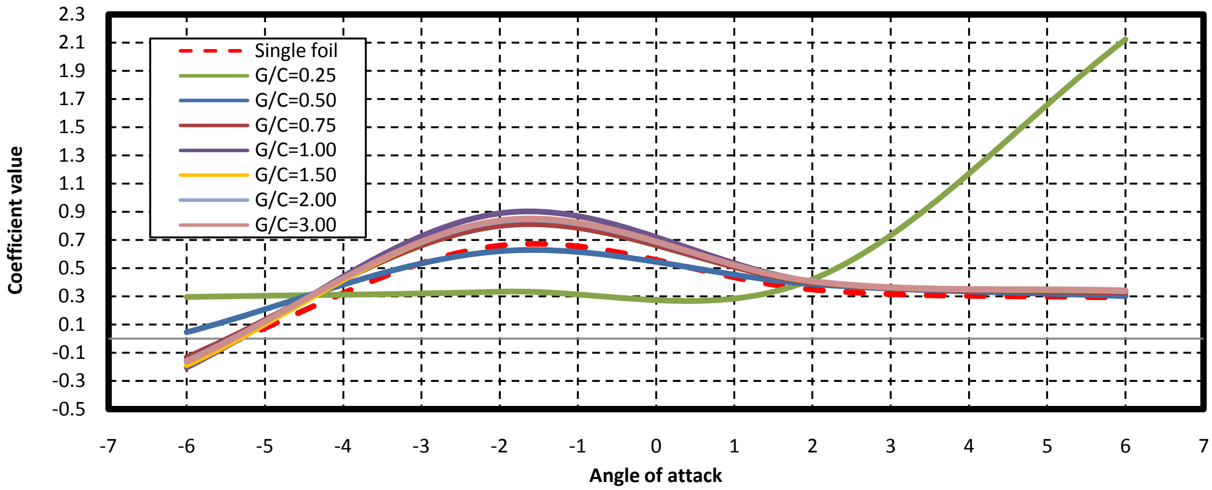

Figure 84. Moment Coefficient of upper foil vs. angle of attack.

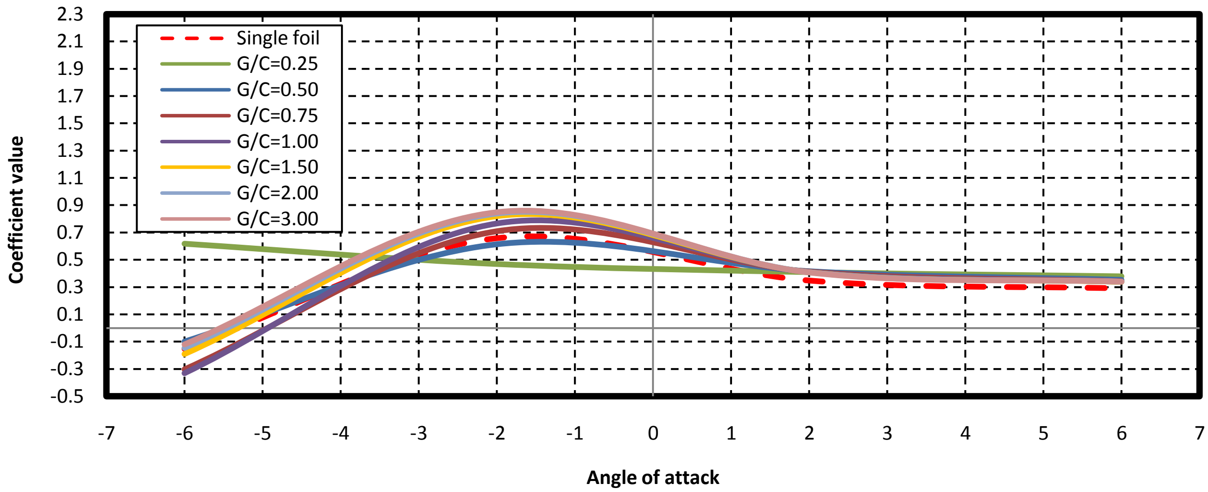

Figure 85. Moment Coefficient of lower foil vs. angle of attack.

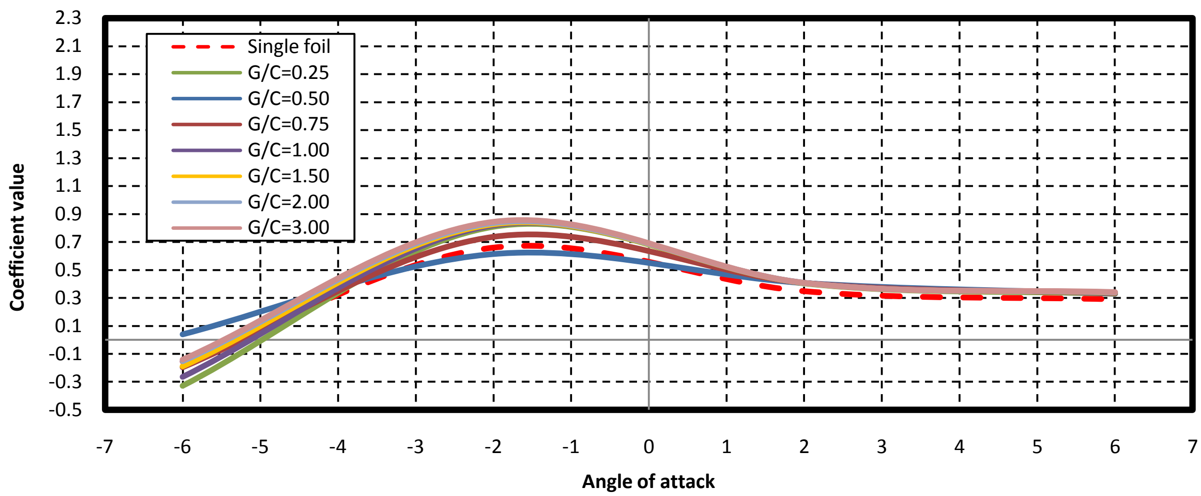

Figure 86. Moment Coefficient of cellule vs. angle of attack.

Chapter 7 - Analysis of two Sequential Foils

7.1. The Geometry of the Model

As performed in the previous chapter for vertically oriented foils, this chapter deals with the same Clark-Y section where two sequential foils are horizontally oriented. Five different cellules were examined in this case which is called stagger. The following table and figure describe the geometry of the model. The blue foil is fixed and represents the front (first) foil; the green foil is the rear (second) foil of each of the cellules:

Table 5. Stagger cellules that were examined.

case	**G**
1	100%
2	200%
3	300%
4	400%
5	500%

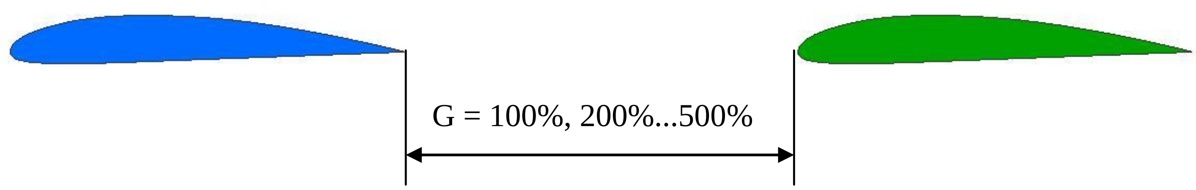

Figure 87. Stagger cellules that were examined.

7.2. Loading and Boundary Conditions

The boundary conditions and applied loads are the same as for the single foil, i.e. the FREE slip condition is imposed on each foil and the velocity upstream is unity. For each model of the 5 cellules described above, the pressure distribution curve was calculated for the first foil and for the second foil. For each model of the cellules, 4 different angles of attack were applied: -6°, -2°, +2° and +6°.

7.3. CFD Analysis and Results

No experimental results were found in the literature for sequential foils with the Clark-Y geometry. However, as was done in the previous chapter for the bi-plane case, the CFD model was of a cellule composed of 2 identical Clark-Y foils horizontally oriented.

The results were obtained for the first foil, second foil and the cellule for the lift and moment coefficients for each of the 4 angles of attack. Each of those 6 curves (per angle of attack) was plotted versus the chord space factor which is the gap between the vertical foils over the chord length, i.e. $\frac{G}{c}$. In addition, a summary of those 24 graphs (figures 98÷121) is given in 6 graphs (figures 122÷127) describing the lift and moment coefficients of first foil, second foil and the cellule. Those graphs include of all the 5 cellules together, are plotted versus the angle of attack. The moment coefficient is plotted with respect to the leading edge of the foil and not its middle, as performed in the previous chapter.

In addition to those 30 following figures, plotting the pressure distribution curves for both the first and second foils for the 4 different angles of attack is given. Each of those 8 graphs (figures 90÷97) contains all of the 5 different cellules together. For each of the 38 graphs, the results of the single foil under the same conditions are also given for easy and comfortable comparison.

The following figure demonstrates the meshed model of the stagger case when the gap between the foils is G = 100%. In addition, the velocity field at +6° is given as well in the second figure in order to show to the reader how clear is that view in ADINA. This case was chosen coincidentally.

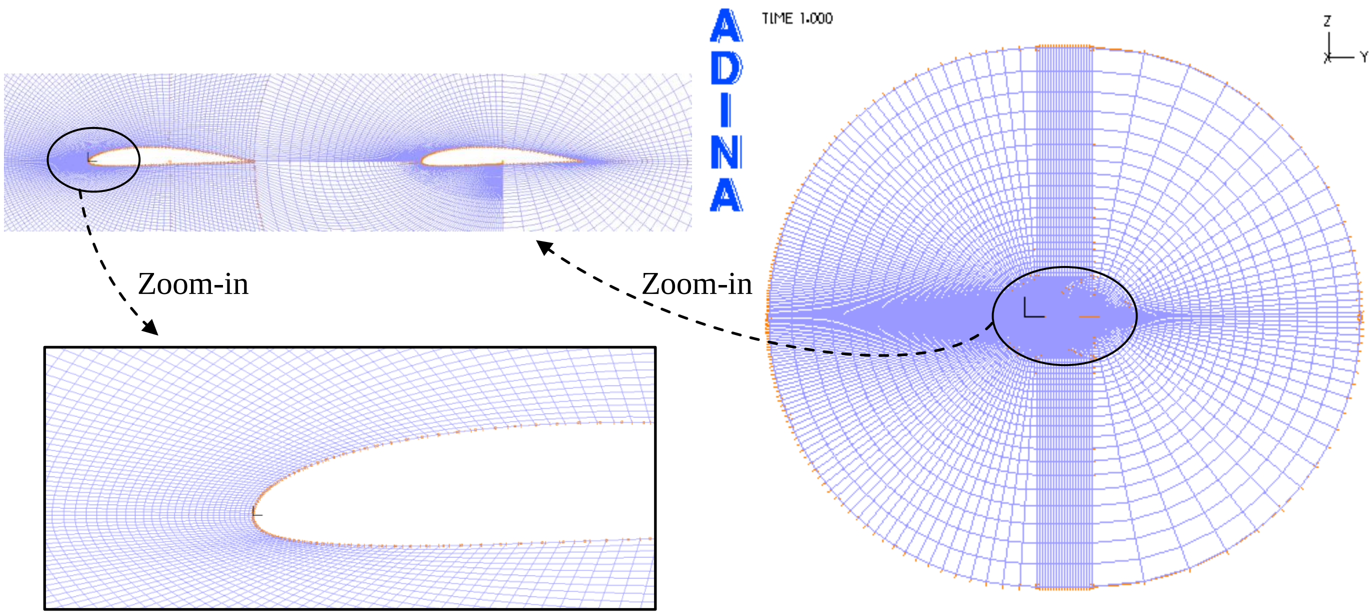

Figure 88. Stagger meshed model in ADINA for G=100%.

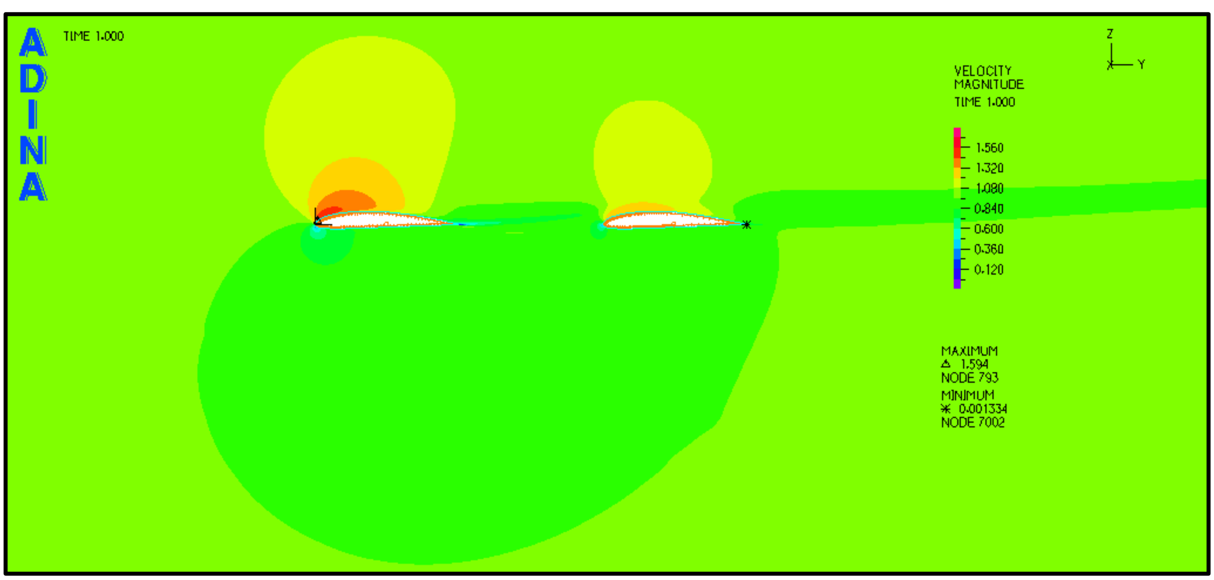

Figure 89. Stagger velocity field in ADINA for G=100% at +6°.

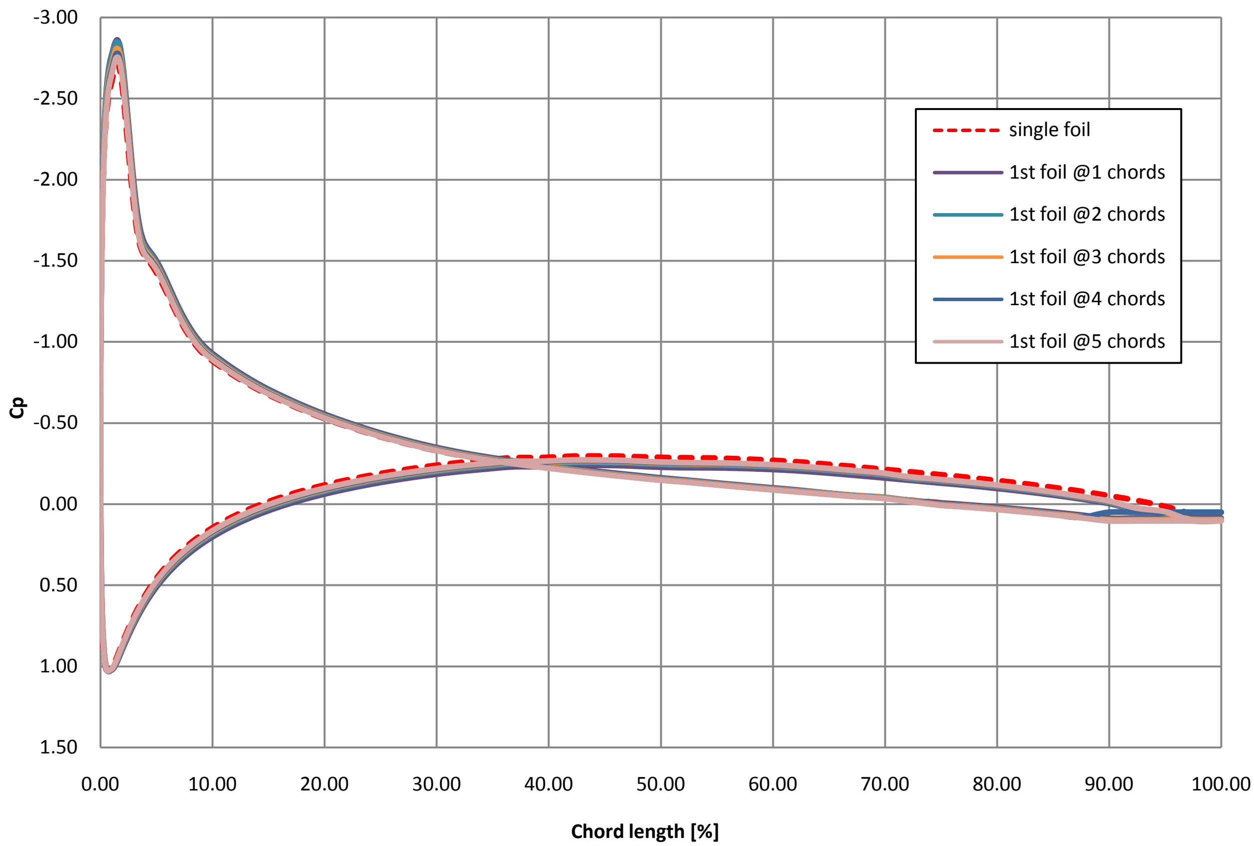

Figure 90. Pressure distribution curve of first foil at -6°.

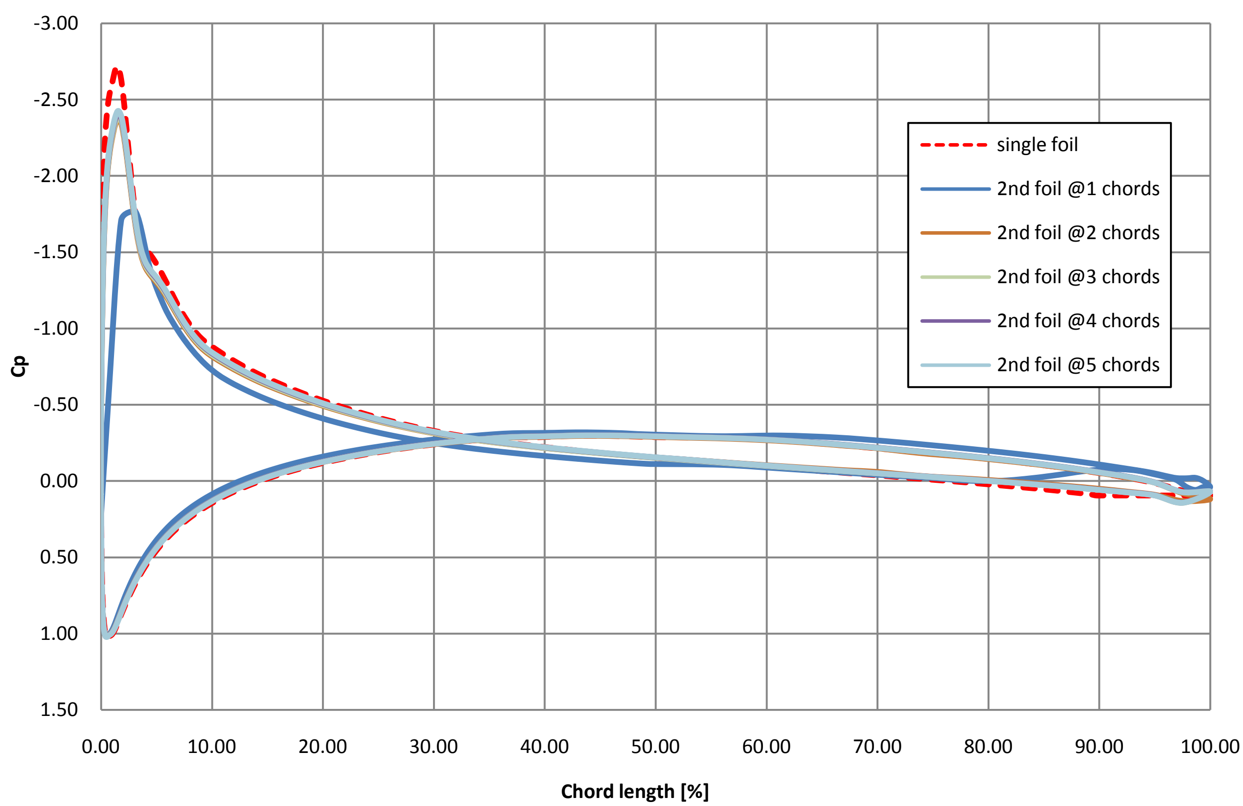

Figure 91. Pressure distribution curve of second foil at -6°.

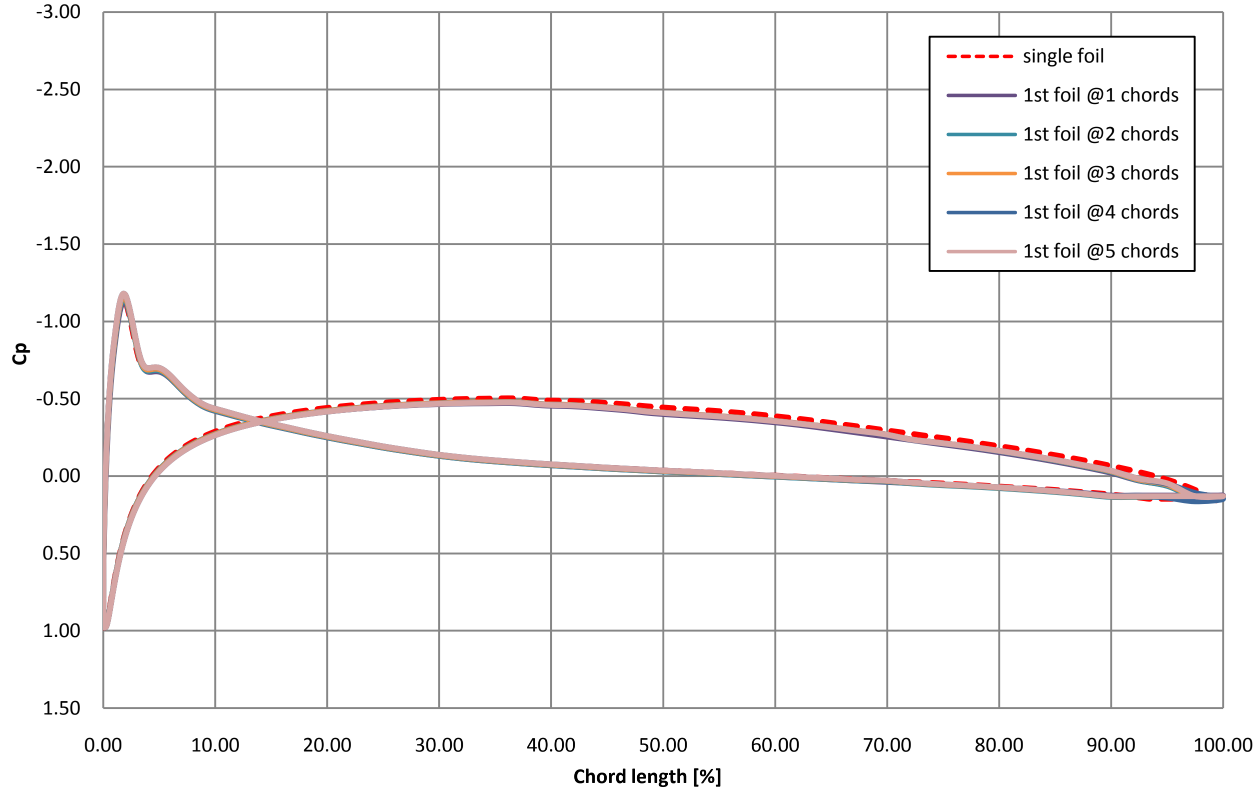

Figure 92. Pressure distribution curve of first foil at -2°.

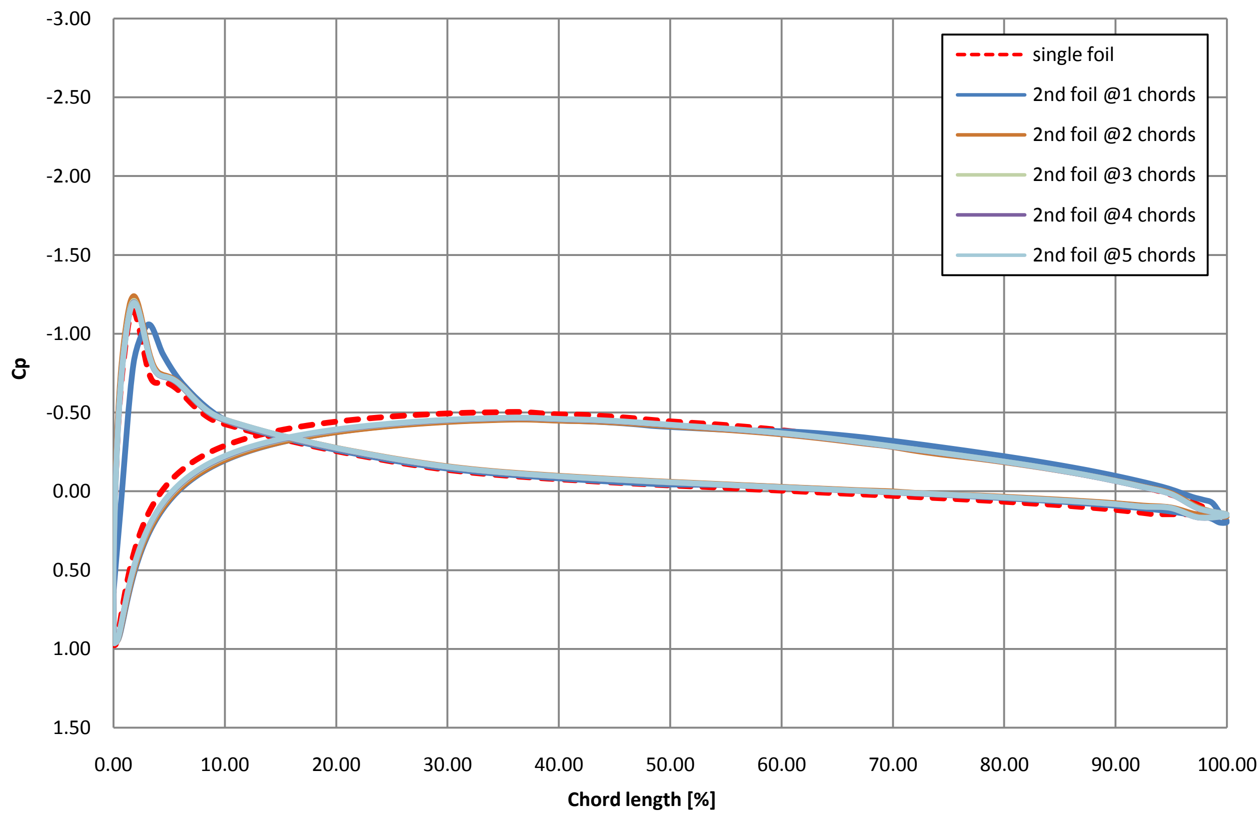

Figure 93. Pressure distribution curve of second foil at -2°.

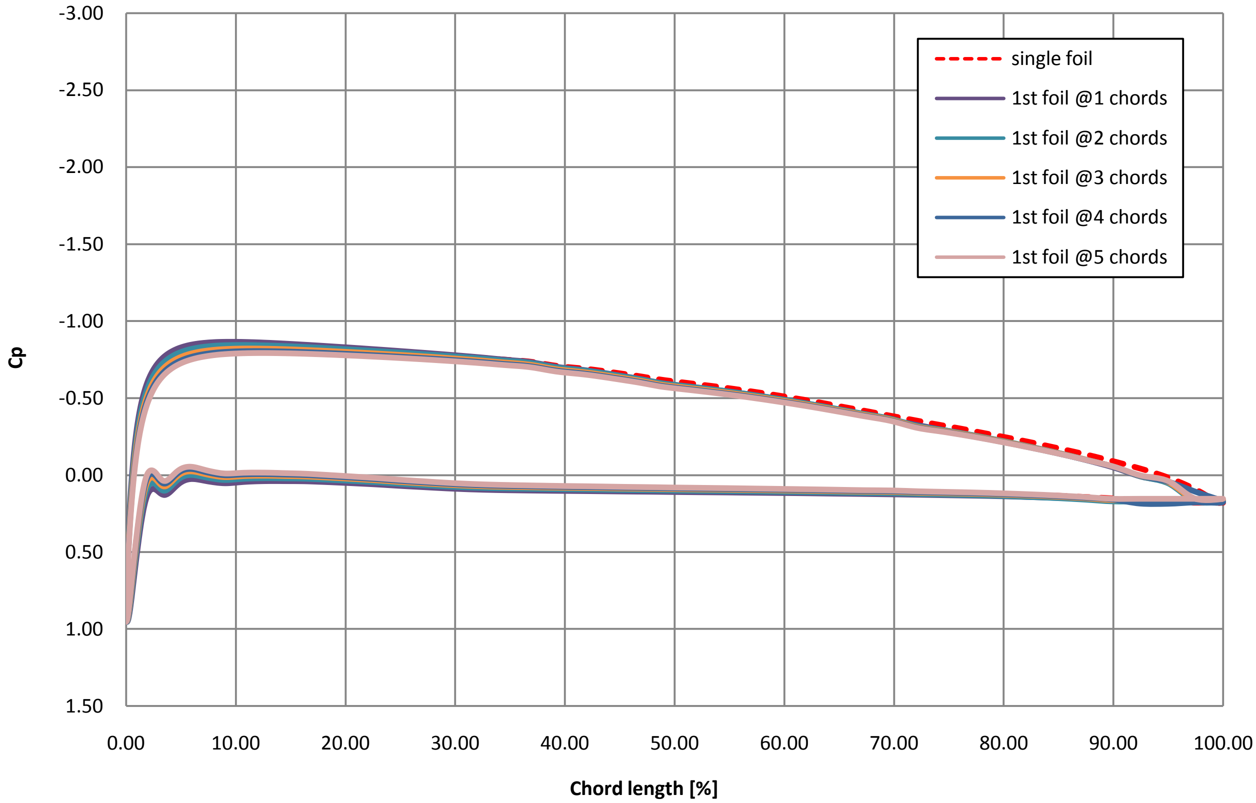

Figure 94. Pressure distribution curve of first foil at +2°.

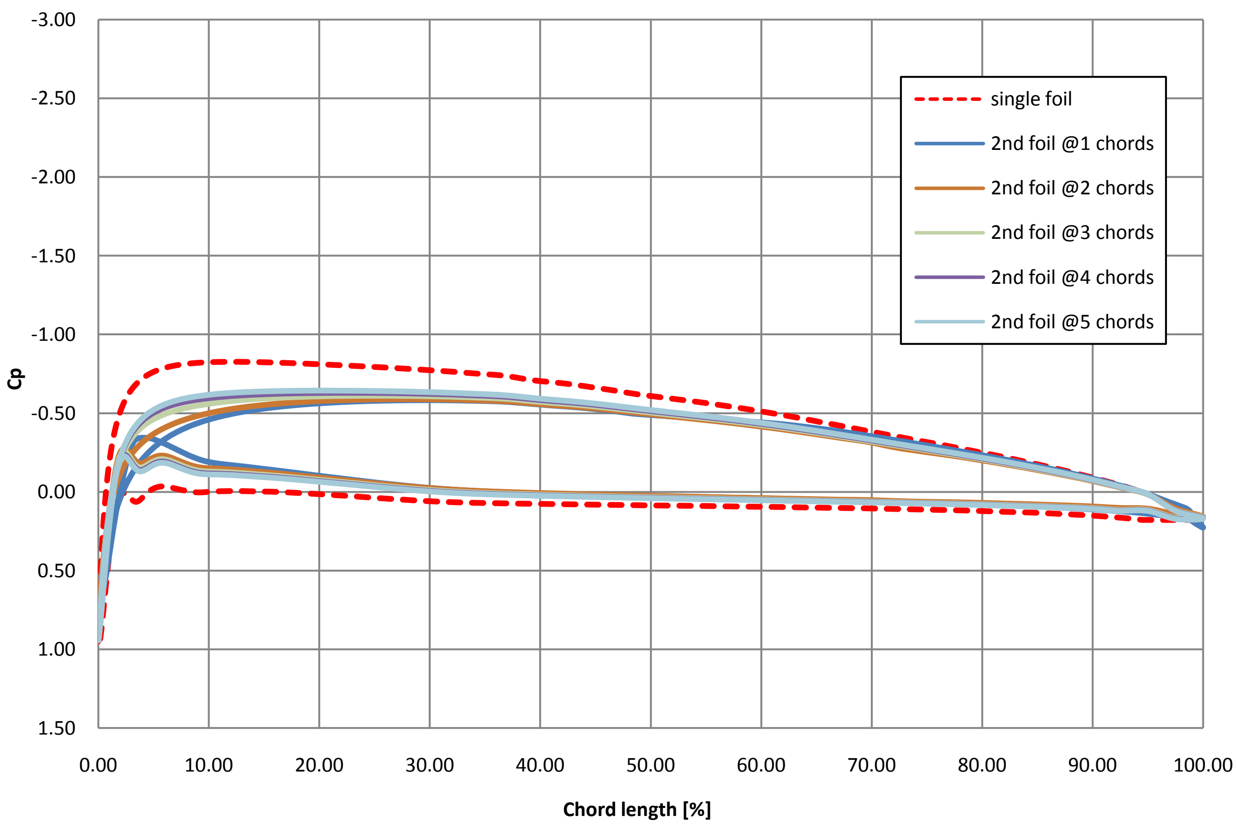

Figure 95. Pressure distribution curve of second foil at +2°.

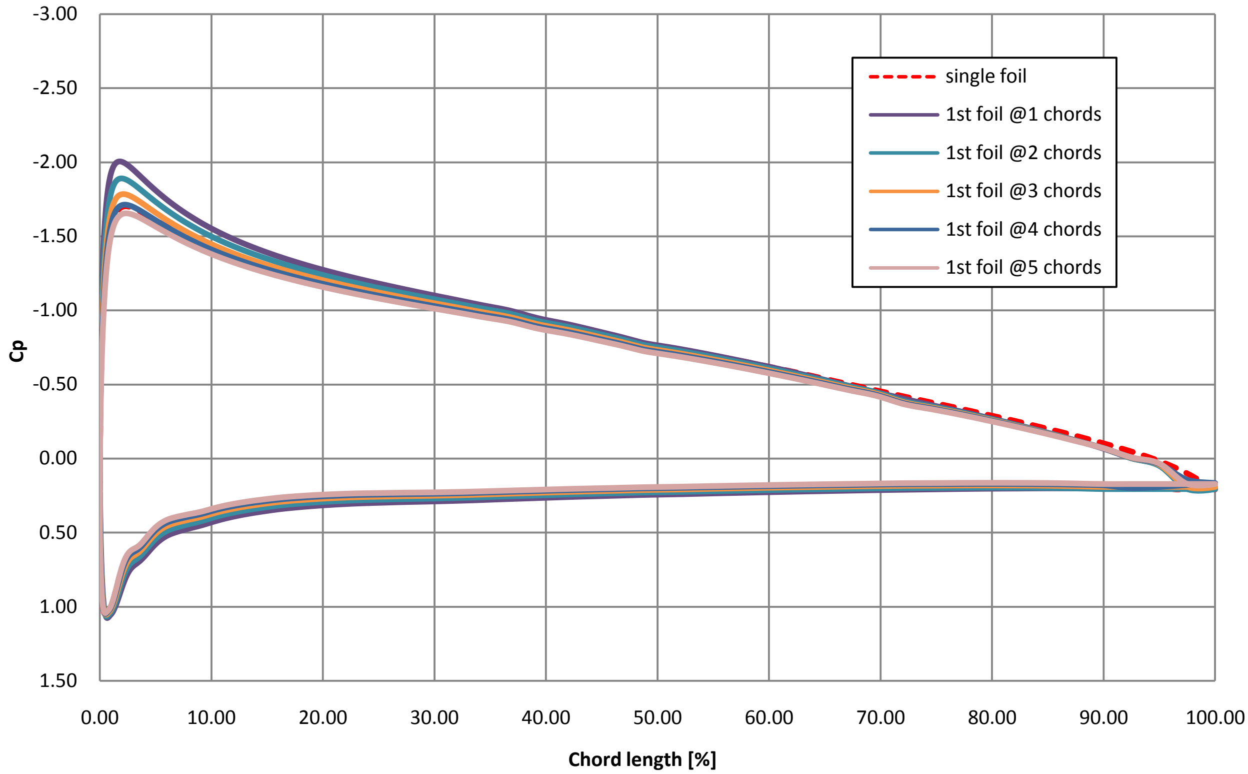

Figure 96. Pressure distribution curve of first foil at +6°.

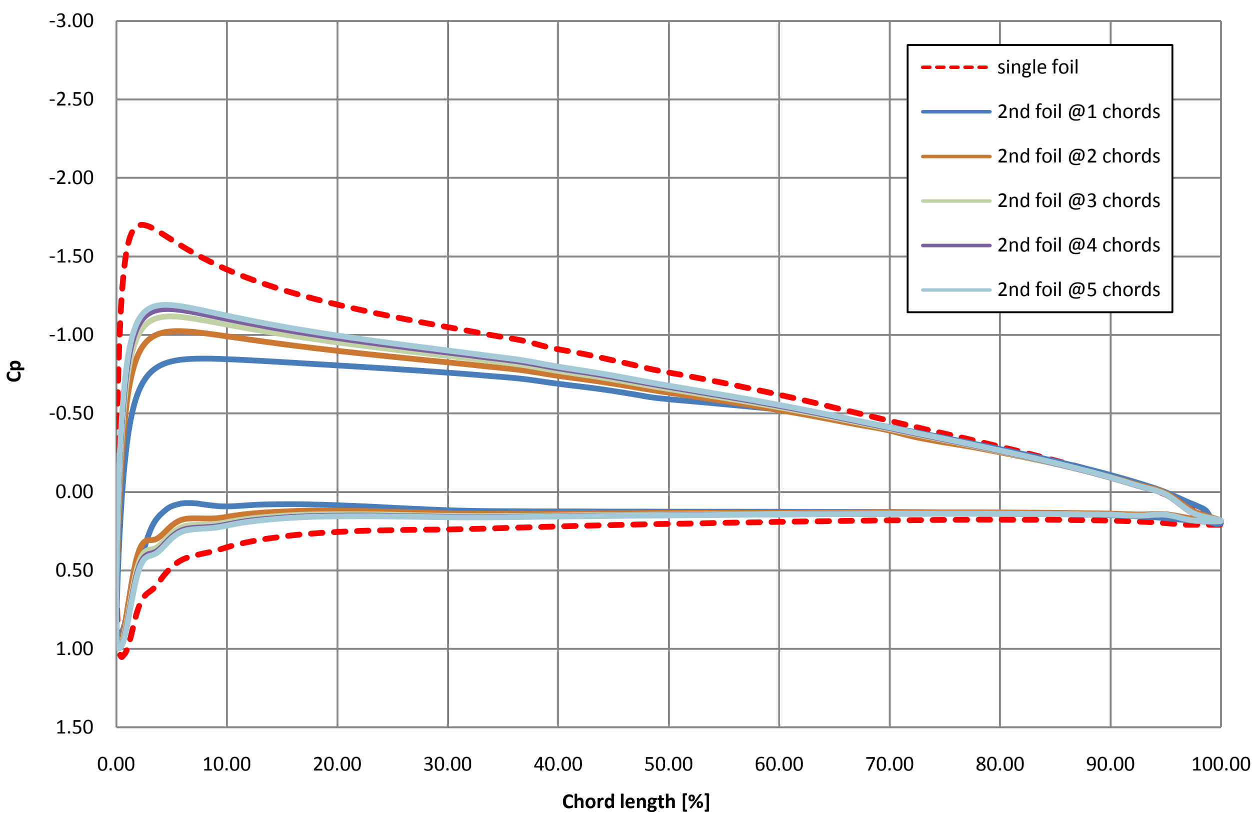

Figure 97. Pressure distribution curve of second foil at +6°.

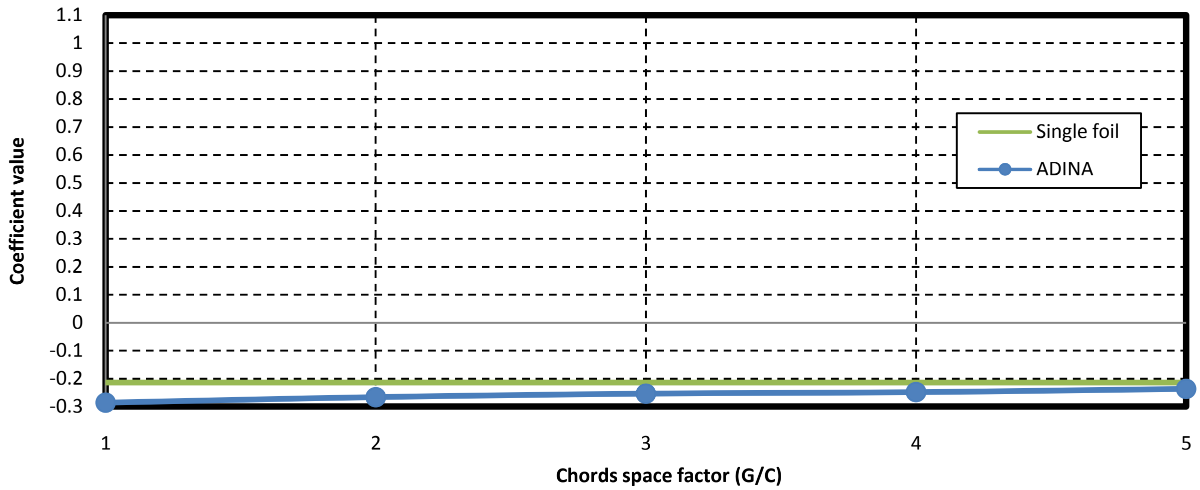

Figure 98. Lift Coefficient of upper foil at -6°.

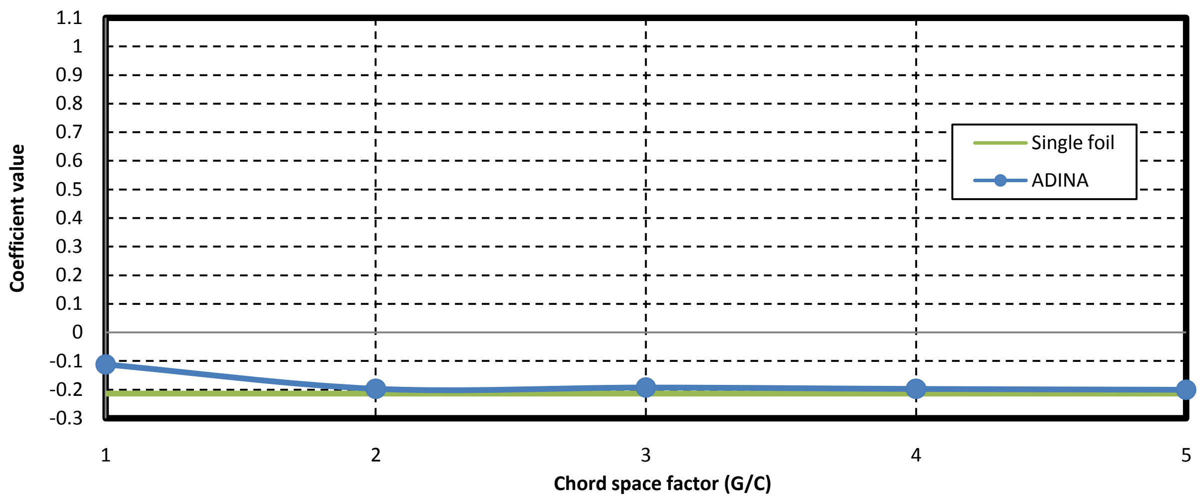

Figure 99. Lift Coefficient of second foil at -6°.

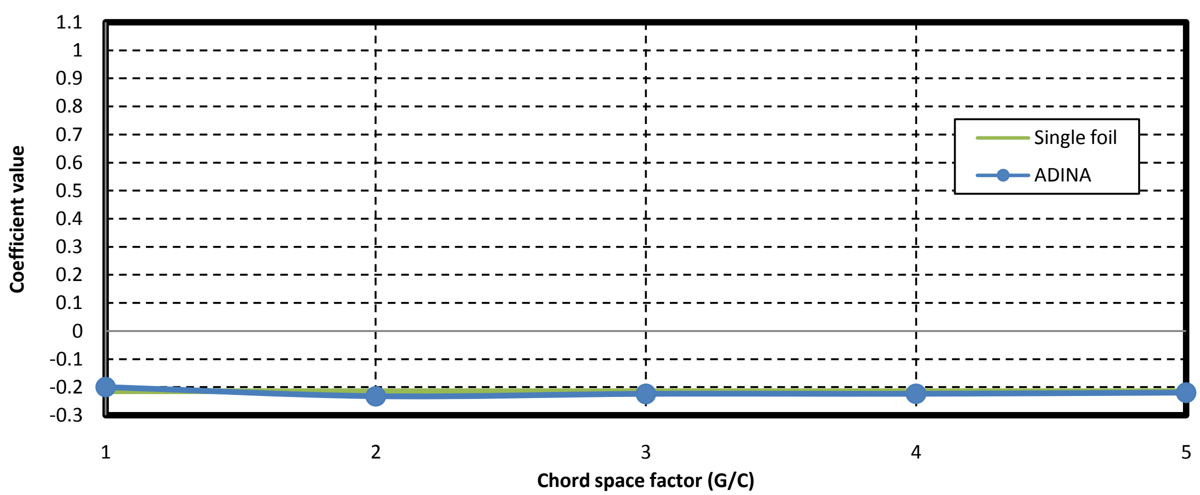

Figure 100. Lift Coefficient of cellule at -6°.

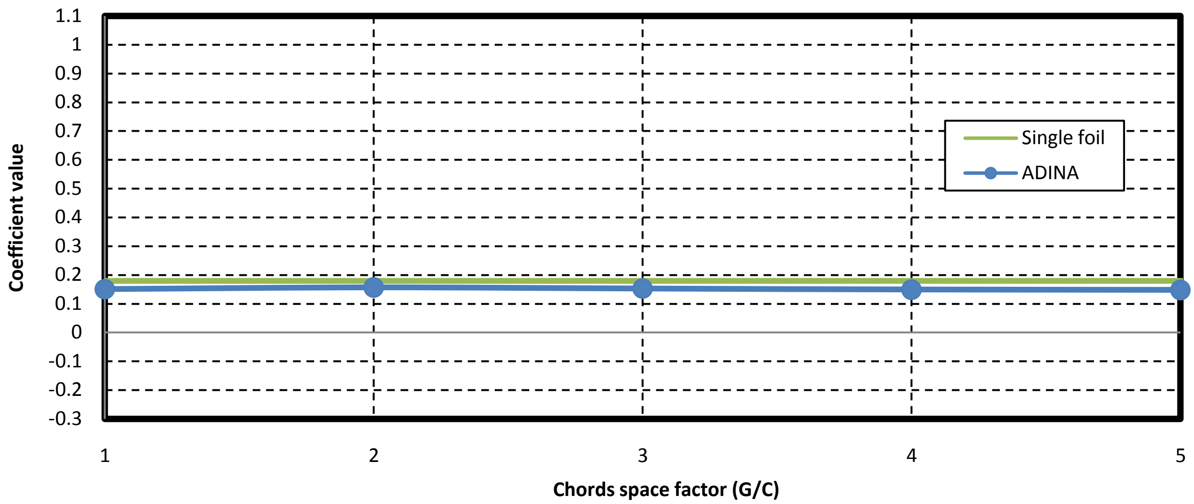

Figure 101. Lift Coefficient of first foil at -2°.

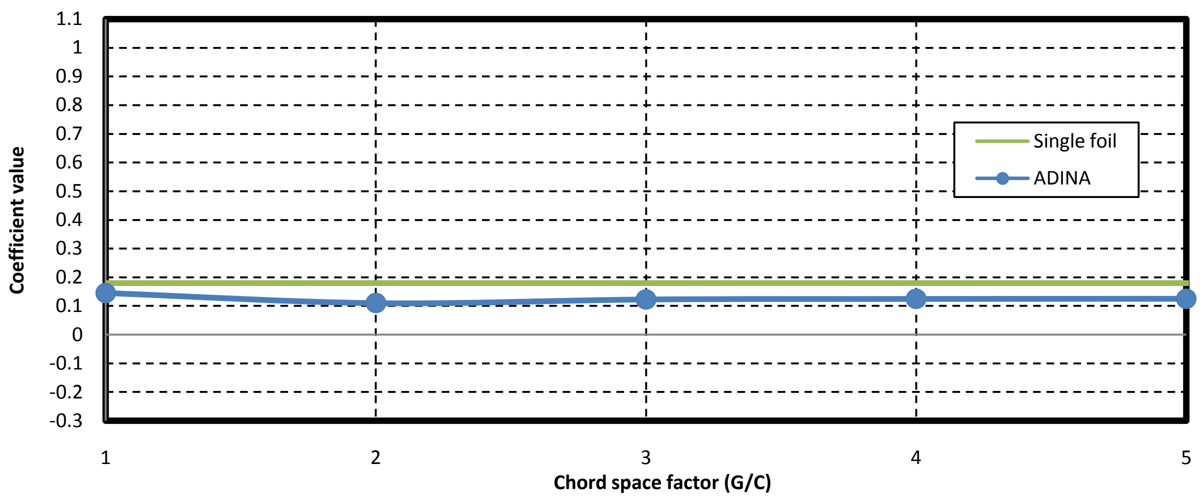

Figure 102. Lift Coefficient of second foil at -2°.

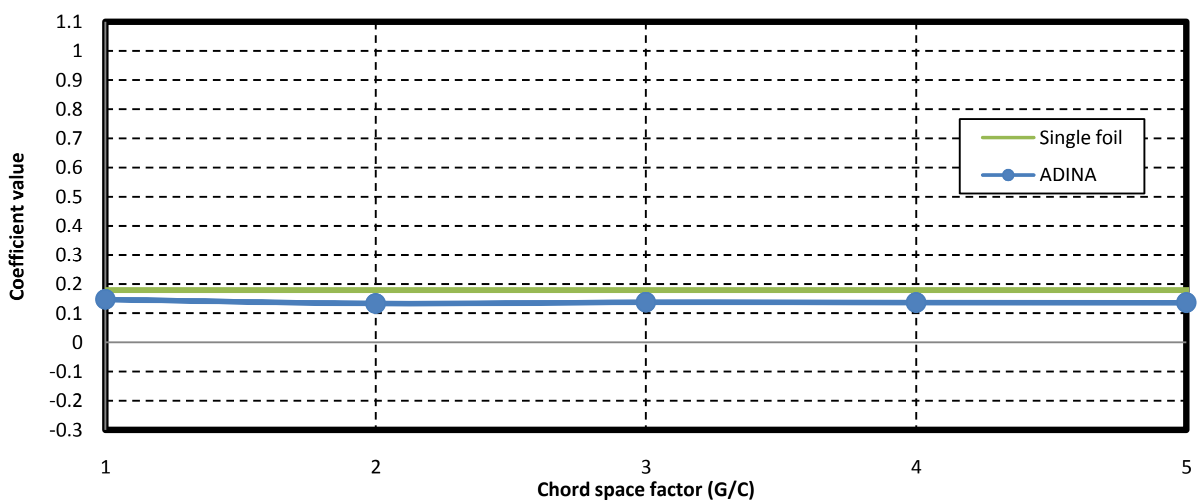

Figure 103. Lift Coefficient of cellule at -2°.

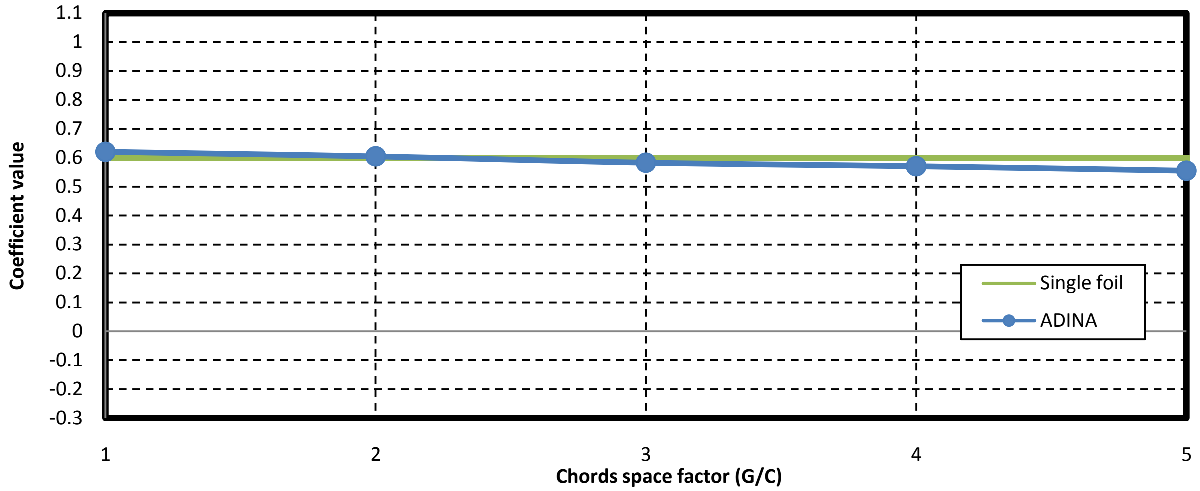

Figure 104. Lift Coefficient of first foil at +2°.

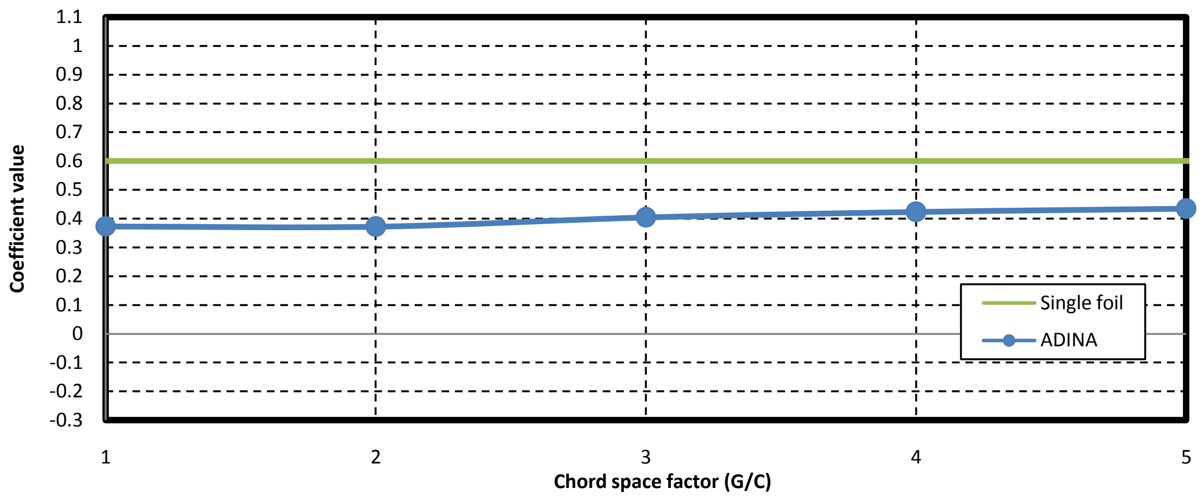

Figure 105. Lift Coefficient of second foil at +2°.

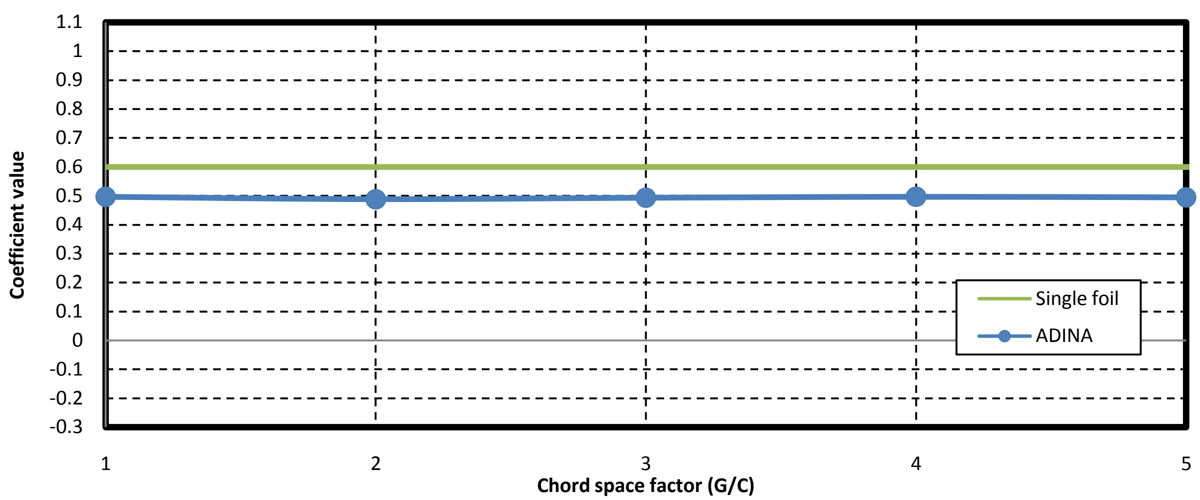

Figure 106. Lift Coefficient of cellule at +2°.

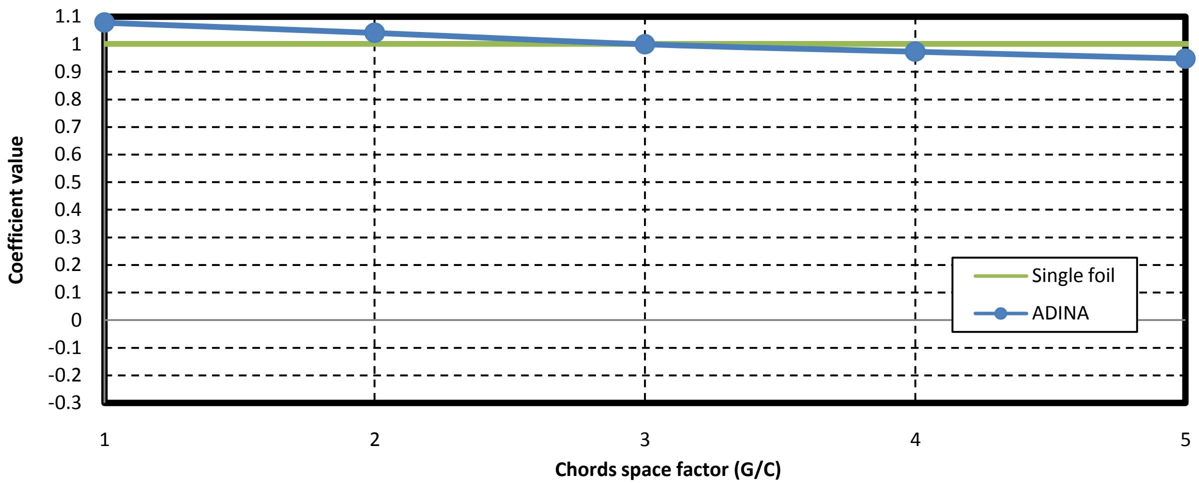

Figure 107. Lift Coefficient of first foil at +6°.

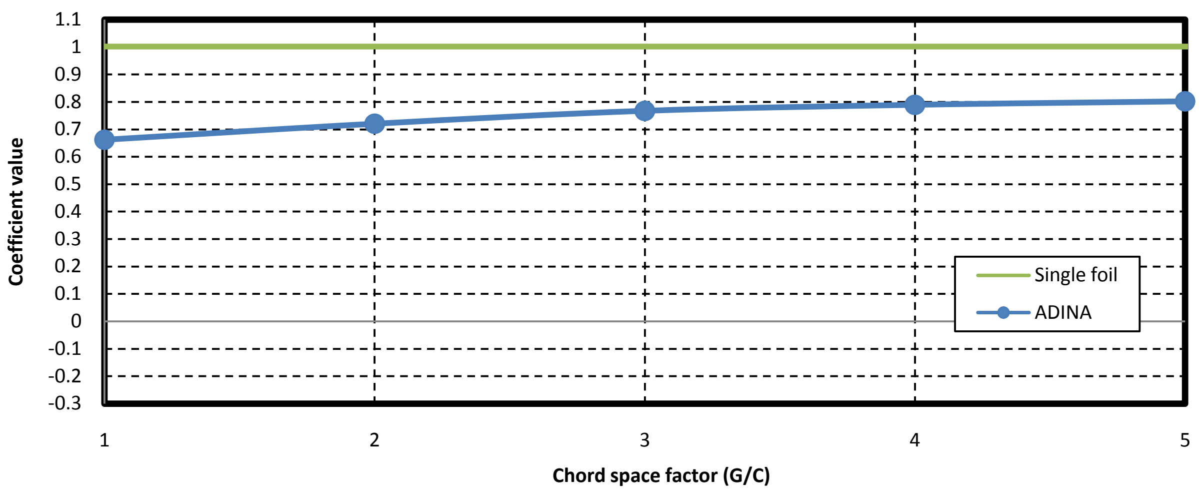

Figure 108. Lift Coefficient of second foil at +6°.

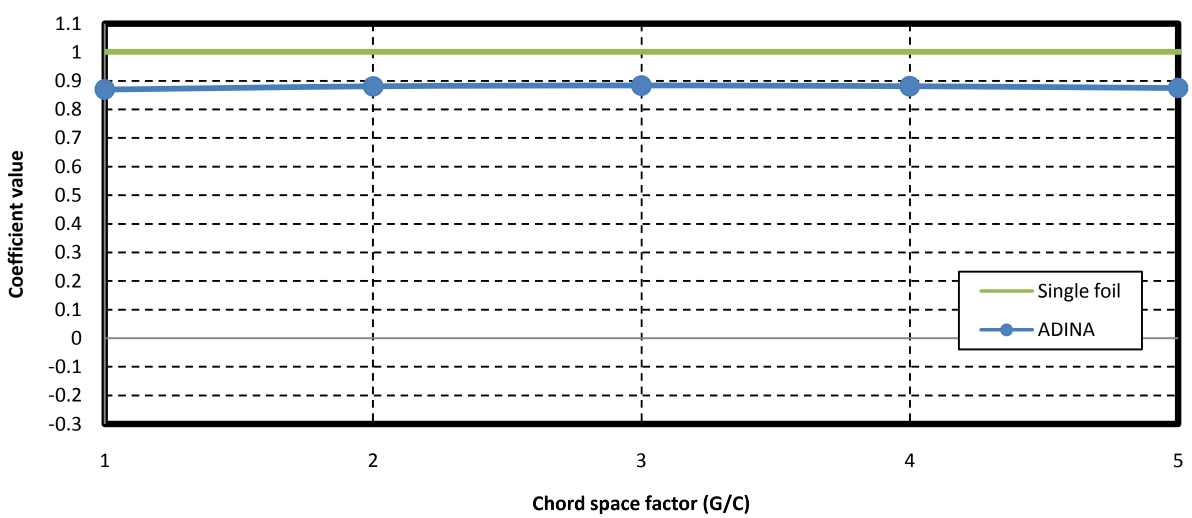

Figure 109. Lift Coefficient of cellule at +6°.

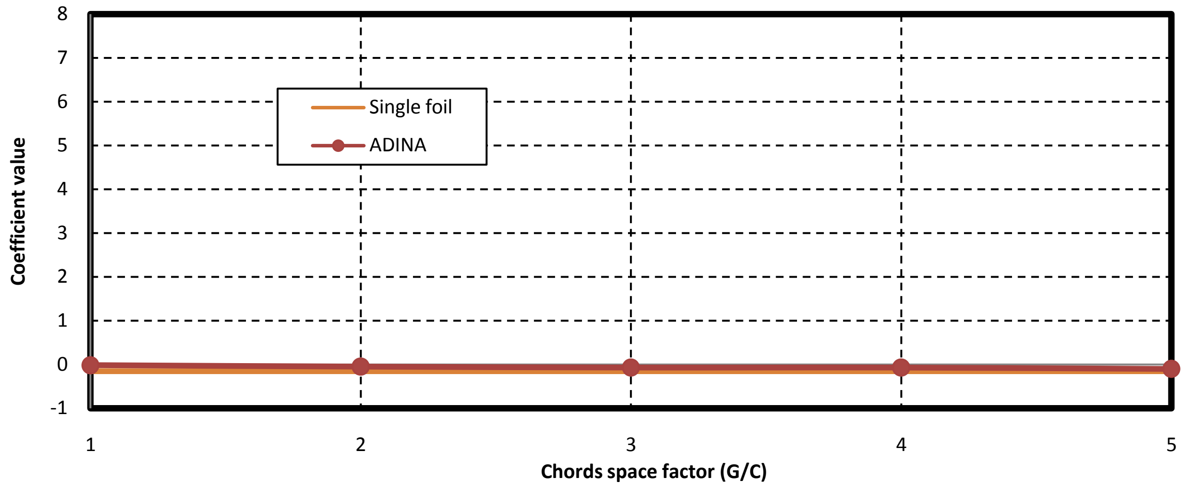

Figure 110. Moment Coefficient of first foil at -6°.

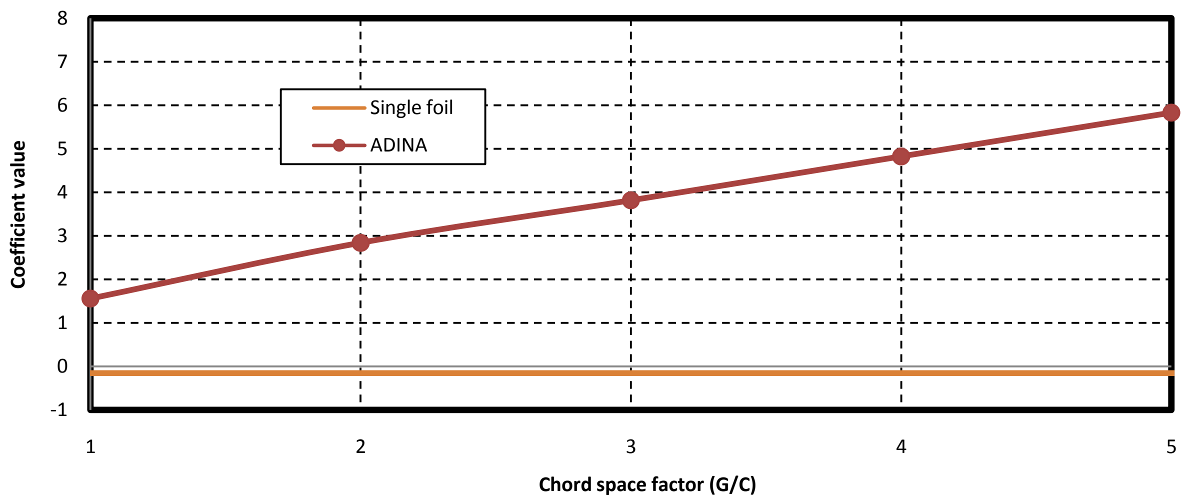

Figure 111. Moment Coefficient of second foil at -6°.

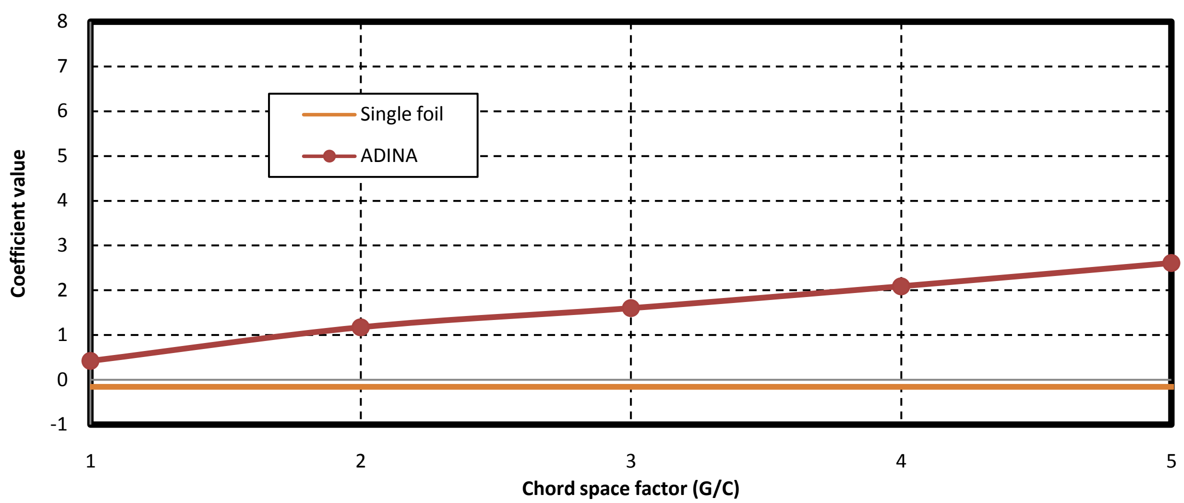

Figure 112. Moment Coefficient of cellule at -6°.

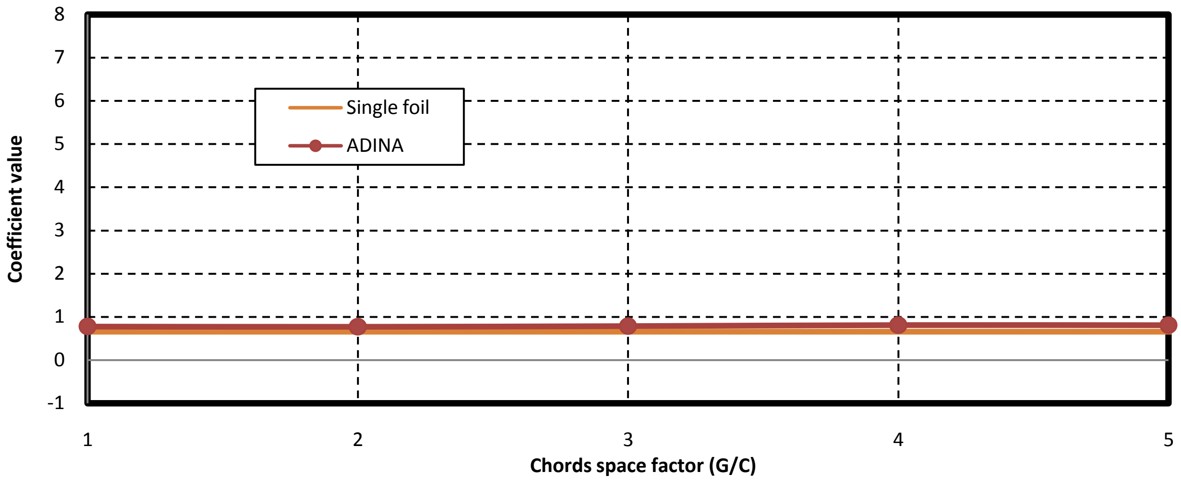

Figure 113. Moment Coefficient of first foil at -2°.

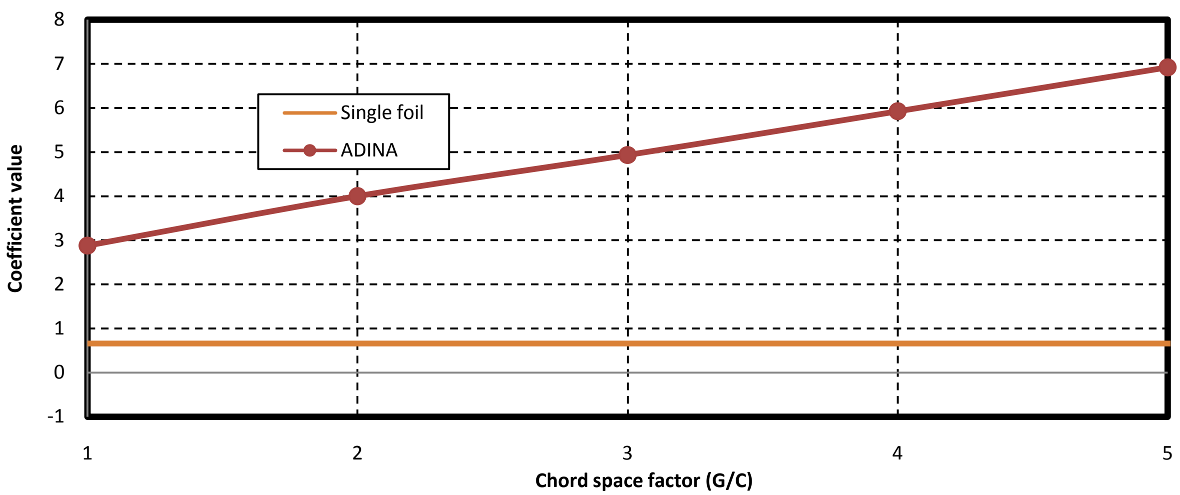

Figure 114. Moment Coefficient of second foil at -2°.

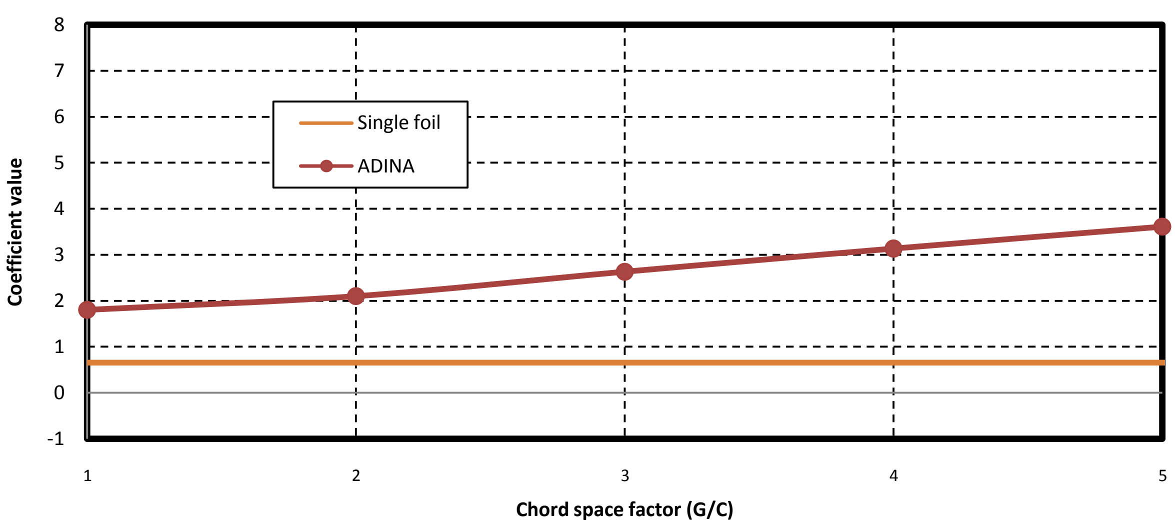

Figure 115. Moment Coefficient of cellule at -2°.

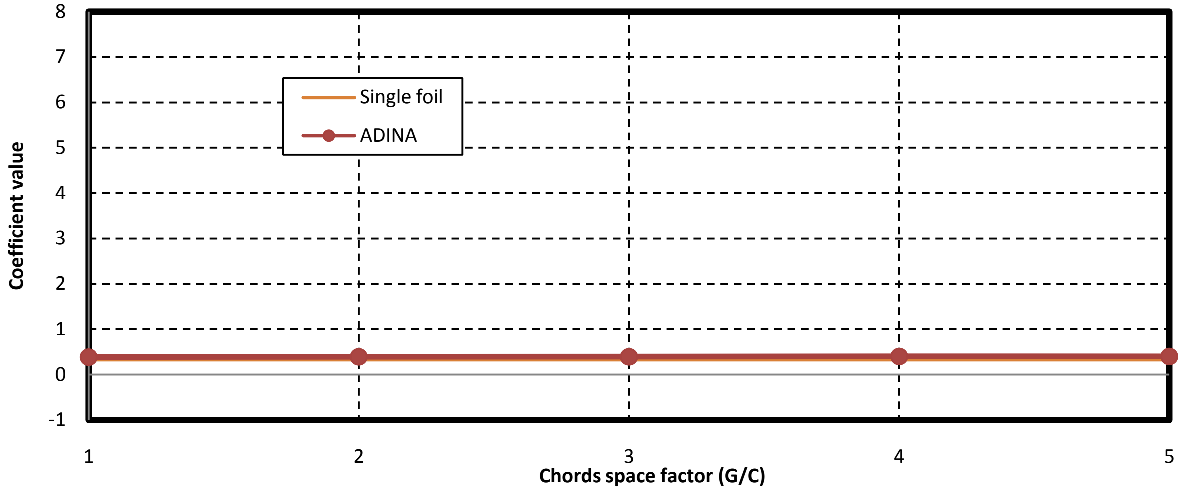

Figure 116. Moment Coefficient of first foil at +2°.

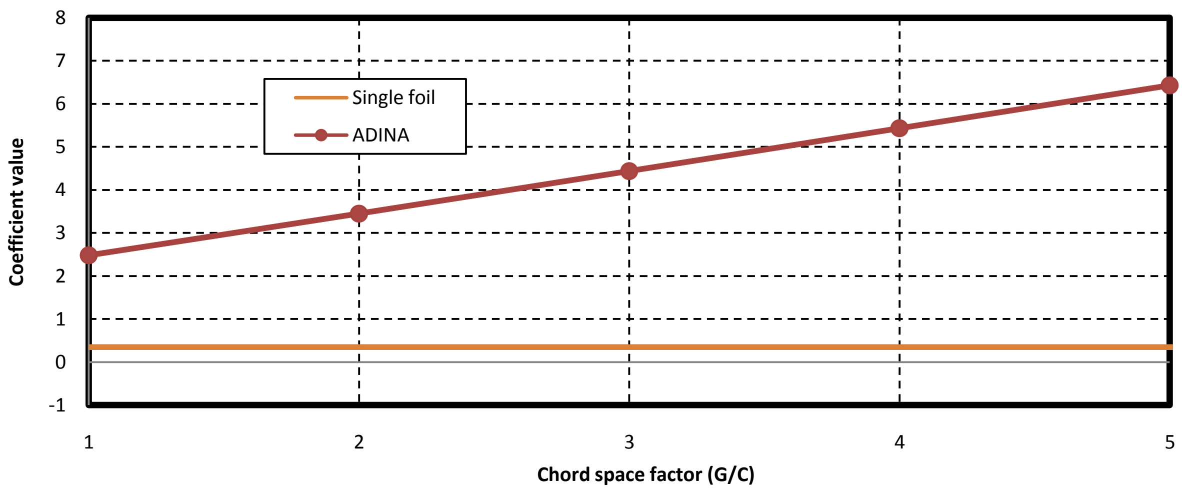

Figure 117. Moment Coefficient of second foil at +2°.

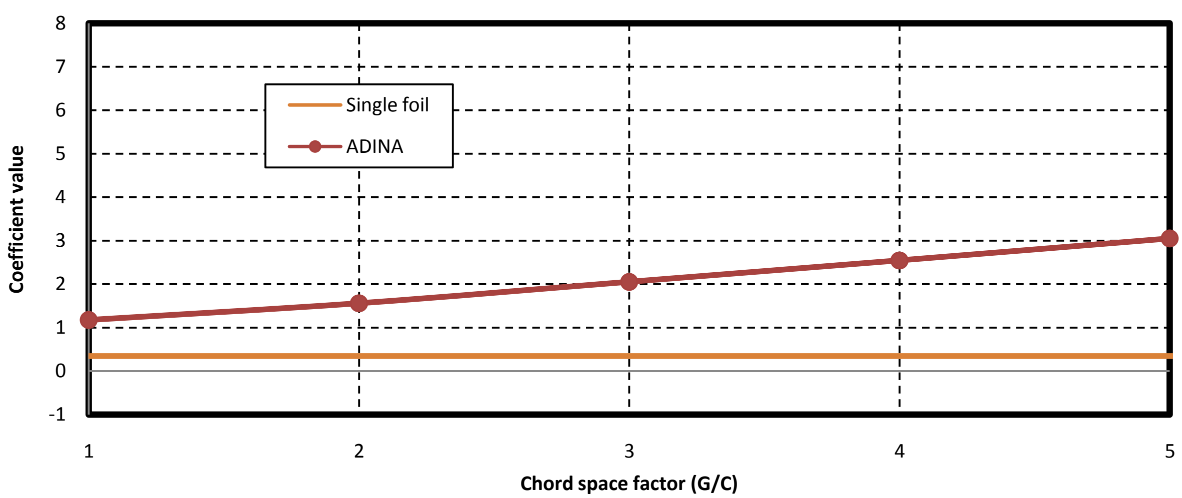

Figure 118. Moment Coefficient of cellule at +2°.

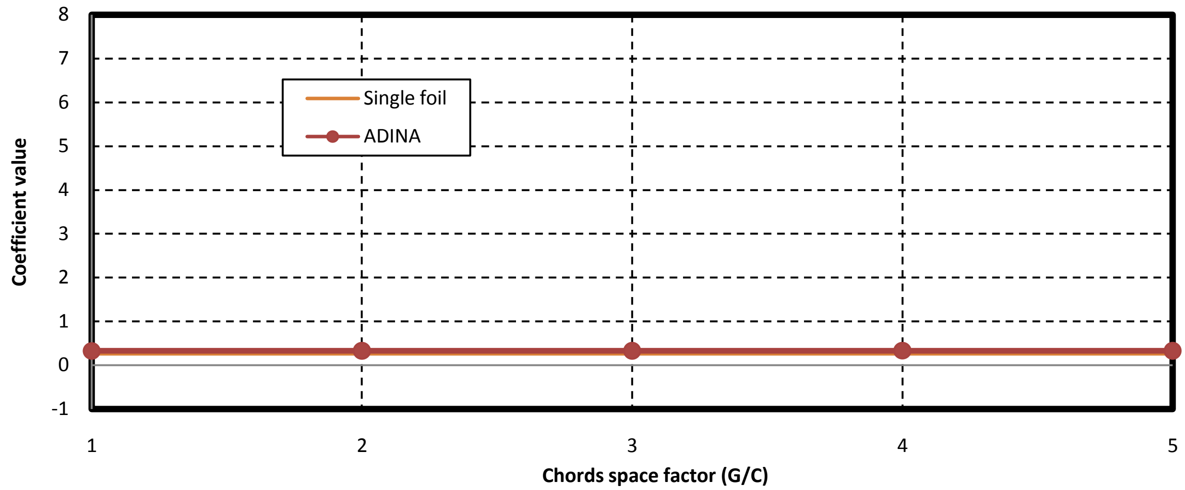

Figure 119. Moment Coefficient of first foil at +6°.

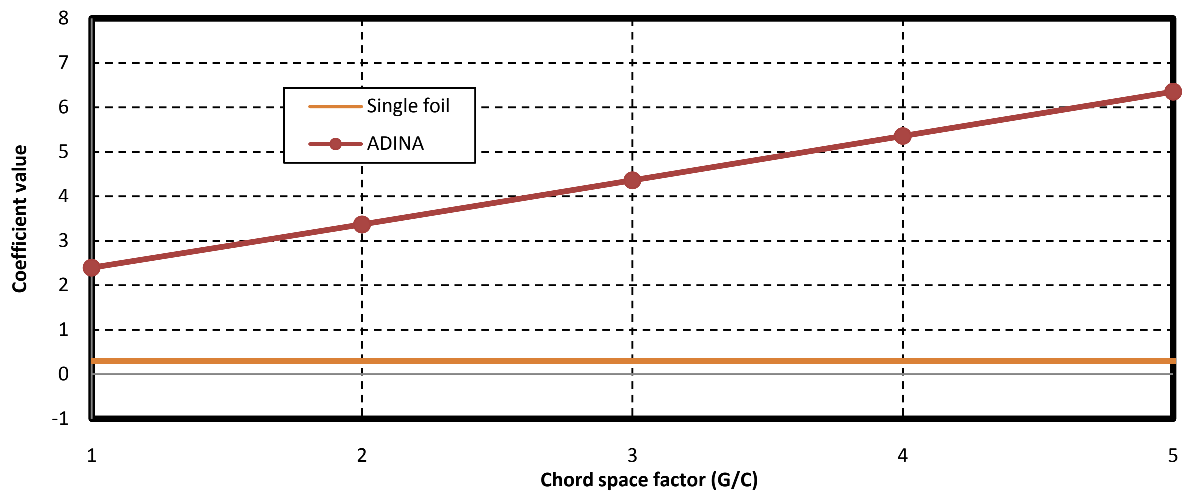

Figure 120. Moment Coefficient of second foil at +6°.

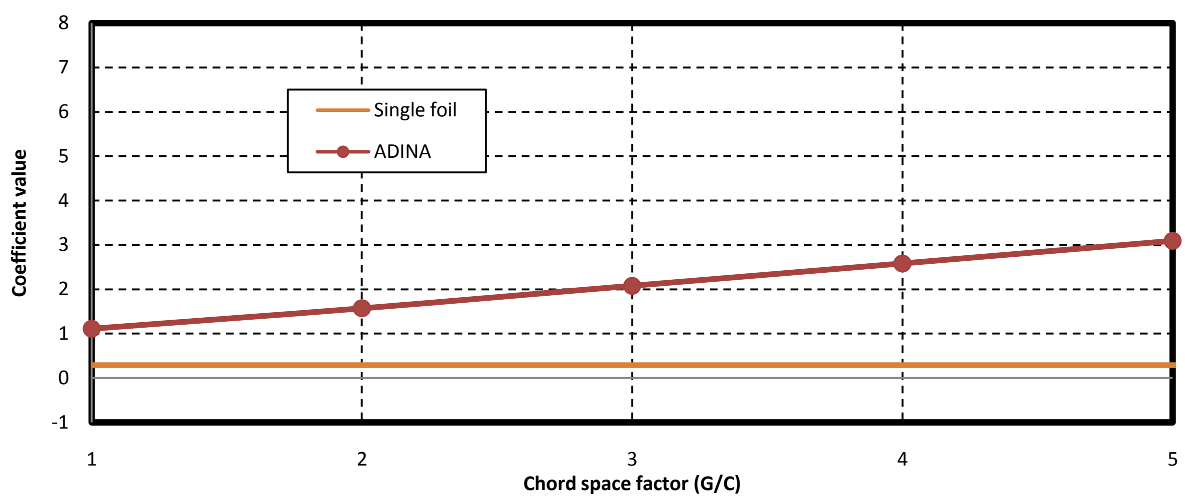

Figure 121. Moment Coefficient of cellule at +6°.

7.4. Discussion of the Results

The prominent observation that can be made out of the results in the graphs above is that the general behavior of the curves for both the first and second foils makes sense since they tend towards the values of the single foil when they are far away from each other and their reciprocal disturbance is gone. Although there are no experiments to make comparison with, the results are reliable and trustworthy. The CFD models were studied by using the bands tool as explained in chapter 4 for verifying the finite element process, which assures the reliability of the process.

Looking carefully at the pressure distribution curves (figures 90÷97), it is easy to notice that for the second foil when G=100%, the curve is smaller than for a single foil when the angle of attack is negative (-6° or -2°) and for all G's for a positive angle of attack, the pressure distribution curve gets wider and wider as the gap between the foils, i.e. $\frac{G}{c}$, gets bigger but still does not reach the single foil curve. The reason for that is that the flow that passes the first foil leaves the foil tangent to its tail as the Kutta condition is fulfilled. Due to that, the flow direction over the second foil is not derived only from the angle of attack of the cellule (the 2 foils together) but also affected by the geometry of the tail of the first foil. In addition, because the first foil changes the flow that passes it, the flow that gets to the second foil can no longer be considered uniform. Consequently, at positive angles of attack where the lift is significant, the second foil experiences chaotic flow over it and cannot contribute lift as the first foil does. As the gap between the foils gets bigger, the lift gained from the second foil gets bigger as also can be seen from the graph describing the lift coefficient behavior (figures 98÷109). However, at negative angles of attack, the lift balances out with the negative angle of attack and the foil camber, thus one gets a smaller pressure distribution curve for the second foil at G=100%. In addition, because of this balancing out, when the gap between the 2 foils increases (G>100%), the influence of the first foil over the second foil decreases and this is why the pressure distribution curves are almost the same for the second foil at negative angles of attack for G>100%.

Another interesting finding from the graph (figure 96) is that for the first foil at +6°, the pressure distribution curve is higher than for a single foil. As the gap between the foils gets smaller, the pressure distribution curve of the first foil gets bigger than the single foil. That evidence makes sense since the second foil, which sits behind, builds higher pressure at the tail of the first foil and because of that all the pressure distribution curves of the first foil get higher. Thus, the lift of the first foil at +6° is higher than for a single foil. That could also be verified by observing the lift coefficient curve (figure 107) of the first foil at that angle of attack.

Observing the moment coefficient curve (figures 110÷121), one can notice that the first foil has almost the same curve as the single foil does. However, the second foil moment coefficient curve is much higher than for a single foil. Furthermore, as the distance between the foils gets bigger, the moment coefficient gets bigger as well. The reason for that is the moment coefficient is calculated with respect to the leading edge of the first foil. Thus, the lever arm of the second foil gets bigger as the foil gets far from the first foil. Along with the increase of the lever arm, the moment coefficient of the second foils increases as well. This is valid for the cellule moment coefficient as well. According to formula (64), the cellule moment coefficient is combined by both of the moment coefficients of the foils. Because of the high moment coefficient of the second foil, the moment coefficient of the cellule is much higher than for a single foil. One should notice that this stands in contradiction to the bi-plane case where both of the foils had the same lever arm for all the cellules.

In order to understand the above results better, it is wise to plot the lift and moment coefficients of the first foil, second foil and the cellule versus the angle of attack, as performed for the bi-plane case. These 6 graphs (figures 122÷127) are given below. In those graphs, it is easy to notice the different behavior of the moment coefficient of the first foil, second foil and the cellule compared with the single foil moment coefficient.

According to those graphs, the lift of the first foil is approximately equal to that of a single foil but since the lift of the second foil is small, the cellule lift is lower than that of a single foil. This conclusion was obtained for the bi-plane as well.

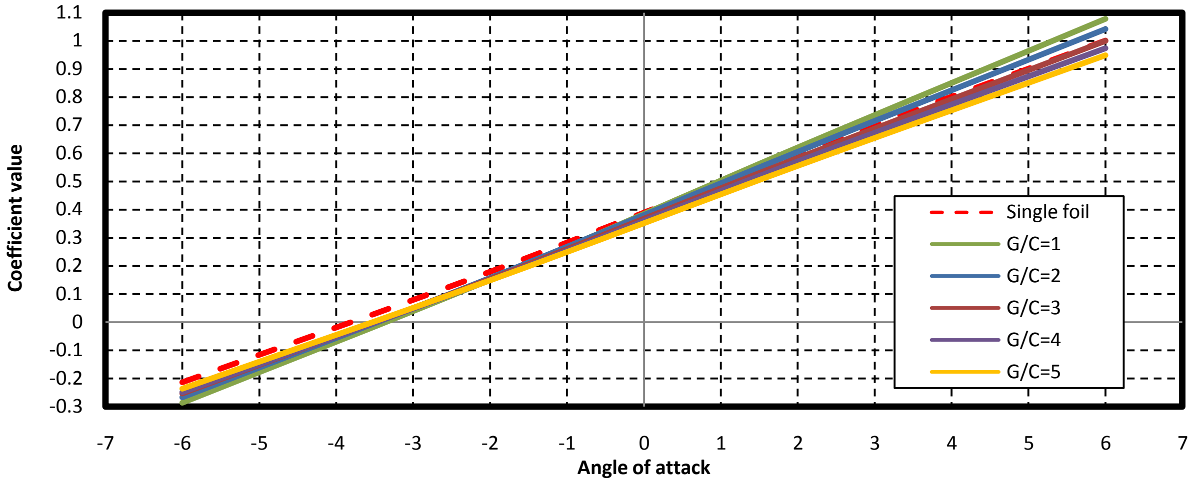

Figure 122. Lift Coefficient of first foil vs. angle of attack.

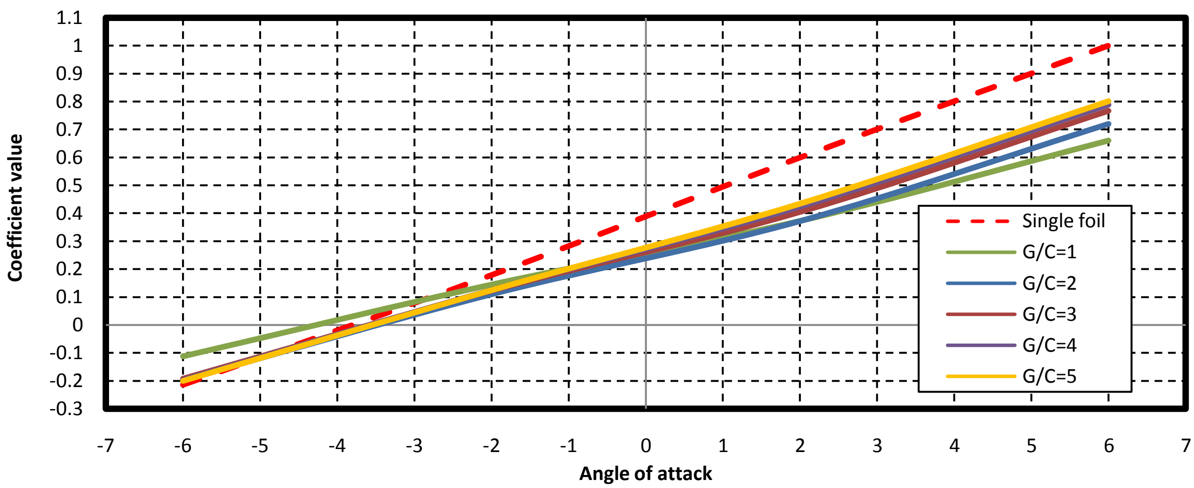

Figure 123. Lift Coefficient of second foil vs. angle of attack.

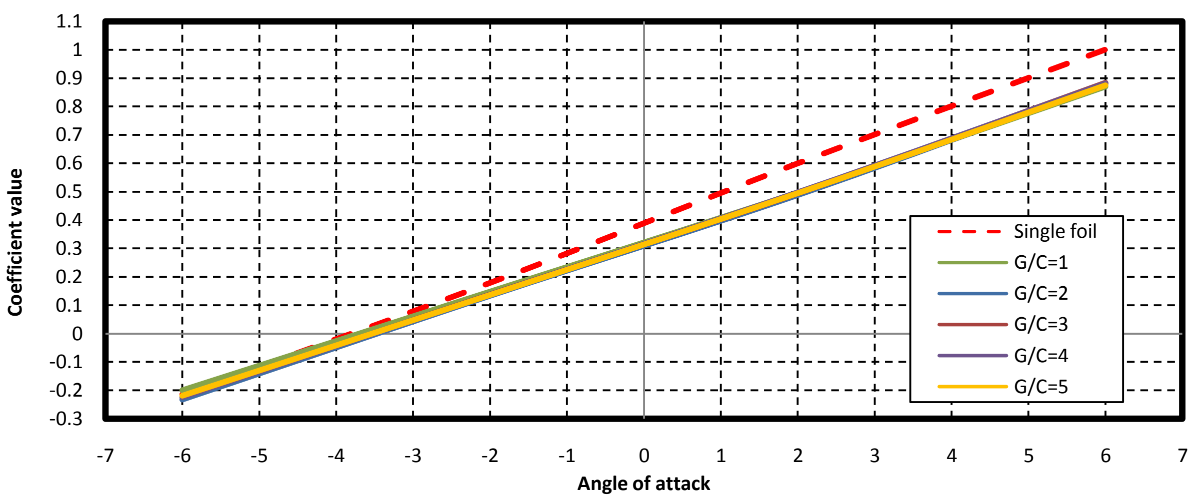

Figure 124. Lift Coefficient of cellule vs. angle of attack.

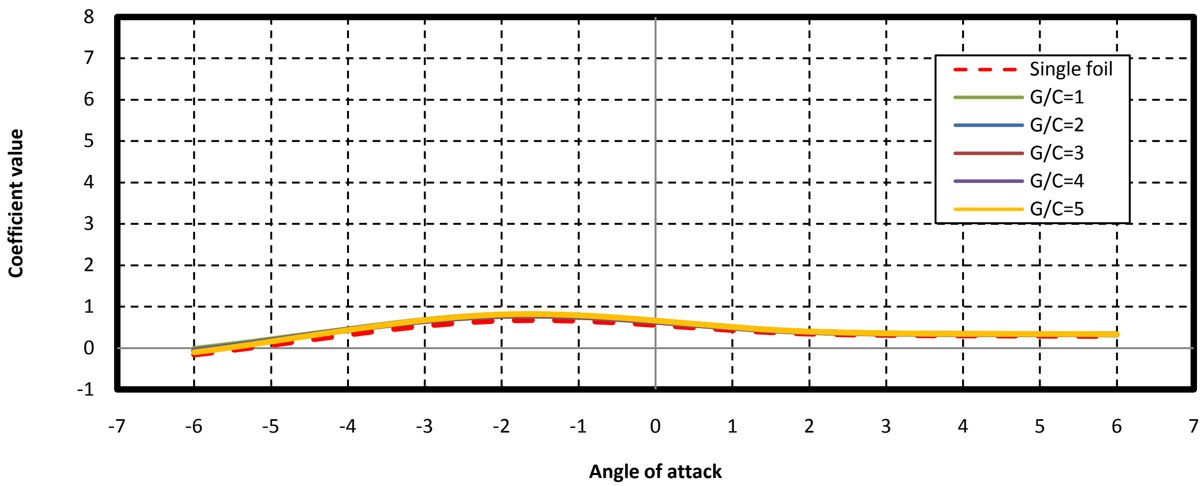

Figure 125. Moment Coefficient of first foil vs. angle of attack.

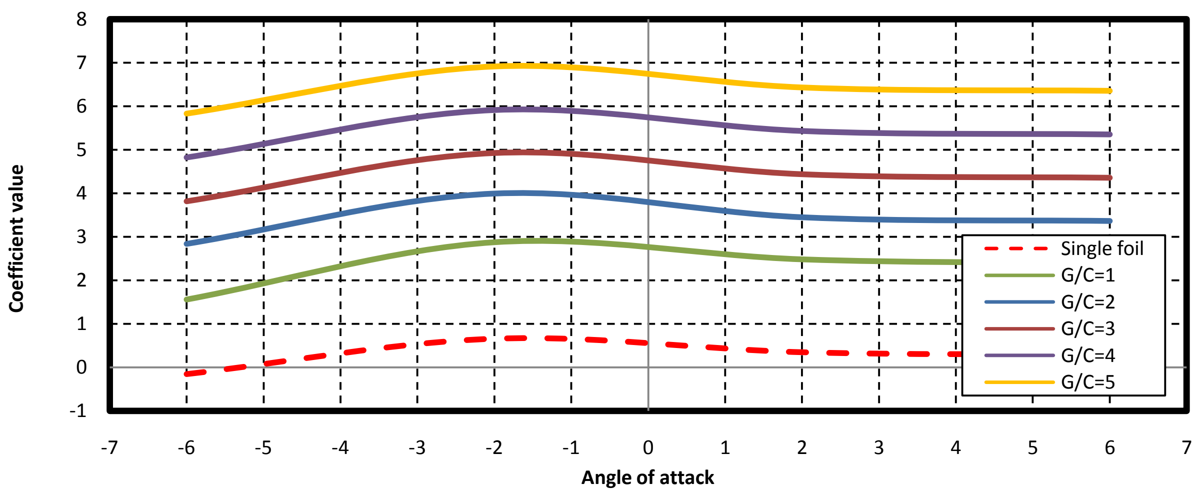

Figure 126. Moment Coefficient of second foil vs. angle of attack.

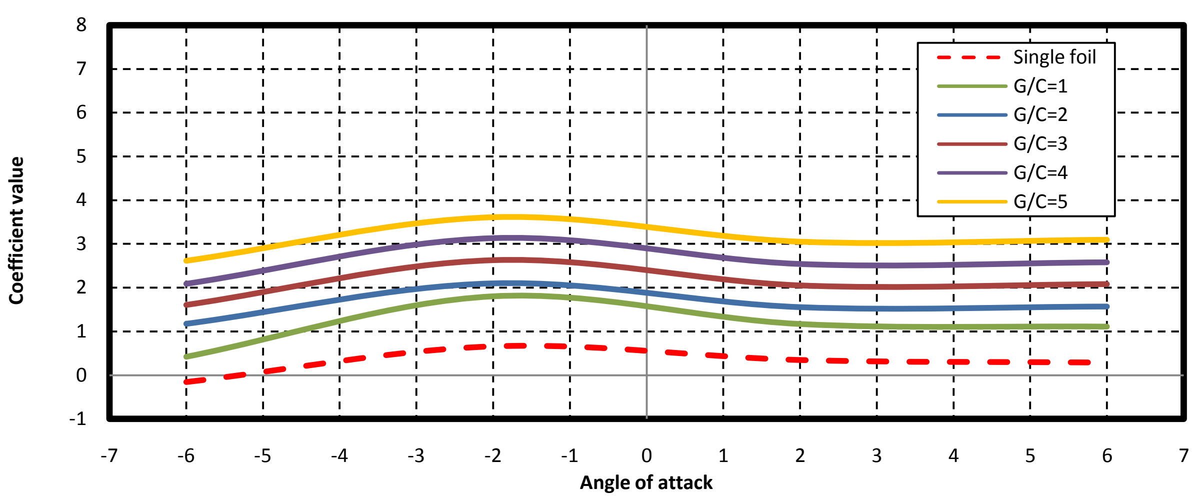

Figure 127. Moment Coefficient of cellule vs. angle of attack.

Chapter 8 - Summary and Concluding Remarks

The main goal of this research was to explore and investigate the reciprocal influence between two foils, one on each other and as a whole as a cellule, when placed vertically and horizontally. This objective is the focus of a bigger process of lowering significantly the drag of a ship when hydrofoils are attached to its hull. The research results were obtained and based on CFD analyses using the ADINA software. In addition, the CFD results were compared with analytical solutions and experimental results where those were available. The analytical process is well detailed and can be easily followed by the reader.

The first step was to solve the flow field around a single foil where the chosen foil was the Clark-Y foil. Observing the pressure distribution at the leading edge discovered a problem with the section geometry. Looking for different references only strengthens that finding and led to using the Unigraphics software in order to correct the leading edge by having a smooth spline with continuous and smooth curvature; The new and correct offsets of the Clark Y foil contain 142 points along the foil section which are detailed in 2 tables (table 2 and table 3) describing the upper and the lower surfaces of the foil, respectively.

Using the corrected geometry with an analytical solution well detailed and explained, the results of the CFD model were compared to experimental and analytical solutions of a single foil. The obtained precision of the results is very high and was achieved for all the cases that were examined. Furthermore, The CFD solution is much closer to the experimental results than to the analytical solution which shows how accurate and close the CFD is to the real life. One of the boundary conditions was examined for its impact of the results. Surprisingly, it was discovered that the FREE slip condition along the foil is much closer to the physical process under the following assumptions that have to be preserved:

1. Small angles of attack where separation does not take place.
2. The viscosity of the fluid is very small and can be neglected. The boundary layer effects are second in importance and do not change the results.
3. The flow is in the turbulent regime so if separation occurs, reattachment of the flow takes place. In contrary to laminar regime where no reattachment of the flow can happen after it detaches.
4. The body is a streamlined body where the flow re-joins once it separates at the leading edge.
5. The flow does not have to be incompressible. However, being such, the analytical and CFD solution are easier to solve. Fortunately, sea-water is an incompressible fluid domain.

Before approaching the main core of this research, a study was done of exploring the flow field around a stretched body in its horizontal coordinates. The obtained results were exactly as expected where the pressure at the leading edge got bigger and the lift coefficient went down as the stretched factor was enlarged. The pressure went up due to a sharper corner at the leading edge and the total lift went down due to a bigger chord length while keeping the same camber.

The core investigation of this research is the bi-plane case where two identical foils vertically oriented are under few angles of attack. Seven different cases were examined where 4 of them have experimental results for comparison. The obtained precision of the results, compared also with a single foil, is very high and satisfactory. A surprising phenomenon was discovered when the gap between the foils was 25%. Unfortunately, no experiments were done for such a case because of the difficulty of performing it, so the results were verified by the CFD process itself using the bands tool, as detailed in chapter 4 for a single foil. The main conclusion of the bi-plane case is that a single foil does better when it comes to performance, and the reason for using bi-planes in the past was structural rather than stability or speed.

Another interesting case that was examined, following the bi-plane case, is the stagger case where two identical foils horizontally oriented are under few angles of attack. Five different cases were examined but no experimental results were available. According to the CFD results, the first foil gives better lift when the gap between the foils is 100% but as a cellule, the single foil is better. The bottom line for the stagger case, as for the bi-plane case, is that a single foil does better when it comes to performance.

While performing this research, the outstanding advantages of the CFD process appeared over and over in every analysis. Every time one of the parameters was changed, whether it is the velocity of the fluid or the viscosity, the geometry of the foil, adding another foil to the model, re-displacing it with relation to the other foil - the effortlessness of doing it compared with performing an experiment is impressive. Plotting the streamlines, the velocity or pressure fields and the vorticity around the foils are some of the many accessible features of the CFD software. However, it is very important to pay attention to the way the process is done and the user should be very careful with inputting the known data of the problem - as explained in chapter 3.

In summary, this research is very wide but also deep as well in its knowledge, references and academic work. The objective has been achieved by using many tools where the ADINA software plays the main role. This paper may be used for future research based on it or continuation of it such as: a 3D CFD model of a foil, foil with different grooves along its chord length, the groove effects in the laminar and turbulent regimes and different end-geometries of the foil to improve its performance and characteristics.

References[2]

[1] Owen Hughes, *Ship Structural Design*, The Society of Naval Architects & Marine Engineers, NJ, 1988.

[2] Edward V. Lewis, *Principles of Naval Architecture, vol. II - Resistance, Propulsion and Vibration*, Chapter 5, The society of Naval Architects and Marine Engineers, NJ, 1988.

[3] Thomas C. Gillmer and Bruce Johnson, *Introduction to Naval Architecture*, Naval Institute Press, Annapolis, Maryland, 1982.

[4] J.N. Newman, *Marine Hydrodynamics*, MIT, 1978.

[5] Massachusetts Institute of Technology, *2.20 Marine Hydrodynamics - Lecture notes*, Fall 2007.

[6] Theodore Theodorsen. *Theory of wing sections of arbitrary shape*. NACA Report No.411, 1932.

[7] Ira H. Abbott and Albert E. Von Doenhoff, *Theory of wing section*, Dover Publications, NY, 1958.

[8] Pinkerton, Robert M. *Calculated and Measured Pressure Distributions over the Midspan Section of the NACA 4412 Airfoil*. NACA Report No.563, 1936.

[9] Prof. Bathe KJ., *Finite Element Procedures*, Prentice Hall, NJ, 1996.

[10] Kohno H, Prof. Bathe KJ. *Insight into the flow-condition-based interpolation finite element approach: solution of steady-state advection-diffusion problems*. International Journal for Numerical Methods in Engineering 2005; **63:**197-217.

[11] Kohno H, Prof. Bathe KJ. *A nine-node quadrilateral FCBI element for incompressible fluid flows.* Communications in Numerical Methods in Engineering 2006; **22:**917-931.

[12] Banijamali B, Prof. Bathe KJ. *The CIP method embedded in finite element discretizations of incompressible fluid flows*. International Journal for Numerical Methods in Engineering 2007; **71:**66-80.

[13] Riegels, F.W., *Airfoil Sections*, Butterworths, London, 1961 (English translation from German).

[14] Airfoil Design Workshop, Copyright 2003-2006, www.tdmsoftware.com.

[15] Unigraphics NX 2.0.0.21, Copyright 2003 Electronic Data Systems Corporation (EDS).

[16] ADINA System version 8.4, AUI (ADINA User Interface) Primer, Problems and solutions.

[17] Sylvia and Milton Van Dyke, *An Album of Fluid Motion - 11th printing*, California, May 2007.

[18] Max M. Munk, *General Biplane Theory*, Report National Advisory Committee for Aeronautics, Report No. 151, 1923.

[19] William Frederick Durand, *Aerodynamic Theory*, Volume II out of VI, Dover Publications, NY, 1935.

[20] Montgomery Knight and Richard W. Noyes, *Wind Tunnel Pressure Distribution Tests on a Series of Biplane Wing Models*, Report National Advisory Committee for Aeronautics, Report No. 310, 1929.

[2] This list is sorted by the order of the references given in this document.